

Characteristics of Precipitation and Extreme Precipitation Events over the Drakensberg Mountains in Past and Future Climates



by

Ridick Roland TAKONG
(RDCTAK001)

Thesis Presented for the Degree of

Doctor of Philosophy

In the Department of Environmental and Geographical Science

University of Cape Town

Supervised by: Assoc. Prof. Babatunde Joseph ABIODUN

January 18, 2023

The copyright of this thesis vests in the author. No quotation from it or information derived from it is to be published without full acknowledgement of the source. The thesis is to be used for private study or non-commercial research purposes only.

Published by the University of Cape Town (UCT) in terms of the non-exclusive license granted to UCT by the author.

Declaration 1

I hereby declare that all the work in this thesis is mine and that information derived from other studies has been properly acknowledged and referenced in an included reference list. I understand the meaning of plagiarism and know that it is wrong.

Ridick Roland TAKONG, January 18, 2023

Declaration 2

Parts of materials of this thesis have been submitted for publication in the following papers:

- Takong RR and Abiodun BJ (2023): Improving the model simulation of rainfall over the Drakensberg on weak-synoptic days. *Modelling Earth Systems and Environment* (DOI:10.1007/s40808-022-01686-y).
- Takong RR and Abiodun BJ (2023): Simulating widespread extreme rainfall events over the Drakensberg with WRF and MPAS models. *Climate Dynamics* (under review).
- Takong RR and Abiodun BJ (2023): Projected changes in precipitation characteristics over the Drakensberg Mountain Range. *International Journal of Climatology* (DOI:10.1002/joc.7989).

The co-author of the manuscripts directed and supervised the research that forms the basis for the thesis.

Abstract

The Drakensberg Mountains is one of the most valuable natural resources in Southern Africa because precipitation over the mountains is the source of rivers that support socio-economic activities in Lesotho, South Africa, and Namibia. Meanwhile, extreme precipitation events over the Drakensberg are a threat to the communities around the mountains. While several studies have shown that mountains are among the most sensitive regions to climate variability and change, the potential impacts of global warming on precipitation and extreme precipitation occurrences over the Drakensberg are poorly understood. This thesis examines the characteristics of precipitation and extreme precipitation events over the Drakensberg in past climate and investigates how the characteristics might change in future climate at various global warming levels under RCP8.5 future climate scenario. Series of climate datasets were analyzed for the study. These include observed precipitation datasets from eight satellite products, reanalysis datasets from National Centre for Environmental Prediction (NCEP) Climate Forecast System Reanalysis (CFSR), and climate simulation datasets from the Model for Prediction Across Scales (MPAS), Weather Research and Forecasting Model (WRF), and the National Aeronautics and Space Administration (NASA) Earth Exchange Global Daily Downscaled Projections (NEX), and the Coordinated Regional Climate Downscaling Experiment (CORDEX). All the simulation datasets were evaluated against the observation datasets. Precipitation indices were used to characterize precipitation and extreme precipitation events over the Drakensberg Mountains, with emphasis on widespread extreme events (WEREs). Self Organizing Map (SOM) technique was employed to group the synoptic patterns over southern Africa, WERE patterns over DMR, and the future climate change projections over the Drakensberg Mountains.

Results of this dissertation reveal that the weak synoptic days, which are associated with high-pressure systems or the ridging of highs, account for 16 – 20% of weather conditions in March-August and 5% of annual rainfall over the Drakensberg. Wet weak synoptic days can induce widespread extreme rainfall (up to 20mm day^{-1}) over the Drakensberg. CFSR underestimates the magnitude of the weak-synoptic-day rainfall but the WRF downscaling of the CFSR dataset enhances the quality of the simulated rainfall. All of the climate simulation datasets (WRF, MPAS, CORDEX, NEX) give realistic simulations of the precipitation indices over Southern Africa, especially over South Africa and DMR. In most cases, the biases in the simulations are within the observation uncertainties. SOM analysis reveals four major patterns of WERE patterns over the Drakensberg. The most prevalent WERE pattern usually occurs on the eastern side of the mountain, stretching from north-east to the south-west along the coastline, and it is usually induced by tropical temperate troughs, cold fronts, and the ridging highs.

There is no agreement among simulations ensemble means on the annual precipitation projection over DMR. However, the ensemble means agreed on an increase in the intensity of normal precipitation and a decrease in the number of precipitation days and the number of continuous wet days. They also agreed on a future increase in frequency and intensity of extreme precipitation and widespread extreme events over DMR. SOM analysis, which elucidates the range of projection patterns that lie beneath the simulation ensemble means of the simulations, shows the most probable combination of projected changes in the annual precipitation and extreme precipitation events (intensity and frequency) over DMR: (i) an increase in both annual precipitation and extreme precipitation events; (ii) a decrease in

both annual precipitation and extreme precipitation events; (iii) a decrease in annual precipitation but increase in extreme precipitation events. Results of this study can provide a basis for developing climate change adaptation and mitigating strategies over the Drakensberg.

Keywords: Mountains, WRF model, Weak Synoptic Conditions, Drakensberg, Self-Organizing Maps, Extreme precipitation, Climate change, MPAS Model.

Acknowledgements

I thank GOD Almighty for bringing me thus far and His son Jesus Christ who saved me from sin. Particularly, I thank him for endowing me with wisdom, knowledge, favour, strength, determination and good health through out my study here at UCT.

Secondly, I thank Associate Professor Babatunde Joseph Abiodun for accepting to supervise me and for his guidance throughout the Ph.D. period.

This work was supported by the University of Cape Town's (UCT) Faculty of Science Ph.D. Fellowship, the International Students and Refugees Scholarship of the Postgraduate Funding Office, and the Water Research Commission (WRC) of South Africa. The computational resources were provided by the Centre for High Performance Computing (CHPC) in South Africa and the Climate Systems Analysis Group (CSAG) at UCT.

I am very grateful to my parents Mr. Takong Nkatow Abraham and Mrs. Vosinwi Grace Takong for all the efforts and sacrifices they have made to raise me to be who I am today. Their continuous encouragement helped me push this work to completion. Thank you for being the giants on whose shoulders, I stood all these years. I thank my brothers, sisters, cousins, uncles, and aunts for their encouragement.

I thank my wife Dr. Aude Ines TAKONG for her encouragement and support throughout the Ph.D. period.

Finally, I thank God for my sons (Uriel J. Takong and Jayden A. Takong) and daughter (Ange Ruth Takong) who were born during the Ph.D. journey. They motivated me to study to the end.

Dedication

To my parents (TAKONG NKATOW Abraham & Vosinwi Grace TAKONG), wife (Aude Ines TAKONG) and children (Uriel J. TAKONG, Jayden M. TAKONG & Ange Ruth TAKONG).

Contents

Declaration 1	i
Declaration 2	ii
Abstract	iii
Dedication	vi
Table of Contents	ix
List of Figures	xi
List of Tables	xii
List of Abbreviations	xii
1 Introduction	1
1.1 Background	1
1.2 Impacts of rainfall variability over the Drakensberg	2
1.3 Factors controlling characteristics of precipitation over mountains	3
1.3.1 Diurnal cycle of mountain heating.	3
1.3.2 Dynamic modification of airflow by a mountain as an obstacle or barrier.	3
1.3.3 Thermodynamics of airflow over mountains.	6
1.3.4 Modification of synoptic systems over mountains.	6
1.3.5 Location of the mountain.	6
1.3.6 Mountain–mass effect.	7
1.4 Atmospheric models	8
1.4.1 Statistical Downscaling.	8
1.4.2 Regional climate modelling.	9
1.4.3 Variable-resolution GCMs.	10
1.5 Motivation for the study	10
1.6 Aims and objectives	11
1.7 Thesis outline	11
2 Literature review	13
2.1 Characteristics of precipitation over the Drakensberg	13
2.2 Factors controlling precipitation over the Southern Africa	14
2.2.1 Inter-annual to decadal precipitation variability.	15
2.2.2 Seasonal and intraseasonal rainfall variability.	16
2.2.3 Botswana High.	17
2.3 Southern African weather producing systems and precipitation over the Drakensberg	18
2.3.1 The Ridging High.	18

2.3.2	The Angola low.	19
2.3.3	Cold Front.	19
2.3.4	Cut-off lows.	19
2.4	Challenges in simulating precipitation over the Drakensberg	20
2.4.1	Paucity of Observational data.	20
2.4.2	Low model resolution.	21
2.5	Climate change projection over Southern Africa	22
2.6	Scaling of extreme precipitation versus temperature changes	24
3	Methodology	26
3.1	Study area	26
3.2	Dataset	27
3.2.1	Observation datasets.	27
3.2.2	Reanalysis data.	28
3.2.3	Model simulation data.	29
	CORDEX dataset	30
	NEX dataset	31
	WRF model	32
	The MPAS	32
3.3	Methods	33
3.3.1	Identification of weak synoptic days and wet weak synoptic days..	33
3.3.2	Definitions of rainfall and extreme rainfall indices.	34
3.4	Quantifying phase synchronization between observed and simulated variables	34
3.5	Classification of rainfall patterns on WERE days.	35
3.5.1	Classifying or grouping the spatial patterns of climate variables.	36
4	Simulating rainfall distribution over the Drakensberg on weak synoptic days	38
4.1	Characteristics of weak synoptic days	39
4.2	Rainfall over Drakensberg on wet weak synoptic days	40
4.3	Major patterns of WSD precipitation and the associated dynamics	43
4.4	WRF simulation over the Drakensberg	46
4.5	Summary	54
5	Simulating widespread extreme rainfall events over the Drakensberg using WRF and MPAS models	56
5.1	Rainfall and extreme rainfall indices	58
5.2	Synoptic atmospheric features and WERE over the DMR	62
5.3	Spatial patterns of WERE over the Drakensberg	66
5.4	Thermodynamic and dynamic conditions associated with the EWR pattern.	68
5.5	Summary	69
6	Projected changes in precipitation characteristics over the Drakensberg Mountains	70
6.1	Evaluation of CORDEX and NEX datasets	72
6.2	Future Projections over the Drakensberg Mountains	77
6.2.1	Projected changes in mean rainfall intensity.	77
6.2.2	Projected changes in duration indices.	79
6.2.3	Projected changes in extreme rainfall indices.	79
6.2.4	Scaling of extreme precipitation changes.	81

6.3	The SOM classification of the future projections	82
6.4	Summary	89
7	Conclusions and Recommendations	91
7.1	Conclusions	91
7.2	Recommendations	93
	References	110

List of Figures

1.1	Location of the Drakensberg Mountain Range	1
1.2	The influence of diurnal mountain heating on convective precipitation in a mountain region during the day and night.	3
1.3	Mountain inducing precipitation by acting as an obstacle to an airflow.	4
1.4	Mountain inducing precipitation by acting as a (a) total or (b) partial barrier to statistically stable and slowly moving airflow.	4
1.5	Mountain inducing precipitation by acting as an obstacle to a stable airflow with pre-existing clouds in (a) single vertical layer and (b) two vertical layers	5
1.6	Mountain waves inducing clouds and precipitation around mountains.	5
2.1	Austral summer season synoptic features.	18
3.1	Topography of Southern Africa and the Drakensberg	26
3.2	Location of weather observation stations used for the validation of satellite rainfall datasets	30
3.3	Taylor diagrams used for the comparison of satellite rainfall datasets with South African Weather Service (SAW) station observation over the Drakensberg	31
4.1	WRF model nested domain setup	38
4.2	Composite of mean sea level pressure during different geostrophic wind (GW) conditions over the Drakensberg during different seasons in period 1983 – 2012	40
4.3	Percentage frequency distribution of geostrophic wind speed and the percentage rainfall contribution of each GW range to the total rainfall over the Drakensberg.	41
4.4	Characteristics of Weak Synoptic Conditions over the Drakensberg.	42
4.5	SOM classification of WEREs over the DMR and seasonal frequency of the WERE patterns	44
4.6	Composites of synoptic atmospheric conditions associated with wet WSD rainfall patterns.	45
4.7	Comparison of WRF model topography at different horizontal resolutions.	47
4.8	Composite of Node 1 as observed by CHIRPS and ARC2, and depicted by CFSR, and simulated by the WRF model	48
4.9	Composite of Node 3 as observed by CHIRPS and ARC2, and depicted by CFSR, and simulated by the WRF model	49
4.10	Composite of Node 9 as observed by CHIRPS and ARC2, and depicted by CFSR, and simulated by the WRF model	50
4.11	Comparison of observed (CHIRPS and ARC2), reanalysis (CFSR), and simulated (WRF) rainfall over the Drakensberg for Nodes 1, 2 and 9.	51
4.12	Local processes prevalent and influencing rainfall distribution during wet WSD.	52
4.13	Vertical cross section of the diurnal variation of potential temperature, vertical velocity and associated diurnal cycle of rainfall.	53
4.14	Local processes prevalent and influencing rainfall distribution during wet WSD.	54
5.1	Simulation domain for WRF and MPAS models	57
5.2	Variation in number of WEREs with WERE threshold criteria over DMR	58

5.3	Spatial distribution of rainfall indices over Southern Africa as depicted by observation, reanalysis and simulations.	59
5.4	Rainfall intensity–frequency curves over the Drakensberg as depicted by observation, reanalysis and simulation datasets.	60
5.5	Annual variation of WERE frequency anomalies over the DMR in the period 1987 – 2016	61
5.6	SOM analysis of daily mean sea-level pressure (MSLP) over Southern Africa (1987–2016).	62
5.7	Seasonal frequency of synoptic patterns identified with SOM.	63
5.8	Frequency of WERE occurrence during the synoptic patterns identified with SOMs. . . .	65
5.9	SOM classification of WEREs over the DMR and seasonal frequency of the WERE patterns	67
5.10	Thermodynamic and dynamic conditions associated with occurrence of EWR patterns over the Drakensberg in summer.	68
6.1	Precipitation intensity–frequency over the DMR	73
6.2	Comparison of biases in the CORDEX and NEX simulation datasets using a boxplot. . .	74
6.3	Spatial distribution of the precipitation indices over the Drakensberg	76
6.4	Projected changes in extreme precipitation indices over the Drakensberg	77
6.5	CORDEX and NEX projected changes in rainfall indices over Drakensberg at four GWLs	78
6.6	Scaling between future changes in extreme rainfall–temperature and the temperature over DMR at various global warming levels as depicted by CORDEX and NEX datasets.	82
6.7	SOMs classification of projected changes in annual rainfall	84
6.8	SOMs classification of projected changes in R97.5p	85
6.9	SOMs classification of projected changes in REXTRFREQ.	86

List of Tables

3.1	Atmospheric variables that were analysed from each dataset used in the thesis.	28
3.2	Information about observation datasets used in the study. The period of the data analysed in each dataset is indicated	29
3.3	Definition of extreme rainfall indices used in this study.	35
4.1	WRF model configuration for simulation of rainfall patterns from SOM classification. . .	39
5.1	MPAS and WRF model physics parameterization setup	56
5.2	Description of the nine dominant synoptic weather patterns identified in Figure 5.6 and the percentage contribution of each dataset	64
6.1	List of GCMs simulations downscaled by NEX and CORDEX	71
6.2	Simulated mean and standard deviation of rainfall indices over DMR during the present-day and the projected changes under various global warming	80
6.3	Ranking of GCM simulations for downscaling over DMR based on their contribution to the SOMs classification of projected changes in RTOT and R97.5p patterns.	87
6.4	Projected changes in precipitation over the Drakensberg and its potential impacts and suggested adaptation strategies	88

List of Abbreviations

ARC2	African Rainfall Climatology version 2
BCSD	Bias-Correction Spatial Disaggregation
CC	Clausius-Clapeyron
CFSR	Climate Forecast System Reanalysis
CHIRPS	Climate Hazard Group Infrared Precipitation with Stations
CMIP5	Fifth phase of the Coupled Model Intercomparison Project
COL	Cut-Off Lows
CORDEX	Coordinated Regional Climate Downscaling Experiment
CPC	Climate Prediction Centre
CRU	Climate Research Unit
FEWS	Famine Early Warning System
GCM	General Circulation Model
GPCC	Global Precipitation Climatology Centre
GW	Geostrophic wind
GWL	Global Warming Level
HPOD	Heavy Precipitation Over the Domain
ITCZ	Intertropical Convergence Zone
MPAS	Model for Prediction Across Scales
MPNE	Moderate Precipitation over the North-East
MPSW	Moderate Precipitation Over the South-West
NASA	National Aeronautics and Space Administration
NCEP	National Centre for Environmental Prediction
NEX	Earth Exchange Global Daily Downscaled Projections
NEX-GDDP	Earth Exchange Global Daily Downscaled Projections
PERSIANN	Precipitation Estimation from Remotely Sensed Information using Artificial Neural Network
QBO	Quasi-Biennial Oscillation
RCPs	Representative Concentration Pathways

RH Relative Humidity
SOM Self-Organizing Map
SOMs Self-Organising Maps
SPEI Standardised Precipitation Evapotranspiration Index
SPI Standardized Precipitation Index
TTT Tropical Temperate Troughs
TUVA Tugela–Vaal water transfer scheme
UNESCO United Nations Educational, Scientific and Cultural Organization
VGCMs Variable Resolution Global climate models
WCRP World Climate Research Program
WFDEI Water and Global Change Forcing Data methodology applied to ERA-Interim
WPOD Weak Precipitation Over the Domain
WRF Weather Research and Forecasting
WSC Weak Synoptic Conditions
WSDs Weak Synoptic Days

CHAPTER 1

Introduction

1.1 Background

The Drakensberg Mountains (hereafter, the Drakensberg; $28^{\circ}S - 32^{\circ}S$ and $26^{\circ}E - 32^{\circ}E$), located in the eastern escarpment of South Africa (Figure 1.1), is the highest mountain range in Southern Africa and one of the most valuable natural resources in Africa (Nel and Sumner, 2006). This trans-frontier mountain straddles the border between South Africa and Lesotho, with the highest peak exceeding $3000m$ above mean sea level (Nel, 2009). Its natural beauty makes it a major tourist attraction in Southern Africa. The Drakensberg features pristine steep-sided river valleys, rocky gorges, numerous caves, and rock shelters (which contain about 665 rock art sites). It provides a natural habitat for lots of plants and animal species. For example, it accommodates endemic and threatened species like the Yellow-breasted Pipit. Due to this rich natural diversity, the Drakensberg was designated as a UNESCO World Heritage site in the year 2000 (UNESCO, 2000).

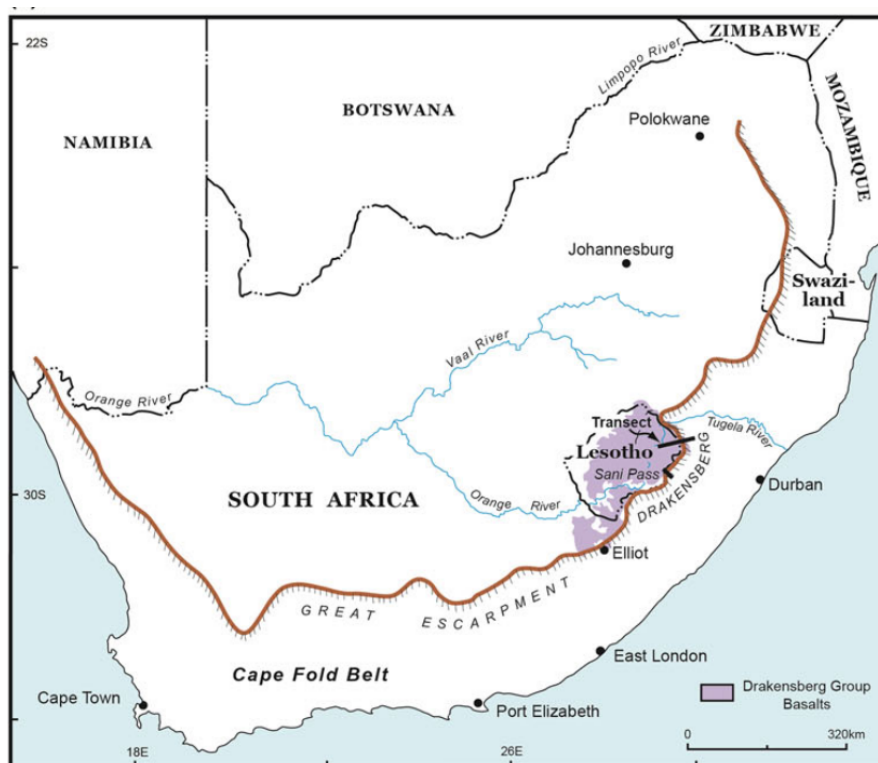


Figure 1.1: Location of the Drakensberg Mountain Range in Southern Africa (source: Knight and Grab, 2015).

Furthermore, the rainfall over the Drakensberg is the source of water for many rivers that support socio-economic activities (like agriculture, mining, and hydro-electric power generation) in Southern African countries. For example, the Vaal River, which takes its rise from the upper catchments of the Drakensberg, is the largest tributary of the Orange River, a key water source for industrial activities in South Africa and Namibia. The Drakensberg also supports two large inter-basin water transfer schemes: the Tugela–Vaal water transfer scheme (TUGVA) and the Lesotho Highlands Water Project. However, the large variability in the Drakensberg rainfall remains a challenge to the socio-economic activities in the surrounding communities.

1.2 Impacts of rainfall variability over the Drakensberg

Rainfall variability over mountains can manifest as droughts or heavy rainfall events with huge socio-economic impacts on the surrounding communities that depend on the mountains for various socio-economic activities. The rainfall variability over the Drakensberg is a threat to the environment, agriculture, and water resource management in Southern African countries. As a major water tower for Southern African countries (e.g., Lesotho, South Africa and Namibia), rainfall over the Drakensberg influences stream flows in these countries (Everson, 2001; Nel and Sumner, 2006). For instance, a substantial decrease in the annual rainfall can lead to hydrological droughts in these countries. A dry year over the Drakensberg means a continuous low flow discharge in these countries throughout the year, making the water resources and transfer schemes operation around the Drakensberg (e.g., TUGVA) more difficult to manage. On the other hand, heavy rainfall events over the Drakensberg can induce floods, landslides, soil erosion, destruction of property, and loss of lives in the communities around the Drakensberg (Hyden et al., 2000). For example, in September 1987, an extreme rainfall event caused more than 300 fatalities and damaged more than a billion Rands (about 85 million US Dollars) infrastructure in KwaZulu-Natal Province, South Africa (Tennant and van Heerden, 1994). And similar events occurred in April 2019 and 2022 (Pinto et al., 2022).

Rainfall variability can also influence tourism in mountain regions (Haeberli and Beniston, 1998). Specifically, uncertain snow cover during peak winter sports seasons may discourage tourists from coming to the mountains. This may lead winter sports resorts into financial difficulties even during favourable winters. The Vaal Dam near Vereeniging is a popular water sports playground offering canoeing, paddle-boating, power-boating, jet skiing, and fishing, among other water sports. These water sports activities may be affected by a change in the Vaal river flow resulting from rainfall variability over the Drakensberg.

However, there is concern that the global warming may enhance rainfall variability over the Drakensberg (Kruger, 2006; Mason et al., 1999; Karl and Trenberth, 2003; Fatti and Patel, 2013; Pohl et al., 2017; Abiodun et al., 2017). This could alter the extreme rainfall intensity and frequency over the Drakensberg. Global warming could also lead to a seasonal or spatial shift in the Drakensberg climatic regimes (in particular precipitation), altering the characteristics of river systems that originate in the mountain area. This could lead to regional water stress with devastating impacts on water resources, agricultural and economic productivity, ecological systems, and human health (Maúre et al., 2018). Therefore, to enhance the quality of life and socio-economic activities of people living in the vicinity of the Drakensberg and those living downstream of the rivers that originate from the mountain range, there is a need to better our knowledge and prediction of precipitation characteristics over the Drakensberg, including the processes that control the precipitation.

1.3 Factors controlling characteristics of precipitation over mountains

The characteristics of precipitation (especially the spatio-temporal distribution) over mountain regions depend on the two-way interactions between synoptic-scale and local-scale atmospheric processes in the mountain. This section describes some of the mechanisms through which the interactions take place.

1.3.1 Diurnal cycle of mountain heating.

The non-homogeneous diurnal solar radiation heating of a mountain region might create convection in the mountain surroundings (Figure 1.2). During the day, the solar heating of the mountain's slope and the peak is greater than that of the surrounding air. This may lead air parcels to climb above the level of free convection and converge at the peak of the mountain. It could also improve the parcels' potential buoyancy. These effects typically cause the greatest amount of convective precipitation to fall over the mountain during the warmest period of the day (Figure 1.2a). At night, the opposite is true. The evening cooling over the mountaintops slows convection. Nonetheless, if the night-time cooling-induced down slope motion collides with a moist unstable low-level flow, a night-time precipitating convection may form at the mountain's base (Figure 1.2b).



Figure 1.2: The influence of diurnal mountain heating on convective precipitation in a mountain region during the day and night. Modified after Houze Jr (2012).

1.3.2 Dynamic modification of airflow by a mountain as an obstacle or barrier.

The response of a moist airflow meeting obstacle topography (mountain) depends on whether the flow is thermodynamically stable or unstable (Figure 1.3). If the incoming airflow is unstable, the mountain may elevate air over its level of free convection, causing convective clouds and precipitation (Figure 1.3a). If the approaching airflow is stable, it often follows the topography upward, and the motion's vertical component creates or strengthens a cloud on the windward side (Figure 1.3b). On the leeward side, the cloud dissipates.

However, the response of the stable flow to the terrain is also affected by the degree of thermodynamic stability of the oncoming flow, the height of the terrain barrier, and the strength of the upstream airflow's cross-barrier component. These variables are sometimes combined to form a non-dimensional number known as the Froude Number (which is the ratio $\frac{U}{Nh}$, where U is the cross-barrier flow strength, N is the Brunt-Väisälä frequency, and h is the maximum terrain height). The Froude number quantifies the importance of non-linear effects in flow. When the Froude number is high, the airflow rises readily over the terrain; when it is low, the incoming airflow is impeded or blocked, and the air does not climb easily. When approaching the terrain, the flow may turn to flow parallel to a barrier or around an isolated hill or



Figure 1.3: Mountain inducing precipitation by acting as an obstacle to airflow in (a) an unstable and (b) a stable condition. Modified after Houze Jr (2012).

mountain. A good relationship between Froude number and orographic precipitation has been reported over various mountain regions around the world, including the Alpines (Steiner et al., 2003) and the Hawaiian mountains (Carbone et al., 1998).

If the air moving toward a barrier of land is stable (has a low Froude number) and is moving slowly, it doesn't easily rise over the land. Instead of rising over the terrain, the air tends to accumulate behind the barrier, like water behind a dam. As a result, the air above the barrier layer can be elevated substantially above the mountain barrier. This type of blocking can have an impact on both convective storms and frontal systems (Figure 1.4a). In places where there is only partial blocking, the return to equilibrium in the form of a hydraulic jump may cause a cloud and rain to form at lee side of the mountain (Figure 1.4b).



Figure 1.4: Mountain inducing precipitation by acting as a (a) total or (b) partial barrier to statistically stable and slowly moving airflow. Modified after Houze Jr (2012)

If the airflow over a mountain consists of a pre-existing cloud and the mountain barrier is tiny (e.g., a hill), the pre-existing cloud may be amplified to produce maximum precipitation on the upwind side of the barrier. Since the hill is low, the precipitating cloud would be advected over it and to the lee side, where the down slope air motion would weaken its precipitating capacity (Figure 1.5a). This process can also occur in layers that are separated vertically (Figure 1.5b). Thus, the pre-existing precipitating cloud can be advected over the hill at a higher level, while a shallow orographic cloud forms right over the hill in the low-level up slope flow. By accretion of cloud water in the lower cloud, the precipitation particles from the higher cloud would expand, increasing precipitation on the leeward side of the mountain.

A stable airflow passing over a mountain can generate mountain waves, which usually enhance or



Figure 1.5: Mountain inducing precipitation by acting as an obstacle to a stable airflow with pre-existing clouds in (a) single vertical layer and (b) two vertical layers. Modified after Houze Jr (2012)

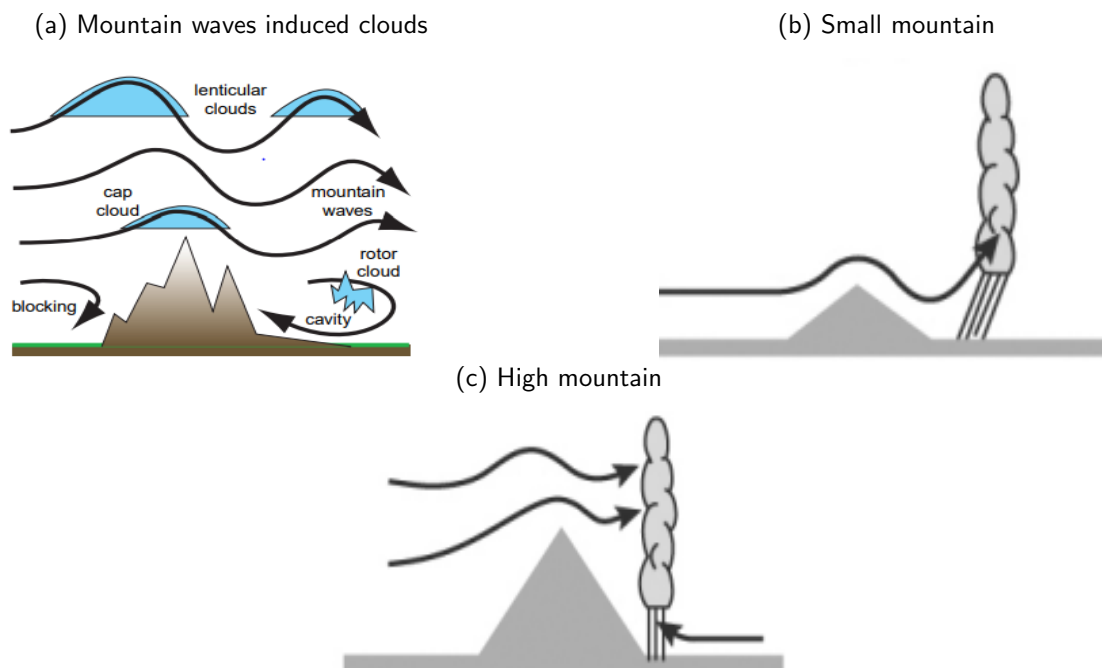


Figure 1.6: Mountain waves inducing clouds and precipitation around mountains. Modified after Wallace and Hobbs (2006) and Houze Jr (2012).

suppress cloud and precipitation amounts around mountain ranges. This occurs when the air flowing across a mountain barrier is displaced vertically. The vertical displacement is counteracted by the force of gravity which tries to restore the displaced air to its equilibrium position on the lee of the mountain. Very often, as the air flows downwind, vertical oscillations develop leading to the formation of clouds and precipitation around the mountains (Figure 1.6). The occurrence of distinctive cloud forms (e.g., cap cloud, lenticular cloud and rotor clouds) around mountains is visible evidence of mountain waves (Figure 1.6a). Mountain waves have been reported to contribute to unexpectedly heavy snow across the Smoky Mountains in the US (Gaffin et al., 2003). However the size of a mountain influences the location of precipitation induced by the mountain waves. For instance, near a small mountain, the upward motion of a lee wave might cause persistent precipitating convective clouds to be advected downwind and generate leeward side rain bands parallel to the flow (Figure 1.6b). Vertically propagating wave motion launched over high mountains may cause precipitating convective cloud systems wave on

the lee side of a high peak (Figure 1.6c).

1.3.3 Thermodynamics of airflow over mountains.

The thermodynamics of air ascending over mountains can influence cloud precipitation over mountains (Barry, 1992; Houze Jr, 2012). Specifically, the saturation vapour pressure of the atmosphere drops exponentially with temperature and, thus, altitude. On the windward side of a barrier, precipitation created by upward air motion and microphysical development processes is most robust at lower levels. Consequently, the precipitation is likely to be heavier on the lower slopes of a mountain with a high elevation. In addition to the microphysical time scale and terrain size, precipitation fallout over mountains is governed by the micro physical time scale and terrain size. Water drops and ice crystals need time to grow to a precipitable size before they can fall, and the height and steepness of the terrain limit where the falling particles can settle. Therefore, the relationship between the micro physical time scales of particle growth and the spatial scales of the terrain is significant and essential.

1.3.4 Modification of synoptic systems over mountains.

A mountain can modify the frontal characteristics of a synoptic system (e.g. front) that is passing over the mountain (Houze Jr, 2012; McCauley and Sturman, 1999; Barry, 1992). For example, when a front encounters a mountain barrier, frontolysis (frontogenesis) occurs on the windward (leeward) slopes of the mountain in the westerlies. This may be caused by the alteration of the temperature profile of the front. The alteration of the temperature profile may result from adiabatic cooling (warming) during forced ascent (descent) of air ahead of the front. Mountains can retard and block an approaching cold front. The slowing down and deformation of fronts as they traverse a mountain barrier can also cause a change in vertical motion fields, thereby influencing precipitation and cloud patterns. Weather conditions on the lee slopes of mountain barriers are affected by cyclones that form on the leeward side of the mountain. Cyclones may develop if a meridional flow of cold air is obstructed by a mountain and there is an intensification of baroclinic conditions in the lower troposphere.

1.3.5 Location of the mountain.

The latitudinal location of a mountain can affect the local climate and weather around the mountain due to several reasons. Firstly, the temperature of any location depends on the amount of insolation at the location and insolation varies with latitude. For example, the net insolation at lower latitudes (around the equator) is higher than that at high latitudes (poles). Hence, higher temperatures may be expected in equatorial than polar mountains. Secondly, latitudinal location also determines seasonal and diurnal climate cycles (or patterns). For example, seasonal variation of temperature, insolation and day length is smaller in the lower latitudes compared to the higher latitudes, whereas the diurnal amplitude of temperature, for example, is relatively large. These latitudinal differences in temperature regime also affect the precipitation characteristics. For example, in low latitude high mountains, snow can only occur on any day of the year at altitudes above 4000m (Barry, 1992) but, in the middle and higher latitudes mountains, where there is a well-marked and prolonged winter season, snow can occur at much lower altitudes. Like in the Alps (mid-latitude mountain), there is snow cover at altitudes above 3000m for about 350 days per year.

The proximity of mountains to water bodies also influences precipitation over the mountains. Precipitation on coastal mountains may be enhanced by the interaction of the sea breeze effect and mountain winds as well as moisture resulting from evaporation over the water body. A sea breeze is a cool day-

time wind that blows from the ocean to land (similar flows form over lake shorelines and are called lake breeze). The sea breeze circulation is formed due to the difference in temperature between continental landmass and the surrounding water body. This difference in temperature stems from the difference in heat capacity of land and water. Water has a high specific heat capacity compared to dry soil. This causes the water to heat up more slowly than the land. Consequently, the air immediately above the water surface is cooler than the air over the land surface at the same height. This results in higher air pressure at the water surface and lower air pressure on the land surface (at low altitudes). The pressure difference causes cool air at the water surface to flow towards the land surface forming the sea breeze. Aloft, the situation is different. Specifically, high pressure aloft over land and low pressure aloft over ocean results in a return flow from land to ocean aloft. A sea-breeze front is the leading edge of cool maritime air moving in from the ocean. It acts like a thunderstorm gust front or a weakly moving cold front. If the rising air along the front is sufficiently humid, a band of cumulus clouds may develop on the frontal boundary. If the atmosphere is convectively unstable, this line of cumulus clouds can then turn into a line of thunderstorms. Upslope winds on coastal mountain slopes are caused by the strong heating of the mountain slopes. The sea breeze may make these winds stronger. The mountain slope may cause force uplift of sea breeze or local valley winds. For example, [Tyson et al. \(1976\)](#) found that in summer over the Drakensberg, conditions that favour thunderstorm activity occur when moisture-laden air is advected over the "Natal" by plain-mountain winds near the surface and northerly gradient winds above. The sea breeze can also transport moisture-laden from the surrounding water body to the mountains where force uplift by the mountain slope causes the moist air to rise, condense and fall back as precipitation.

The orientation, size and shape of a coastal mountain can also influence the formation of sea breeze and precipitation over and around the mountain. For example, if the slope of a coastal mountain is facing the sea and is located inland of a coastal plain, its influence on the sea breeze system will be controlled by the slopes surface temperature cycle ([Miller et al., 2003](#)). If the temperature of the mountain slopes vary with the same diurnal period as that of the coastal plain, then the sea breeze system is enhanced and occurs earlier than it would normally occur if the mountain was not present. If the mountain slopes act as a barrier only, the sea breeze would be confined to the coastal plain. On the other hand, if the mountain's topography is complex, it may produce several separate sea breeze systems along different portions of the coast line. The appearance of these different independent sea breeze systems may not occur at the same time and their intensities may be different. The topographic variation (inland topographic features) of the mountain channels low-level flow such that areas of enhanced convergence and upward vertical motion are created. Upward vertical motion is also enhanced where different sea breeze systems converge at points inland. These areas with enhanced upward vertical motion may be characterized by precipitation.

1.3.6 Mountain–mass effect.

The mountain-mass effect influences climate on the mountain itself, hence precipitation distribution. The mountain–mass effect also known as the Massenerhebung effect was introduced by [de Quervain \(1903\)](#) to explain the observed tendency for temperature-related parameters (e.g., snow line, timber line or forest line) to occur at higher elevations in the central Alps than on their outer margins ([Barry, 1992](#)). It occurs because the ground at high altitudes on mountainous areas acts as the main direct heat source for the atmosphere ([Pan et al., 2021](#)). This is because the high altitude mountainous ground receives more solar radiation than that in non-mountainous areas. Consequently, the high altitude mountain terrain is warmer than the surrounding air. This results in greater heat transfer to the atmosphere. The heating of the high altitudes mountainous areas causes the internal climate of a mountain range

to be relatively dry, with minimal precipitation. The Massenerhebung effect is influenced by a number of factors. For instance, depending on whether there is a mountain range or an isolated hill/mountain the effect may be different. The mountain-mass effect is more pronounced on mountain ranges than on isolated mountains/hills because of wind shadowing and heat retention. That is, the timberlines will be higher in mountain ranges than on isolated mountains. The Massenerhebung effect is more pronounced in the interior of mountain ranges than at the margin of mountainous areas. The mountain size also influences the mountain-mass effect. The larger the mountain, the higher the upper limit of plant growth and the higher the corresponding vertical vegetation zone boundary. The mountain-mass effect creates a unique local climate on the mountain itself. This is because, compared with lowland areas, the air pressure, temperature, and humidity are lower in the mountain; however, sunshine and radiation are more intense, and rainfall is observed at a certain height.

However, the above mechanisms seldom occur in isolation. In most cases, they can occur together in non-linear ways. Sometimes, they may reinforce one another in enhancing or reducing precipitation over a certain part of a mountain; other times, they may act against one another in modulating the precipitation over the same part of the mountain. Hence, understanding and predicting the complex interactions of these atmospheric processes in inducing precipitation over the mountains requires the use of atmospheric models.

1.4 Atmospheric models

Global Climate Models (GCMs) are main tools for simulating weather and climate (Giorgi and Mearns, 1991). To simulate the weather or climate, GCMs represent the globe as a collection of grid cells. The size of each grid cell is defined in three Cartesian coordinates directions: x (longitude), y (latitude), and z (altitude). The size of a grid cell in each Cartesian coordinate direction represents the resolution in that direction. Large size grid cells imply coarse (low) resolution whereas small size grid cells imply high resolution. During the simulation, the average condition of weather variables (e.g. humidity, surface pressure, temperature, and winds) at each grid cell is forecasted. The atmospheric processes that take place at the scale of the grid size are called grid scale processes whereas processes that take place at a scale less than the size of a grid scale are called subgrid-scale processes. Models can explicitly resolve processes that occur at a larger scale than their grid size but not those at a lower scale than their grid size (i.e. sub-grid scale processes). The sub-grid processes are usually represented in GCMs with parameterization schemes.

The horizontal resolution of most GCMs is of the order of hundreds of kilometres. At this resolution, GCMs can reasonably simulate synoptic-scale processes and capture the dominant dynamics of global scale systems to a remarkable degree, but they would perform poorly in simulating local-scale processes and the associated precipitation over mountains (Legates, 2014; Joubert and Hewitson, 1997; Dedekind et al., 2016). A reliable simulation of precipitation over mountains requires a high horizontal resolution that can resolve important local-scale processes over the terrain (Giorgi, 1990). Running a GCM with such a high horizontal resolution is usually computationally expensive. There are three alternatives to solving this problem: (i) statistical downscaling; (ii) regional climate modelling; and (iii) variable resolution GCM.

1.4.1 Statistical Downscaling.

Statistical downscaling is a technique that uses statistical models to spatially refine the GCM simulation output and bridge the spatial scale gap between coarse and fine scale. A statistical downscaling model

works by establishing the empirical (linear or non-linear) relationships between large-scale atmospheric variables (i.e. the coarse GCM simulations) and the local scale climate variables using the historical data (Wilby and Wigley, 1997). After determining and validating the model parameters, the model would be applied to predict the future values of the climate variable, using the future atmospheric variable from the GCMs as input. The statistical downscaling approach is very good for producing climate projections over specific sites.

However, the statistical downscaling approach assumes that the relationship between large-scale and local-scale climate in present climate will remain the same (stationary) in projected future climate (Wilby and Wigley, 1997; Hewitson and Crane, 2006). The validity of such an assumption can not be fully assessed. In addition, the approach is not dynamically consistent. For example, a projected change in precipitation may not be dynamically consistent with that of other variables (e.g., humidity and temperature). In addition, statistical downscaling does not account for the feedback from local scale features (topography, land use and land cover change) which can either amplify or attenuate the projected climate change signal (Hewitson and Crane, 2006; Thrasher et al., 2012).

1.4.2 Regional climate modelling.

In contrast to statistical downscaling, the regional climate modelling technique uses physically based models to spatially refine GCM simulation output and bridge the spatial scale gap between coarse and fine scale. It consists in nesting or embedding a fine mesh Regional Climate Model (RCM) or Limited Area Model (LAM) within the grids of a GCM (Giorgi and Mearns, 1999). RCMs generally include the mathematical representation of the main atmospheric dynamical and physical processes as in GCMs. They include detailed descriptions of air dynamics, radiative transmission, cloud and precipitation formation, boundary layer and surface physics processes, and radiative transfer. With the RCMs technique, initial and time-varying meteorological lateral boundary conditions for high-resolution RCM simulations are derived from large-scale meteorological fields (surface pressure, water vapour, temperature, and wind components required to conduct an RCM) derived from GCM runs. Depending on whether one-way or two-way nesting was established, the RCM-simulated circulations could provide input to the driving GCM. With one-way nesting, circulations formed in the RCM subregion with higher resolution do not feed back into the GCM domain with lower resolution. In particular, the coarse resolution GCM grid is solved first, and its output is then used as time-varying boundary conditions to the finer resolution RCM grid. In contrast, with two-way nesting, circulations simulated by the RCM provide input to the driving GCM. Specifically, the GCM coarse grid and RCM fine grid are simultaneously solved, and features from each grid are input into each other at every time step. This downscaling technique is predicated on the notion that the GCM provides the response of the global circulation to large-scale forcings, whereas nested RCMs may account for the effects of local, sub-GCM grid scale forcing. The RCM approach adds value to the GCM simulation as its fine grid allows it to resolve local scale forcings like topographic variations, thereby producing a more realistic and more detailed simulation. It also reduces the computation cost of running a high-resolution simulation over the whole earth. Unlike statistical downscaling, the RCM results are dynamically consistent.

However, the RCM methodology has certain limitations. First, the abrupt shift in grid size at the lateral boundaries (between RCM and GCM) can affect wave propagation and reflection characteristics (i.e., lateral boundary conditions problem; Giorgi and Mearns, 1999). Second, faults in the driving GCM's large-scale circulations are transferred to the nested model (i.e., garbage in, garbage out issue). For example, the nested model will reflect the misplacement of a large-scale circulation feature by the GCM. This issue originates from the failure of GCMs to reproduce regional characteristics of large-scale circulation patterns accurately. Thirdly, the interpretation of disparities between the GCM and

RCM data is difficult if the GCM and RCM utilize distinct physics parameterization systems (physics adequacy issue). This variation could be the result of various forcing resolutions or distinct physical methods. Fourthly, the location of the region, its lateral limits, the size of the domain, and the model resolution all influence the RCM simulation outcomes over a region. For example, the larger the influence of the lateral boundary condition error on the model solution, the smaller the domain size and the closer an area is to the lateral boundaries. Consequently, the RCM domain must be sufficiently large to permit full development of internal model mesoscale circulations and contain relevant regional forcings, but the resolution must be suitable to reflect the scale and impacts of such forcings. Fifthly, the technical effort of setting up two-way interacting experiments between GCM and LAM frequently outweighs the anticipated benefits of such an endeavour.

1.4.3 Variable-resolution GCMs.

A Variable resolution GCM (VGCM) technique simulates regional climate using a GCM with a variable-mesh grid. Unlike traditional GCMs, VGCMs can enhance their horizontal resolution locally over the region of interest. The variable-mesh grid employs smoothly altering grid spacings to locate the region of interest over the finer mesh. The VGCM method has numerous advantages over the RCM method. It is not affected by lateral boundary condition issues. Naturally, VGCMs permit bidirectional interactions between local-scale and large-scale circulation. The deployment of VGCM for regional climate simulation is simpler from a technical standpoint than RCM downscaling.

However, the VGCM approach also has some downsides. First, although using this approach is computationally cheaper than using uniformly high-resolution GCM, it is more computationally expensive than the statistical and regional climate downscaling approaches, because in a VGCM simulation, the low and high-resolution grids use the same time-step, and the size of time-step is determined by the size to the highest resolution.

Given that each of the three downscaling approaches has its advantages and disadvantages, it is essential to combine the three techniques in investigating the performance of three approaches in simulating precipitation over mountains. That is the approach used over the Drakensberg in the present study.

1.5 Motivation for the study

Despite the socio-economic importance of the Drakensberg to the Southern African region, there is a dearth of information on the spatio-temporal characteristics of rainfall over the Drakensberg. This is due to the paucity of long-term observation data over the mountain range. Because of the remoteness and inaccessibility of high-altitude areas, most of the South African Weather Services (SAWS) stations are confined to the foothills of the Drakensberg at altitudes below 1800 m (Nel, 2008). While past studies (e.g. Tyson et al., 1976; Preston-Whyte and Tyson, 1988; Nel and Sumner, 2005) agree on the dependence of precipitation on elevation over the mountain range, they disagree on the magnitude and spatial distribution of the annual precipitation. For example, Tyson et al. (1976) indicated that precipitation over the Drakensberg generally increases with altitude, but Nel and Sumner (2006) found that, below 2100 m above sea level, the precipitation increases with both altitude and eastward distance from the mountain's peak. The discrepancy may be due to different approaches used in interpolation or extrapolation of the sparse rainfall data. For more robust information, there is a need to supplement the observation data with satellite, reanalysis and model simulation datasets in studying the characteristics of precipitation over the Drakensberg.

Rainfall prediction over the mountains during weak synoptic conditions is a challenge (Phillips et al.,

2004). While global climate models perform well in simulating the rainfall distribution during moderate or strong synoptic scale when the local scale processes are suppressed (Pielke, 1984; Paegle et al., 1990; Barros and Lettenmaier, 1994; Markowski and Richardson, 2011; Lennard and Hegerl, 2015), they perform poorly in predicting the rainfall pattern during weak synoptic conditions (WSC) when the local-scale processes are active (Phillips et al., 2004). For example, Phillips et al. (2004) found that the CAM2 model forecast skill drops rapidly in boreal summer when midlatitude synoptic control is weaker. The convective nature of the rainfall over the Drakensberg (Blamey et al., 2017; Tyson and Preston-Whyte, 2000) during the summer months also makes it difficult to forecast because convection initiation is difficult to predict under WSCs (LaCorte, 1999; Stensrud and Fritsch, 1993). However, no rainfall studies over the Drakensberg have documented precipitation characteristics under WSCs. Therefore, some important questions remain unanswered regarding rainfall distribution over the Drakensberg during WSCs. For example, how often does WSC occur over the Drakensberg? What percentage of annual precipitation falls during WSC? What are the major rainfall patterns over the Drakensberg during WSC? How well do reanalysis datasets (e.g. CFSR) reproduce these major rainfall patterns? To what extent can downscale of the reanalysis datasets with regional weather or climate models improve the simulation of these rainfall patterns, and what is the lowest model resolution for doing so? As answers to these questions may improve weather and seasonal forecasts over the Drakensberg, the present study intends to improve knowledge in this area.

Precipitation patterns are expected to change with Global Mean Temperature rise to different levels above pre-industrial levels (Schleussner et al., 2016), however, it is not clear what impact this may have on precipitation characteristics over the Drakensberg. The Paris Agreement aims to keep the rise in global temperature to 1.5 or 2°C above the pre-industrial levels. But, there is a scarcity of information on how rainfall patterns over the Drakensberg could respond to different levels of global warming. This is the focus of this thesis.

1.6 Aims and objectives

This thesis aims to study the characteristics of precipitation over the Drakensberg, examine the capability of climate models to simulate the characteristics and project the impacts of climate change on the characteristics. To this end, the objectives of the thesis are:

- Examine the characteristics of rainfall distribution under weak synoptic conditions over the Drakensberg.
- Evaluate the capability of two climate models in simulating the characteristics of rainfall over the Drakensberg.
- Assess the potential impacts of climate change on characteristics of precipitation over the Drakensberg at various global warming levels (GWLs) .

1.7 Thesis outline

This thesis consists of seven chapters. **Chapter 1** (this chapter) provides a background for the study, highlights the importance of the Drakensberg, and discusses some of the factors that control precipitation over mountains and introduces atmospheric models. Finally, it presents the motivation for the study as well as the aims and objectives.

Chapter 2 is the literature review chapter, where relevant past studies are reviewed to provide a com-

pressive overview of previous findings on characteristics and drivers of precipitation over the Drakensberg and to expose the challenges involved in simulating precipitation over the Drakensberg.

Chapter 3 is the methodology chapter that describes the datasets, climate models, simulation experiments, and data analysis methods used in the study.

Chapters 4 - 6 present and discuss the results of the study. Chapter 4 focuses on characteristics of rainfall over the Drakensberg on weak synoptic days; Chapter 5 compares the capabilities of an RCM and a VGCM in simulating the widespread extreme rainfall events over the mountain, and Chapter 6 reports impacts of climate change on rainfall over the Drakensberg.

Chapter 7 provides concluding remarks and offers recommendations for future work.

It should be noted that different study periods are used in results and discussion chapters (Chapters 4 - 6) depending on focus of the chapters. For example in chapter 4, the period 1983 – 2012 is used to examine rainfall distribution under weak synoptic conditions. In chapter 5, the period 1987 – 2016 is used to study extreme rainfall distribution over the Drakensberg. And, in Chapter 6, which examines the projected impacts of climate change on rainfall over the Drakensberg, the datasets used spanned the period 1950 – 2100. The pre-industrial period is defined as the period between 1861 – 1890 and the reference period is defined as 1971 – 2000. Each CORDEX and NEX downscaled dataset has different future period based on the global warming levels of the global climate model simulations they downscaled.

CHAPTER 2

Literature review

This chapter provides a comprehensive review of past studies on precipitation characteristics over Southern Africa and the Drakensberg in particular. The chapter starts with studies on forms and spatio-temporal distribution of precipitation over the Drakensberg then moves to studies on factors controlling precipitation over Southern Africa and the Drakensberg. It also discusses some studies on the challenges identified in the literature on simulating precipitation characteristics over South Africa and the Drakensberg, reviews past studies that projected future changes in temperature, precipitation, and extreme precipitation over Southern Africa.

2.1 Characteristics of precipitation over the Drakensberg

Several studies have attempted to describe the characteristics of precipitation over the Drakensberg (Tyson et al., 1976; Nel and Sumner, 2005, 2006; Nel, 2008, 2009; Schulze, 1979; Mulder and Grab, 2009; Taylor et al., 2016). Their descriptions focused on the temporal and spatial distribution of forms of precipitation (i.e. fog, hail, mist, snow, and rainfall) over the Drakensberg. For example, Tyson et al. (1976) analysed fog interception data over a station at Cathedral peak (which was the only station with such data) over a four-year period. They found that the highest amount of Fog occurs in November (about $70mm$) and the least in June (about $4mm$). They also found that fog occurs on days with and without rainfall. Over the four years, fog amount was found to exceed rainfall amount on 65% of precipitation days in January and 82% of precipitation days in October. The authors reported that hail occurs in about $8days\ year^{-1}$ over the Drakensberg but that this value drops as one moves away from the Drakensberg, suggesting that the mountain plays a crucial role in hail occurrences. However, hail is most frequent in November or December and is generally recorded in the same zones where thunderstorms occur (Tyson et al., 1976). Tyson et al. (1976) and Morris et al. (2021) acknowledged that that mist is very frequent over the Drakensberg, but the statistics of the occurrence of mist are missing in literature.

The spatial-temporal characteristics of snow over the Drakensberg is well discussed in literature (Nel and Sumner, 2008; Sene et al., 1998; Nel and Sumner, 2005; Tyson et al., 1976). Most studies indicate that snow is mainly recorded around the mountain summits but the incidence varies with altitude. For example, Mulder and Grab (2009) found that snow incidences increase with altitude to about $3250m$ elevation and remain constant above this height. Lower altitudes only receive snow during severe snow events when all locations along the Drakensberg become snow-covered. The authors also found that the highest seasonal incidence of snow cover over the Drakensberg occurs in June - August (63% of the annual total) while the highest monthly incidence is in August (29% of the annual total). They indicated that, in May, the snow spreads across the whole Drakensberg but only above $3000m$ elevation; whereas, in September, the snow cover occurs only at the central and southern Drakensberg regions but extends below $2800m$ altitude. Nevertheless, there is a controversy in literature on the annual frequency of snow events over the Drakensberg (Nel and Sumner, 2008; Sene et al., 1998; Nel and Sumner, 2005; Tyson et al., 1976). While Mulder and Grab (2009) reported about 2.5 snowfall events per year, Tyson

et al. (1976) reported eight events per year, and Sene et al. (1998) reported five to ten snow events from June to July alone. The controversy may be due to the differences in data sources used and in methods employed in the studies. For example, the results of Tyson et al. (1976), which is the most cited in the literature (Nel and Sumner, 2008), were based on newspaper reporting for a 14 years period while the Mulder and Grab (2009) results were based on satellite images over a more recent 16-year period (1989 – 2004). However, there is no literature on the exact contribution of snowfall to precipitation totals over the Drakensberg.

Previous studies indicated that the Drakensberg receives more than 70% of its annual rainfall in October – March and less than 10% in May–August months (Nel and Sumner, 2005, 2006; Nel, 2007; Nel and Sumner, 2008; Nel, 2009; Schulze, 1979; Tyson et al., 1976; Sene et al., 1998; Mulder and Grab, 2009). However, while the studies agree that the annual rainfall varies markedly with altitude, they disagree on the pattern of variation and the estimated annual rainfall at mountain's top. Early studies (e.g., Tyson et al., 1976; Schulze, 1979; Sene et al., 1998) assumed the annual rainfall increases linearly with elevation (up to the mountain's top, above 3000m *a.s.l.*). For example, Tyson et al. (1976) found annual rainfall of 700mm at lower altitudes of the Drakensberg and used it to estimate the annual rainfall to be more than 2000mm at the top of the escarpment. In the same vein, Schulze (1979) estimated annual rainfall to exceed 1800mm at the mountain top. Sene et al. (1998) reported a linear positive relationship between elevation altitude and rainfall in different sections of the Drakensberg. They showed that along the eastern escarpment, the annual rainfall increased from about 800mm (at 1100m *a.s.l.* in South Africa) to 1200mm (at 3000m *a.s.l.* in Lesotho), indicating an increase of 51mm per 100m rise in elevation. Along the Maloti Mountains in the western half of Lesotho, the annual rainfall was about 800mm per annum, meaning an increase of 48mm per 100m rise in elevation. And along the western escarpment, the annual precipitation was only 600mm (possibly due to a rain shadow), suggesting a 27mm increase per 100m rise in elevation. However, contemporary studies by Nel and Sumner (2005, 2006, 2008) argued that annual rainfall does not increase monotonically with altitude over the Drakensberg. Nel and Sumner (2006) indicated that the linear increase of precipitation with altitude is only significant for elevation below 2100m *a.s.l.*, and it becomes uncertain above 2100m *a.s.l.* Observation data collected by Nel and Sumner (2005) from the escarpment showed that the annual rainfall values are lower above 2800m *a.s.l.* than below 2800m *a.s.l.*, thereby challenging the assumption of linear increase in rainfall with elevation in prior studies.

Hence, it is not very clear whether maximum rainfall on the Drakensberg escarpment occurs along the slope or at the crest. The location of this maximum rainfall may be dictated by several factors such as the shape and size of the mountain, mountain-induced circulations, or by the interaction between the mountain induced circulations and the large scale rain-producing systems (synoptic conditions). The issue is exacerbated by the lack of data for the area (Tyson et al., 1976; Nel and Sumner, 2005) and deeply dissected nature of the terrain that makes extrapolation from station to station extremely difficult Tyson et al. (1976). Therefore, more studies are needed to understand the spatial variability of rainfall over the Drakensberg. The current thesis uses a combination of satellite observation datasets, reanalysis products, and climate model simulations to examine rainfall characteristics over the Drakensberg.

2.2 Factors controlling precipitation over the Southern Africa

Several studies have documented the regional and global scale circulation features influencing rainfall variability over Southern Africa (Mason and Jury, 1997; Mason, 2001; Jury et al., 2004; Reason and Jagadheesha, 2005; Taljaard, 1986; Tyson and Preston-Whyte, 2000; de Sousa Pinto, 2015; Rouault et al., 2003; Cook et al., 2004; Ndarana et al., 2021; Dieppois et al., 2016). They showed that these

circulation features influence the rainfall variability at different time-scales. This section focuses on the features that control rainfall variability at (i) inter-annual to decadal scale and (ii) seasonal scale.

2.2.1 Inter-annual to decadal precipitation variability.

Large-scale (global) atmospheric features such as the El Niño-Southern Oscillation (ENSO), the Quasi-Biennial Oscillation (QBO), and solar activity have been found to influence inter-annual to decadal rainfall variability over Southern Africa (Mason and Jury, 1997; Jury et al., 2004; Mason, 2001; Reason and Jagadheesha, 2005; Dube, 2002). ENSO, which refers to a change in the sign of the east-west atmospheric pressure gradient across the tropical Pacific and Indian Oceans as a result of sea-surface temperature (SST) in the central and eastern Pacific, has two active phases known as El Niño and La Niña. While El Niño occurs when tropical SSTs in the central and eastern Pacific oceans are warmer than the multi-decadal climate average (Wallace and Hobbs, 2006), La Niña occurs when tropical SSTs in the central and eastern Pacific oceans are cooler than the multi-decadal climate average. However, it is well understood that ENSO has global climate implications, particularly for rainfall anomalies over much of Southern Africa and the Drakenberg Mountains (Mason and Jury, 1997). Mason (2001), for example, discovered that December-February precipitation over the Drakensberg was lower than normal during the eight warmest El Niño episodes between 1950 and 1996/87. Kane (2009) attributed the drop in precipitation over most of South Africa from October 1982 to April 1983 to an El Niño event.

The Quasi-Biennial Oscillation (QBO) was also discovered to have an impact on rainfall over South Africa (Kane, 2009; Mason and Tyson, 1992; Mason and Jury, 1997). With a mean period of 28 to 29 months, QBO is a quasi-periodic oscillation of the equatorial zonal wind between easterlies and westerlies in the tropical stratosphere. It influences stratospheric flow from pole to pole by modulating extratropical wave effects (Baldwin et al., 2001). QBO-induced circulation changes have an impact on atmospheric chemical constituents such as methane, ozone, and water vapour (Mason and Tyson, 1992). QBO influences variability in the mesosphere near 85km by selectively filtering waves propagating upward through the equatorial stratosphere, and it may also influence the strength of Atlantic hurricanes (Baldwin et al., 2001). Droughts occur during warm phase years like 1991 – 92 when QBO is in its easterly phase, according to Mason and Jury (1997). Wet conditions occur when it is in its westerly phase.

It has also been reported that solar activity influences annual rainfall in South Africa (Dyer, 1975; Alexander and Emeritus, 2005; Mason and Tyson, 1992). Solar activity refers to solar surface processes such as solar flares, sunspots, coronal mass ejections, solar winds, solar radiation bursts, and so on (Usoskin, 2017; Li et al., 2017). Solar activity varies over the course of an 11-year solar cycle, and this variation manifests itself in various ways (Usoskin, 2017). Mason and Tyson (1992) and Alexander and Emeritus (2005) demonstrated that solar activity influences rainfall. According to Alexander and Emeritus (2005), the 21-year period of South African annual rainfall is directly related to the double sunspot cycle. The link between the double sunspot cycle and annual rainfall is statistically significant at the 95 percent level, whereas the link between the single (11-year) sunspot cycle and annual rainfall is not. The transition between double and single sunspot cycles is usually associated with abrupt precipitation changes, from low rainfall (drought) to high rainfall (floods). These reversals correspond to sudden increases in annual sunspot numbers as well as reversals of solar magnetic polarity at sunspot minima. Increased solar activity increases the frequency and magnitude of widespread, heavy rainfall-producing systems (Alexander and Emeritus, 2005). For quiescent periods, the opposite is true. Dyer (1975) discovered a statistically significant correlation between South African annual rainfall and double solar cycles (20 years). Dyer (1975) discovered that the solar influence on annual rainfall over Southern Africa is latitudinal.

However, research has shown that South African rainfall is also affected by the complex interaction of ENSO, solar activity, and QBO (i.e., Kane, 2009; Mason and Tyson, 1992; Mason and Jury, 1997). Mason and Tyson (1992), for example, demonstrated that the initial QBO phase modulated the effects of solar activity on rainfall in Southern Africa (easterly or westerly). They discovered significant correlations between rainfall and solar activity in both South Africa's winter and summer rainfall regions. These correlations were only significant when the QBO was in an easterly phase. When the QBO is in the easterly phase, solar activity in the three months before explains more than 50% of the differences in late summer (January–March) rainfall over summer rainfall area in most of South Africa and more than 60% of the differences in late winter (July–September) rainfall over winter rainfall area (i.e., the southwest Cape). During this phase, an increase in early-season solar activity (April–June in the winter rainfall area and October–December in the summer rainfall area) causes an increase in rainfall in both the winter and summer rainfall area at the same time. When solar activity goes up (or down), it makes it rain less (or more) in the same areas three months later, in the second half of the same rainy season. When the QBO is in its westerly phase, the summer rainfall in the winter rainfall area and the winter precipitation in the summer rainfall area can change out of season. These changes tend to happen when solar activity goes up (or down). Mason and Tyson (1992) found that ENSO has a bigger effect on rain in Southern Africa when QBO is in its westerly phase.

However, while the thesis would study the inter-annual to decadal variability of rainfall over the Drakensberg, the emphasis would not be on the factors influencing the rainfall variability.

2.2.2 Seasonal and intraseasonal rainfall variability.

The seasonal rainfall variability over Southern Africa is influenced by regional-scale features like Intertropical Convergence Zone (ITCZ) and Tropical Temperate Troughs (TTT).

The ITCZ is a location where northeasterly trade winds from the northern hemisphere and south easterly trade winds from the southern hemisphere meet (Stull, 2015). Some authors have referred to it as the meteorological equator. The region of convergence displaces itself between about 10° north and south of the equator (Nicholson, 2018). During August and September it is located at about $10^{\circ}N$ whereas during February and March it is located at about $10^{\circ}S$. The ITCZ is characterised by hot and humid air, strong rising air motion, low pressure, and light to calm winds. This north-south displacement of the ITCZ influences the cycle of the rainfall seasons over the tropics (Nicholson, 2018). Prior studies have also shown that the ITCZ influences South African rainfall (Cook et al., 2004; Ratna et al., 2013). Cook et al. (2004) found that during wet January-February-March (JFM) months, the ITCZ is strengthened over tropical southeastern Africa and shifts southwards when there is relative convergence over Mozambique, Zimbabwe and Zambia. During dry JFM months, relative divergence weakens the ITCZ. Ratna et al. (2013) showed that the seasonal rainfall in the northern part of Southern Africa and Madagascar are associated with the southernmost position of the ITCZ.

A tropical temperate trough (TTT) is a diagonally oriented cloud band extending over the landmass from northwest of tropical Africa to the south east of the mid-latitude in Africa and the southwest Indian Ocean (see Figure 2.1). It links tropical and midlatitude circulation systems (Harangozo and Harrison, 1983; Macron et al., 2014; Ratna et al., 2013) and also contributes to transfer of energy and momentum between the tropics and the mid-latitudes. The cloud-band is formed when lower tropospheric disturbances in the tropics are associated with midlatitude (Southern Africa) troughs in the upper atmosphere (Harangozo and Harrison, 1983; Ratna et al., 2013). Prior studies have reported that TTT is a dominant rainfall producing system in Southern Africa during austral summer (Ratna et al., 2013; Macron et al., 2014; Hart et al., 2013; Diab et al., 1991; Crimp et al., 1998). Hart et al.

(2013) found that TTT accounts for 30 – 60% of wet days (days with rainfall greater than or equal to 1mm) over south Africa increasing from east to west. It also contributes about 30 – 50% of rainfall during the summer months. Strong TTT events over Southern Africa cause extreme rainfall events which generally causes flooding. Hart et al. (2013) found that out of 52 extreme rainfall events during the period 1979 – 1999, 30 were associated with TTT. TTT mainly occurs during October to March producing rainfall for, on average, 3 – 4 days per event. This accounts for a mean contribution of about 48 rain days in the summer season.

Diab et al. (1991) investigated the percentage contribution of eight synoptic types (i.e, TTT, tropical cyclone, Mid-latitude cyclone, Easterly flow, High-pressure, Westerly Wave, East coast low, and Ridging High) to the total annual rainfall at each station in Natal (present day KwaZulu-Natal, location of the Drakensberg) using rainfall data from 310 stations for the period extending from 1965 – 1985. They concluded that TTT is the single most important rainfall producing system over Natal; TTT alone contributes 28% of the integrated annual rainfall, followed by westerly wave type (24%). Todd and Washington (1999) showed that TTT induces convection over Southern Africa whereas they suppress convection over eastern Africa and Madagascar. Some TTT events propagate eastward from the Southern African landmass to the Mozambique Channel and Madagascar (Ratna et al., 2013). The location of the TTT has a strong influence on intraseasonal as well as interannual rainfall variability (Macron et al., 2014; Todd and Washington, 1999). Woodborne et al. (2015) found that this zonal (East/west) displacement of TTT modulates rainfall amounts.

However, while these studies have focused on the impacts TTT over South African precipitation, there is a dearth of information on how TTT could influence the characteristics of precipitation over the Drakensberg. The present thesis would fill this gap.

2.2.3 Botswana High.

Recent studies have also shown that the Botswana high contributes to rainfall over the Drakensberg. The Botswana high occurs in the subtropics at upper levels (best expressed at 500hPa) over western Botswana and eastern Namibia during austral spring, summer and autumn (Reason, 2019; Maoyi and Abiodun, 2022; Driver and Reason, 2017). It forms in August and then intensifies and moves southward over Southern Africa during the spring and summer (Driver and Reason, 2017). Driver and Reason (2017) showed that Botswana High influences summer rainfall variability over Southern Africa at seasonal and interannual time scales. A strengthened Botswana high is associated with reduced rainfall over Southern Africa (Driver and Reason, 2017) because the strengthening is associated with enhanced subsidence that suppresses moisture convergence and the development of TTT (Maoyi and Abiodun, 2022) which are known to contribute rainfall over the Drakensberg. On the other hand, the weakening of the Botswana high allows deep convection and significant rainfall to occur (Reason, 2019). The variability of the Botswana High also influences maximum and maximum temperature extremes as well as the frequency of dry spells during summer (JFM) (Maoyi and Abiodun, 2022). The strength of the Botswana high is also influenced by ENSO. It is strengthened during El Niño events but weakens during La Niña events. For instance, it has been found that during the intense 1997/1998 El Niño event, the anomaly in the Botswana high was less than the weaker 1986/1987 El Niño event (Maoyi and Abiodun, 2022; Driver and Reason, 2017).

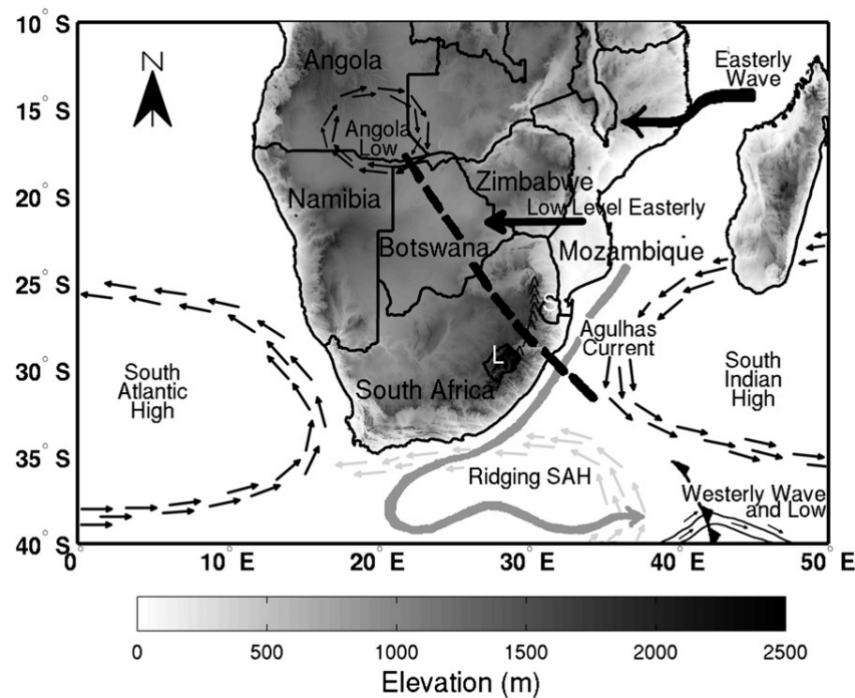


Figure 2.1: Austral summer season synoptic features. The broad dashed line lying diagonally across the continent represents the mean position of cloud bands in the region (TTTs). Note that the letters **L** and **S** are for Lesotho and Swaziland. Also depicted are the Angola low, Easterly wave, South Atlantic high (SAH), Ridging high (SAH Ridge), South Indian high (SIH), Westerly wave and low (source: [Blamey and Reason, 2013](#)).

2.3 Southern African weather producing systems and precipitation over the Drakensberg

Previous studies have identified several weather producing systems over Southern Africa and grouped them into temperate, subtropical and tropical weather systems ([Diab et al., 1991](#); [Mulder and Grab, 2009](#)). The temperate systems include cold fronts and westerly waves; the subtropical systems include the South Atlantic, South Indian ocean and continental Anti-cyclones; whereas, the tropical weather systems include easterly waves. This section would focus on the systems that contribute to rainfall over the Drakensberg, including their complex interaction.

2.3.1 The Ridging High.

A ridging high (see Figure 2.1) is a South Atlantic Ocean high pressure cell that extends east such that its leading edge amalgamates with the South Indian Ocean high ([Ndarana et al., 2021, 2022](#); [Diab et al., 1991](#)). All past studies on ridging highs agreed that ridging highs play a crucial role on Southern African weather by transporting moisture from different locations of the surrounding oceans into the continental landmass and by interacting with other weather systems over Southern Africa ([Taylor et al., 2016](#); [Diab et al., 1991](#); [Ndarana et al., 2021, 2022](#)). For example, [Taylor et al. \(2016\)](#) and [Diab et al. \(1991\)](#) showed that ridging highs advect moist air from Indian Ocean the eastern escarpment, causing orographic rain and thunderstorms. [Ndarana et al. \(2021\)](#) showed that Ridging highs play an important role in moisture transport during the evolution of TTT and even contribute more to summer rainfall days

(60%) than TTT contribute (21%). More recently, [Ndarana et al. \(2022\)](#) found two types of ridging high over Southern Africa (i.e., Type-S and Type-N), based on the latitudinal location of the riding high events. The S-type are ridging events that occur south of the 40°S latitude while the Type-N are those that occur to the north of it. Discussing the differences in the severity of the rainfall associated with the different types of ridging highs, [Ndarana et al. \(2022\)](#) noted that Type-S ridging highs, which transport more moisture to some parts of South Africa especially along the eastern coasts (near the Drakensberg), are associated with heavier rainfall events.

2.3.2 The Angola low.

The Angola low (Figure 2.1) is another weather producing system identified to contribute to rainfall variability over the Drakensberg ([Dedekind et al., 2016](#)) through their association with tropical temperate trough formation. The Angola low is a low pressure system that occurs around the Bie plateau in Angola and extends to Namibia, Botswana and Zambia ([Munday and Washington, 2017](#)). It is also referred to as the Botswana low ([Munday and Washington, 2017](#); [van Heerden and Taljaard, 1998](#); [Tyson and Preston-Whyte, 2000](#)). The Angola low contributes to moisture transport over the subcontinent ([Rouault et al., 2003](#); [Cook et al., 2004](#); [Ndarana et al., 2021](#); [Hart et al., 2010](#)) as well as to the development and intensification of TTT, a dominant summer rainfall producing system around the Drakensberg ([Harrison, 1984](#); [Hart et al., 2010](#)). Prior studies have reported a strong relationship between the strength of Angola low Southern African rainfall ([Hart et al., 2010](#); [Cook et al., 2004](#); [Munday and Washington, 2017](#)). [Munday and Washington \(2017\)](#) showed that the intensification of Angola low is characterised by enhanced local convection, increased westerly moisture transport from the south-east Atlantic and penetration of moisture-bearing north-easterlies deep into the subtropics. [Cook et al. \(2004\)](#) found a 10% increase in the strength of the Angola Low during January–March months of wet years and a decrease of 20% during the same months in dry years.

2.3.3 Cold Front.

There is also evidence that cold fronts contribute to rainfall over the Drakensberg ([Tyson and Preston-Whyte, 1972](#); [Mulder and Grab, 2009](#); [Nel, 2007](#)). A front is the boundary between different air masses which are interacting with one another ([Stull, 2015](#)). Fronts are usually associated with low pressure centres. A cold front is formed when cold air is moving into a region of warm air. Along the cold front, warm air rises rapidly resulting in narrow bands of towering cumuliform clouds, showers and thunderstorms. Past studies (e.g., [Tyson et al., 1976](#); [Mulder and Grab, 2009](#); [Nel, 2007](#)) have noted that cold fronts bring widespread rainfall and snowfall over the Drakensberg region. [Mulder and Grab \(2009\)](#) found that cold fronts account for about 66% of snowfalls over the Drakensberg. The snowfall usually occurs at altitude above 3000m *a.s.l.* However, strong cold front events in austral mid-winter may bring widespread snow to areas below 2600m *a.s.l.* [Grab and Simpson \(2000\)](#) found that about 43 cold front events occur annually over KwaZulu–Natal.

2.3.4 Cut-off lows.

According to the literature, cut-off lows (COL) contribute to precipitation over the eastern parts of South Africa ([Mulder and Grab, 2009](#); [Molekwa et al., 2014](#)). Cut-off lows are cold-cored closed cyclones in the middle and upper troposphere that form in westerly winds equatorial to the polar jet stream ([Molekwa et al., 2014](#); [Favre et al., 2013](#)). When the troughs in Rossby waves extend equatorially and cut off, the air within the COL becomes colder than the surrounding atmosphere. This destabilizes the atmosphere, resulting in deep convection and heavy rainfall ([Omar and Abiodun, 2020](#)). The formation

of COLs over a region is determined by the strength of the westerlies and the position of the jets in the area (Favre et al., 2013; Omar and Abiodun, 2020). It is also affected by the dynamic interaction of the atmosphere and topography (Omar and Abiodun, 2020). Because of the instability caused by the cold pool associated with the cut-off low center, cut-off lows may be associated with intense thunderstorms. They are common between latitudes $15^{\circ}S$ and $40^{\circ}S$ and all over the continent, particularly in the Mozambique Channel and off South Africa's and Namibia's Atlantic coasts (Favre et al., 2013). Cut-off lows over the Drakensberg are typically associated with the passage of one or more cold fronts, according to Mulder and Grab (2009). Cold fronts and associated cut-off lows were responsible for roughly 80% of the snow cover over the Drakensberg. The most intense and widespread snowfalls over the Drakensberg are usually associated with cut-off lows. They account for approximately 15% of the snowfall over the Drakensberg (Mulder and Grab (2009)). The least amount of snowfall due to cut-off lows occurs at altitudes less than 2600m *a.s.l.*, while the most snowfall due to cut-off lows occurs in areas north of Giant Castle. This is most common at altitudes above 3000m *a.s.l.* Snowfall associated with cut-off lows along South Africa's east coast is observed on occasion during late winter or early spring, accounting for about 10% of snowfalls.

However, the literature is divided on the number of synoptic systems that produce precipitation over the Drakensberg. Diab et al. (1991) used rainfall data from 310 stations from 1965 to 1985 to investigate the percentage contribution of eight synoptic types (TTT, Westerly Wave, Ridging high, East coast low, High-pressure, Easterly flow, Mid-latitude cyclone, tropical cyclone) to total annual rainfall at each station in Natal (present-day KwaZulu-Natal, location of the Drakensberg). They discovered that while four synoptic systems (TTT, Westerly Wave, Ridging high, and East coast low) accounted for 81% of the integrated annual rainfall measured at Natal's ten key rainfall stations, the remaining four synoptic systems (High-pressure, Easterly flow, Mid-latitude cyclone, tropical cyclone) accounted for 13%, and other unclassified systems accounted for 6%. Mulder and Grab (2009), on the other hand, identified five synoptic types that can cause precipitation over the Drakensberg, namely: Westerly wave (including cut-off low), Ridging high, mid-latitude cyclones, tropical cyclones, and East coast low (coastal low) (Mulder and Grab, 2009). The disparity in these studies could be attributed to a variety of factors, including a lack of data and methods for identifying synoptic drivers. Diab et al. (1991) used rainfall data from 10 Natal stations, which may not be representative of the entire Drakensberg. However, the current study would investigate the influences and contributions of various synoptic systems on precipitation characteristics over the Drakensberg using a combination of gridded satellite observation, climate model simulation, and the Self-Organising Maps (SOMs) techniques.

2.4 Challenges in simulating precipitation over the Drakensberg

Literature has identified several challenges in simulating precipitation over the Drakensberg (Kalognomou et al., 2013; Tyson et al., 1976; Nel, 2008; Taylor et al., 2016; Mulder and Grab, 2009; Omar and Abiodun, 2017). These include the paucity of observational data, model resolution and model physics parameterization. However this section will only review the challenges that are investigated during the current study.

2.4.1 Paucity of Observational data.

Prior studies suggest that a central difficulty in understanding the precipitation characteristics over the Drakensberg is the paucity of high-quality and long-term records of both the recent past and paleoclimates for the area (Tyson et al., 1976; Nel and Sumner, 2005). The data paucity is primarily due to the sparse meteorological stations coverage and the lack of stations at higher elevations. For

example, (Nel and Sumner, 2005) was the first contemporary study to measure rainfall data at altitudes above 2500m *a.s.l* over the Drakensberg escarpment region. This was due to the fact that previous studies (Tyson et al., 1976; Schulze, 1979) had derived rainfall at higher elevations by estimation from stations at lower altitudes. Nel and Sumner (2005) findings challenged the initial estimations from those studies. In addition, Tyson et al. (1976) indicated that while investigating the climate of the Drakensberg, they generalised rather more than would otherwise have been done. Tyson et al. (1976) and Nel and Sumner (2005) found there are no continuous snowfall records available for the Drakensberg area. Tyson et al. (1976) also mentioned that snow recordings are not kept systematically at any station in the Drakensberg area and they obtained information about snow by analysing newspaper reporting of snow over a 14-year period. The paucity of data over the Drakensberg poses significant challenges in validation of RCM/GCM simulations (Joubert and Hewitson, 1997) as well as model initializations. Joubert et al. (1999) noted that limited-area models may be nested within observational analyses. Therefore, the lack of such data poses a challenge for such studies over the Drakensberg. Climate modelling studies usually compare observed data with model output to determine whether the model is capturing well the process (e.g. precipitation) being investigated. To this end, observation data is crucial as they provide a benchmark against which to compare model output. Hence, it may be difficult to perform cause and effect analysis (attribution) and detect changes (natural variability). Despite the availability of satellite and reanalysis data in recent years, observational uncertainty between different observation datasets still poses a challenge. Omar and Abiodun (2017) assessed the ability of nine regional climate models to reproduce the characteristics of extreme events along South Africa's east coast (closer to the Drakensberg). Two observation datasets were used to compare the model simulations (GPCP and ERAINT). They discovered some inconsistency between the GPCP and TRMM observation datasets. The intensity of rainfall in GPCP datasets is lower than in TRMM datasets. The level of uncertainty in the observation datasets made model evaluation difficult. Despite the availability of satellite observation datasets in recent years and several reanalysis products, almost no study has examined the rainfall characteristics over the Drakensberg using these datasets. To fill this knowledge gap, the current study explores rainfall characteristics over the Drakensberg using different satellite observations and reanalysis and climate model simulations.

2.4.2 Low model resolution.

Low model horizontal resolution is another challenge in simulating precipitation characteristics over the Drakensberg (Joubert and Hewitson, 1997). For example, the steep topography of the Drakensberg (eastern escarpment) is known to create issues with climate models by causing the models to generally overestimate rainfall totals (Note that this list includes RCM studies as well; Joubert et al. (1999); Engelbrecht et al. (2002, 2009); Nikulin et al. (2012); Jury (2012); Hernández-Díaz et al. (2013); Dedekind et al. (2016); Haensler et al. (2011)). Haensler et al. (2011) has shown that using a high resolution simulation over Southern Africa can improve precipitation simulation.

As discussed in Chapter 1, one way of improving results from low resolution GCMs is to employ a statistical downscaling approach. Few studies have employed statistical downscaling approaches over South Africa as a whole or over specific regions of south Africa. Hewitson and Crane (2006), for example, used the statistical downscaling approach to downscale daily precipitation over South Africa. They predicted that summer rainfall in South Africa would increase over the convective region of the central and eastern plateaus, as well as the Drakensberg Mountains. The Western Cape would experience little change, with some summer drying and a slight decrease in winter frontal rainfall. They discovered that the projected changes using the statistical downscaling approach were consistent with GCM forcings, consistent in pattern across different GCMs, and defensible in terms of our understanding of the physical

processes underlying the change. Abiodun et al. (2019) examined extreme rainfall events in Southern Africa and over 12 major cities in the region using statistically downscaled datasets. However, none of these studies have explicitly focused on the Drakensberg which is known to be a challenge for climate models. The current study will use statistical downscaled datasets (Thrasher et al., 2013) to study past, present and future effects of climate change on precipitation characteristics over the Drakensberg.

Another approach that has been used in previous studies to improve the GCM results is nesting RCMs within GCMs. Some studies (Joubert et al., 1999; Engelbrecht et al., 2002) over Southern Africa (the Drakensberg region) have found that nesting an RCM within a GCM results in more accurate and detailed simulation of weather and climate. For instance, Engelbrecht et al. (2002) investigated the possibilities and limitations for nesting the Australian Commonwealth Scientific and Industrial Research Organisation (CSIRO) Division of Atmospheric Research Limited-Area Model (DARLAM) into CSIRO-9 GCM to produce high-resolution climate simulations over Southern Africa. They found that the DARLAM RCM provided a more detailed simulation of climate over the Southern Africa region than the CSIRO-9 GCM. They suggested that the improved simulation may be attributed to the fact that orographic features, which have a significant influence on the climate of the region, are more clearly resolved at the RCM's resolution ($60\text{km} \times 60\text{km}$) than in the GCM (R21 spectral resolution, which is roughly equivalent to 3.2×5.6 degrees latitude-longitude). However, it is not clear from prior studies over the Drakensberg which horizontal resolution could be used to capture the mountain induced processes that influence precipitation formation. Knowledge of the appropriate resolution could help in setting up simulations. In addition, no study has employed an RCM to investigate precipitation characteristics over the Drakensberg under weak synoptic conditions. The current study will attempt to fill these knowledge gaps.

Variable resolution Global climate models (VGCMs) have also been employed to investigate precipitation characteristics over the Drakensberg. For example, Dedekind et al. (2016) evaluated the performance of the Conformal Cubic Atmospheric Model (CCAM), which is a variable-resolution global atmospheric model in representing rainfall totals over eastern escarpment region (the Drakensberg) of South Africa and Lesotho. They found that the model simulates well interannual rainfall variability, rainfall seasonal cycle and rainfall totals over southern and tropical Africa. It also captures the west–east gradient in rainfall over South Africa and the meridional movement of ITCZ-induced rainfall bands. However, the CCAM significantly overestimated rainfall totals over the Drakensberg areas of Southern Africa. Therefore, there is a need to explore the potential of other VGCMs in simulating precipitation characteristics over the Drakensberg. The present study will perform simulations with another VGCM to study the precipitation characteristics over the Drakensberg. The study also evaluates the performance of the different downscaling approaches in simulating precipitation characteristics over the Drakensberg in past, present and future climates.

2.5 Climate change projection over Southern Africa

Several studies have shown that Southern Africa has undergone significant climate change in the past and the change is expected to continue due to global warming (Tyson et al., 1990). This section reviews previous studies on projection changes in temperature and precipitation as well as extreme climate and weather events over Southern Africa.

Previous research conducted over South Africa discovered evidence of increased temperature in the past (Tyson et al., 1990; Joubert, 1994; Joubert and Hewitson, 1997; Engelbrecht et al., 2015; Kusangaya et al., 2014). Unganai (1996); Kruger and Shongwe (2004); Kusangaya et al. (2014); New et al. (2006); Warburton et al. (2005) and Hughes and Balling Jr (1996) discovered a warming trend over Southern

Africa, with minimum temperatures rising faster than maximum temperatures. Levey (1996) observed a 1.5°C increase during the winter season. Jones (1994) found a warming rate of $0.31^{\circ}\text{C decade}^{-1}$, while Karl et al. (1993) discovered an increase in both maximum and minimum temperatures. Tshiala et al. (2011) discovered a $0.12^{\circ}\text{C decade}^{-1}$ increase in annual temperature over South Africa's Limpopo Province. Hulme et al. (2001) concluded that temperatures in Southern Africa were higher in the 1990s than earlier in the century, and that they are currently between 0.2° and 0.3°C higher than the 1961–1990 average. Engelbrecht et al. (2015) discovered that temperatures have been rising rapidly over Africa over the last five decades, faster than the global warming rate, and the increases are statistically significant at most locations by analysing Climatic Research Unit (CRU) datasets from 1961–2010. The largest trends (more than $3.2^{\circ}\text{C Century}^{-1}$) were discovered over subtropical Southern Africa. The study also discovered a $0.8^{\circ}\text{C Century}^{-1}$ temperature trend over the southern Drakensberg and a $1.6^{\circ}\text{C Century}^{-1}$ temperature trend over the northern Drakensberg.

Some studies have projected that future increase over South Africa may be 6°C warmer than global warming (Tyson et al., 1990; Joubert, 1994; Joubert and Hewitson, 1997; Engelbrecht et al., 2015). Based on GCM simulations, Tyson et al. (1990) projected that, if Global CO_2 doubled, Southern African summer and winter temperatures may increase by up to 4°C by 2020–2040. However, there were some disagreements between GCMs on the magnitude of the increase; while the increase is about 4°C in some simulations it is about only 2°C in others. Joubert (1994) projected a warming of 4° – 6°C over the South African region. In a more recent study, Engelbrecht et al. (2015) projected an increase of 4 – 6°C over the subtropics and 3 – 5°C over the tropics by the end of the century relative to current climate under the Special Report on Emission Scenarios' A2 (low mitigation) scenario.

Several studies have projected that global warming will cause changes in precipitation over Southern Africa, though the certainty of the projection is lower than that of temperature (Joubert, 1994; Engelbrecht et al., 2009). Joubert (1994), for example, predicted wetter conditions in tropical Africa, as well as wetter summers in the summer rainfall region and dry conditions in the winter rainfall region. Climate change, according to Christensen et al. (2007); IPCC (2007); Hulme (1992); Mazvimavi (2010), will reduce rainfall in Southern Africa. Hulme (1992) predicted a 5–10% decrease in rainfall, while Mazvimavi (2010) predicted a 3–23% decrease in rainfall due to climate change in Southern Africa. There appears to be no agreement on the magnitude of the anticipated rainfall decrease. This could be due to the various global climate models used. However, studies such as Schulze et al. (2010) and Tadross et al. (2011) predicted an increase in rainfall over South Africa's north eastern regions under various climate change scenarios. Changes in circulation over the South African region are being used to forecast the effects of global warming on precipitation changes (Joubert, 1994; Engelbrecht et al., 2009). Frontal rain bands would be displaced to the south in the austral winter of the future climate (2070–2100), according to Engelbrecht et al. (2009), as a result of the subtropical high pressure belt intensifying to the south of the subcontinent. Mid- and upper-level highs would become more prominent over the eastern and central parts of Southern Africa in the spring and autumn. Because of the increased subsidence associated with these systems, rainfall totals are generally lower across much of the southern subcontinent. The thesis would look into how future precipitation patterns over the Drakensberg could be influenced.

Extreme weather events in Southern Africa are expected to change as a result of climate change. Climate change studies have predicted that Southern Africa will experience below-normal rainfall and frequent droughts in the future (Hulme et al., 2001; Arnell et al., 2003; Schulze, 2011). Climate change, according to Christensen et al. (2007), will result in longer periods between rainfall events and more extreme events. Abiodun et al. (2020) projected fewer rain days but more intense rainfall events over Southern Africa in the future, based on statistical and dynamical downscaling datasets at GWLs, and

indicated that the magnitude of these changes increases with GWLs. Both statistical and dynamical downscaling datasets projected a decrease in the intensity and frequency of extreme rainfall events south of $20^{\circ}S$ and an increase south of $20^{\circ}S$ in the future. While dynamical downscaling suggested that the rainfall shortage from lesser rain events could surpass the rainfall excess from more severe rain events, statistical downscaling suggested the reverse. However, none of the earlier studies specifically addressed the Drakensberg; instead, they all concentrated on Southern Africa as a whole or on a particular nation. The current study would give policymakers much-needed information about how climate change affects the amount and type of rain that falls over the Drakensberg.

2.6 Scaling of extreme precipitation versus temperature changes

Climate change studies in various parts of the world (e.g., Ivancic and Shaw, 2016; Drobinski et al., 2018; Lenderink et al., 2017) have investigated the scaling of extreme precipitation with temperature as prescribed by the Clausius-Clapeyron (CC) equation. The Clausius-Clapeyron (CC) equation governs the relationship between the atmosphere's water-holding capacity and atmospheric temperature (Singleton and Toumi, 2013). According to this equation, for every $1K$ increase in temperature, the moisture-holding capacity of the atmosphere increases by about 7% (Trenberth et al., 2003). Previous research, such as Ivancic and Shaw (2016), found that temperature is the primary factor controlling peak rainfall intensities, among other things. The saturation water vapour pressure determines the maximum amount of water vapour in the air, which is determined by temperature. The Clausius-Clapeyron (CC) equation defines the relationship between saturation water vapour pressure and temperature. The CC relationship assumes that during the most extreme precipitation events, if all other factors affecting precipitation (including relative humidity) remain constant, precipitation will be proportional to the amount of water held in the atmosphere. Temperatures will rise as a result of global warming. When a constant relative humidity is assumed, changes in precipitation intensities should follow suit, and rainfall events should scale with temperature (Trenberth, 2011; O'Gorman, 2015). The assumption of quasi-constant relative humidity as the climate changes, at least over large spatial and temporal scales, is common (Manabe and Wetherald, 1967) and is an emergent property of climate system general circulation models (GCMs) (Held et al., 2000; Allen and Ingram, 2002). However, it has recently been called into question; decreasing surface Relative Humidity (RH) over land has been observed since 2003 (Simmons et al., 2010). Clausius-Clapeyron scaling is the expected scaling from the Clausius-Clapeyron (CC) equation, which is approximately 7% per degree Celsius (Nayak and Takemi, 2020). We refer to super CC scaling when the extreme precipitation versus temperature rates are greater than the Clausius-Clapeyron predicted extreme precipitation versus temperature rate, and sub CC scaling when it is less.

Other studies have found either above or below CC-scaling rates in other parts of the world. Ivancic and Shaw (2016), for example, used station data to analyze extreme precipitation versus temperature rate using an automated method across the contiguous United States. They discovered that the northeastern United States is most likely to experience higher-than-expected extreme precipitation versus temperature rates (super CC scaling), and that super CC scaling is not common throughout the contiguous United States, and that it can be caused by a variety of factors. In a study of German sites, Haerter and Berg (2009) and Berg and Haerter (2011) suggest that the advent of larger than CC rates may be the result of a change in precipitation cause from large-scale, frontal advection at lower temperatures to smaller scale convection at higher temperatures. According to Lenderink and Van Meijgaard (2008) and Lenderink and Van Meijgaard (2010), the increase in extreme precipitation is caused by the acceleration of convection as temperature rises. As the temperature rises, so does the change in saturation specific humidity. When the atmosphere becomes saturated, it releases more heat and accelerates convection, resulting in an increase in rainfall that exceeds the Clausius-Clapeyron equation. Berg et al. (2013)

provide evidence for both convective and transition forcing, favoring the former. In Switzerland, [Molnar et al. \(2015\)](#) also document both convective and transitional forcing, but with a preference for the former. Neither of these assessments, however, relied on any data outside of Germany and Switzerland. Other research on the causes of greater than CC rates are limited to narrow geographic regions (such as [Loriaux et al., 2013](#)). Unanswered problems include whether these effects contribute in other regions, how they vary spatially, and if the balance between transitional and convective forcing is same everywhere. [Panthou et al. \(2014\)](#) address this problem in part by using short duration events as a proxy for convective events and seeing a mixture of convective and transition forces in Eastern Canada but not Western Canada.

Furthermore, [Drobinski et al. \(2018\)](#) investigated the scaling of precipitation extreme with temperature over the Mediterranean region in regional climate simulations from some models. Despite the difference in the simulated precipitation values across the models, the authors found a consistent and robust scaling between the precipitation extreme and temperature among models. Across the Mediterranean, the temperature-precipitation extremes relationship has a hook shape, with a slope following Clausius-Clapeyron (CC)-scaling at low temperatures and a negative slope at high temperatures. The temperature at which the abrupt change occurs in the curve of the temperature-precipitation extreme relationship ranges from around 20°C in the western Mediterranean to around 10°C in Greece. However, this slope is consistently negative in the arid regions of the Mediterranean. The temperature break is projected to shift to higher temperatures under future climate scenario due global warming.

Hence, since rainfall intensity is expected to increase under climate change due to global warming, it would be interesting to compare the increase rate to a Clausius-Clapeyron scaling and see how the regional changes compare to these theoretical values. However, such analysis about extreme precipitation evolution with temperature changes is lacking for the Drakensberg and it is not known if higher-percentile precipitation intensities mostly increase with temperature over the Drakensberg in future climate. That is, do we expect sub or super CC-scaling and what could be accounting for this. This thesis uses data from the CORDEX and NEX-GDDP to investigate CC-Scaling over the Drakensberg at specific Global Warming Levels.

CHAPTER 3

Methodology

This chapter describes the thesis methodology. It starts by describing the study area. It introduces the datasets and provides their sources, then explains the methods used in the analysis of the dataset. Given that the methodology used in the thesis varies to an extent across the chapters, the present chapter provides a broad overview of the datasets and methods that cuts across all the chapters.

3.1 Study area

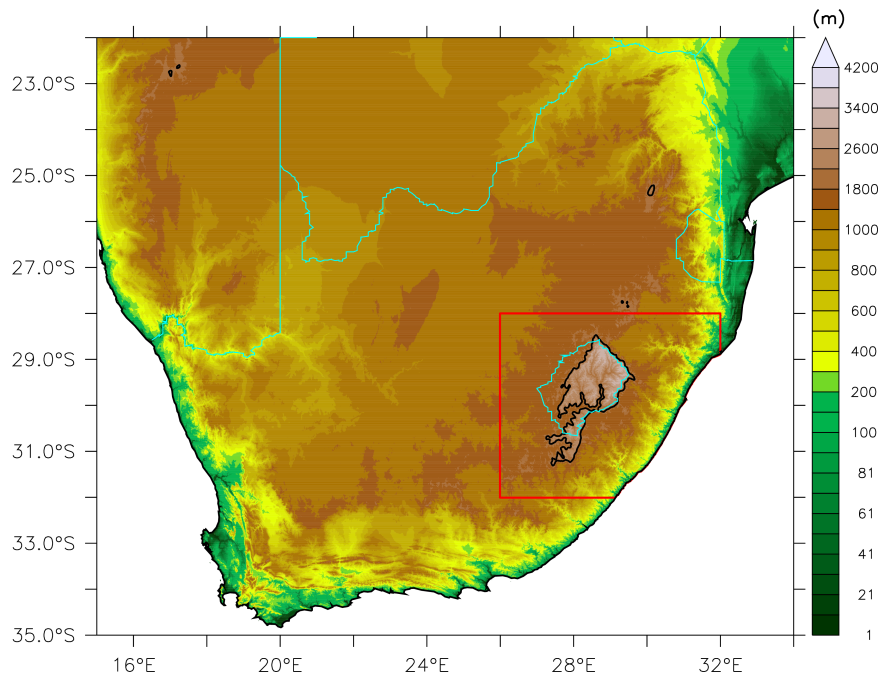


Figure 3.1: Map of Southern Africa showing the topography (shaded) and the study area (called the Drakensberg Mountains; red polygon). The dark contour encloses elevations greater than or equal to 2000m above mean sea level.

The study domain is the Drakensberg Mountains, defined as the area of the eastern escarpment of South Africa extending from $26^{\circ}E$ to $32^{\circ}E$ and Latitudes $28^{\circ}S$ to $32^{\circ}S$ (see Figure 3.1). The area cuts across three South African provinces (KwaZulu–Natal, the Eastern Cape and the Free State) and Lesotho. The Drakensberg is a trans-frontier mountain that straddles the border between South Africa and Lesotho. It receives its highest rainfall in summer and the lowest in winter. Thunderstorms and orographically induced storms are major sources of rainfall over the Drakensberg (Tyson et al., 1976). Cold fronts that move across Southern Africa from a westerly/north-west to east/south-east direction

also bring widespread rainfall and occasionally snow over the Drakensberg (Tyson et al., 1976). However, the inter-annual variation of summer rainfall over the Drakensberg is mostly influenced by the El Niño Southern Oscillation (Nel, 2008).

3.2 Dataset

The thesis analysed three types of datasets, namely: observation, reanalysis, and model simulation datasets. Not all the types of datasets were utilised in all the results and discussion chapters (Chapters 4 - 6). The usage of a dataset in a study (reported in a chapter) depends on the purpose of the study and the availability of the dataset during the study. The atmospheric variables used in each dataset are listed in Table 3.1.

3.2.1 Observation datasets.

The observation data were obtained from eight gridded satellite rainfall datasets. The information of the datasets is summarized in Table 3.2. The observation datasets were used to study the characteristics of rainfall over the Drakensberg and to evaluate the rainfall results from the reanalysis and climate models. While some of the observations were used in all the results chapters (Chapters 4 - 6), some of them were used in only one or two chapters.

To evaluate how well the satellite rainfall datasets capture the observed rainfall over the Drakensberg, the satellite rainfall datasets (AgCFSR, AgMERRA, ARC2, CHIRPS, PERSIANN, TAMSAT, WFDEI-CRU, WFDEI-GPCC) are compared with station observation managed by the South African Weather Services over the Drakensberg. The location of the stations are depicted on Figure 3.2.

Figure 3.3 shows the Taylor diagrams (Taylor, 2001) that were used to compare the satellite rainfall datasets (AgCFSR, AgMERRA, ARC2, CHIRPS, PERSIANN, TAMSAT, WFDEI-CRU, WFDEI-GPCC). The diagrams (Figure 3.3) show that during the period between 1998 – 2007, the Satellite observation datasets (AgCFSR, AgMERRA, ARC2, CHIRPS, PERSIANN, TAMSAT, WFDEI-CRU, WFDEI-GPCC) generally capture to some extent the precipitation intensity recorded at weather observation stations around the Drakensberg. There exist a weak positive correlation between the rainfall recorded at the stations and the satellite measurements. This weak correlation between the insitu rainfall recorded and satellite observation may be due to the interpolation used in obtaining the gridded datasets (Abiodun et al., 2016). It may also be due to cloud coverage, evaporation of rain droplets before they reach the surface and the direction of rainfall and wind at the surface. There are also very weak negative correlations observed at some stations. Figure 3.3 also shows that precipitation at most of the stations is within 0.3 to 2.8 standard deviation (normalized) of the satellite observation. Most of the observation stations capture well the precipitation recorded at low lying altitudes. For example, for all the satellite observations datasets, the largest normalized standard deviations occur at the high-lying station VAN REENEN (located at $28.37^{\circ}S, 29.38^{\circ}E$ and altitude $1680m$). However, in this thesis, satellite rainfall datasets are used for most of the analysis instead of station data, because most of the insitu stations are located below an altitude of $1762m.a.s.l$ whereas the highest peak of the Drakensberg are located at an altitude of $3000m.a.s.l$. Nel and Sumner (2005) was the first study to measure rainfall on the KwaZulu-Natal Drakensberg escarpment at altitude above $2800m.a.s.l$ from two locations. This means that using the station data alone may limit our investigation to foothills of the Drakensberg, hence satellite observation which capture the ground precipitation to some extent may be crucial for evaluating model precipitation at higher altitudes. In addition, it is more appropriate to validate the gridded simulation data with gridded observation data than with station observation data (Abiodun et al., 2016) and

Table 3.1: Atmospheric variables that were analysed from each dataset used in the thesis.

Dataset	Variables analysed
Satellite rainfall datasets (AgCFSR, AgMERRA, ARC2, CHIRPS, PERSIANN, TAM- SAT, WFDEI-CRU, WFDEI- GPCC)	precipitation
CFSR reanalysis	precipitation, wind (u,v,w), geopotential height, mean sea level pressure, specific humidity, Convective Available Potential Energy (CAPE)
CORDEX	precipitation, maximum daily temperature, minimum daily temperature
NEX	precipitation, maximum daily temperature, minimum daily temperature
WRF model	precipitation, wind (u,v,w), geopotential height, mean sea level pressure, atmospheric pressure, specific humidity, potential temperature, CAPE
MPAS model	precipitation, wind (u,v,w), geopotential height, mean sea level pressure, atmospheric pressure, specific humidity, potential temperature, CAPE
South African Weather Services station data	precipitation

previous studies ([Abiodun et al., 2016](#); [Williams et al., 2010](#)) have noted that satellite dataset provides a good alternative to ground-based dataset.

3.2.2 Reanalysis data.

The reanalysis data were obtained from the National Centre for Environmental Prediction (NCEP) Climate Forecast System Reanalysis (CFSR, [Saha et al., 2010, 2011](#)). The dataset has a resolution of $0.5^\circ \times 0.5^\circ$ (lat \times lon). The climate variables used in the CFSR dataset include rainfall, geopotential height, wind (zonal, meridional components), and mean sea level pressure.

As rainfall datasets (observation and reanalysis) have different native resolutions, they were regridded

Table 3.2: Information about 8 observation datasets used in the study. The period of the data analysed in each dataset is indicated.

Dataset	Full name	Type	Resolution	Period	Reference
AgCFSR	Climate forcing datasets for agricultural modeling	Reanalysis-based multiple-source.	0.25°X 0.25°	1981–2010	Ruane et al. (2015)
AgMERRA	Climate forcing datasets for agricultural modelling.	Reanalysis-based multiple-source	0.25°X 0.25°	1981–2010	Ruane et al. (2015)
ARC2	African Rainfall Climatology version 2.0. daily estimates from the Famine Early Warning System (FEWS) from the Climate Prediction Centre (CPC).	Satellite and ground-based data	0.1°X 0.1°	1983–2016	Novella and Thiaw (2013)
CHIRPS	Climate Hazard Group Infrared Precipitation with Stations	Satellite and ground-based data	0.05°X 0.05°	1987–2016	Funk et al. (2014)
PERSIANN	Precipitation Estimation from Remotely Sensed Information using Artificial Neural Network	Satellite based data	0.25°X 0.25°	1987–2016	Sorooshian et al. (2000)
TAMSAT	Tropical Applications of Meteorology using Satellite data and ground-based observations.	Satellite and ground-based data	4 X 4 km	1983–2012	Sorooshian et al. (2000)
WFDEI-CRU	Water and Global Change Forcing Data methodology applied to ERA-Interim(WFDEI) [Climate Research Unit (CRU)]	Reanalysis-based multiple-source	0.5°X 0.5°	1987–2016	Weedon et al. (2014)
WFDEI-GPCC	Water and Global Change Forcing Data methodology applied to ERA-Interim [Global Precipitation Climatology Centre (GPCC)]	Reanalysis-based multiple-source		1987–2016	Weedon et al. (2014)

from their native resolution to a resolution of 0.25° by 0.25° to obtain an identical grid before the analysis.

3.2.3 Model simulation data.

The model data consist of simulation datasets from two international experiments and various local experiments performed as part of the thesis. The two international simulation datasets are from the Coordinated Regional Climate Downscaling Experiment (hereafter, CORDEX) and the National Aero-

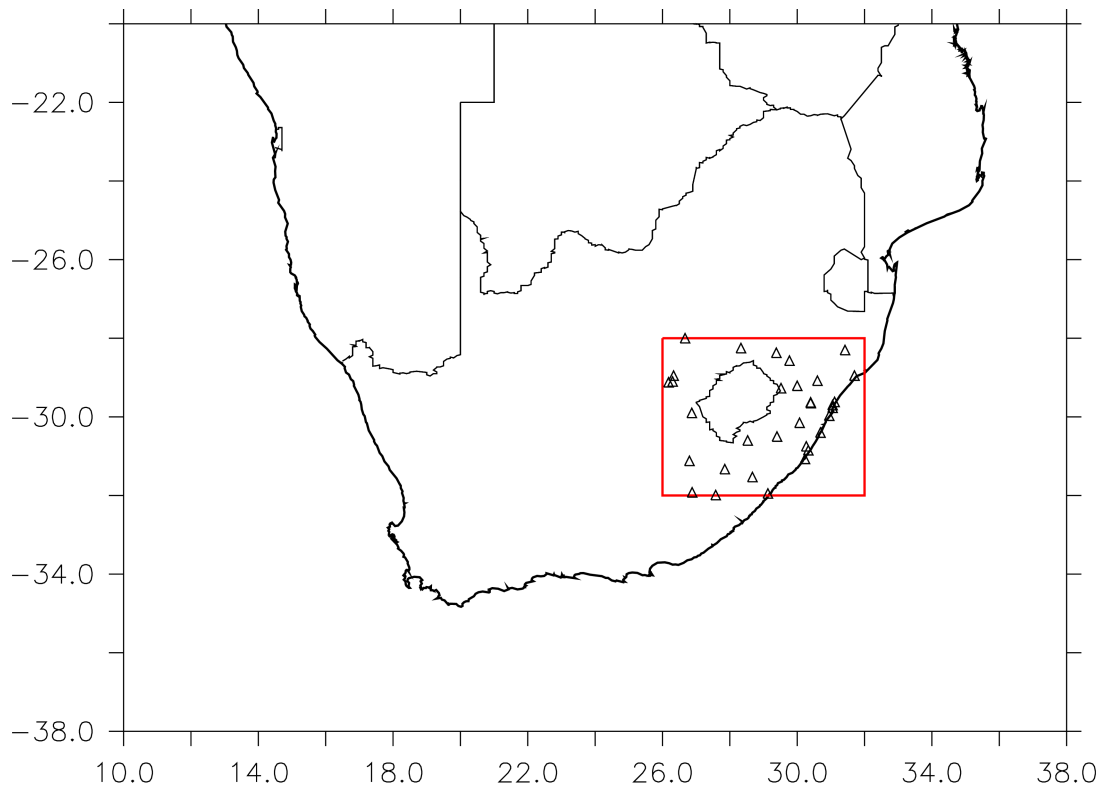


Figure 3.2: Location of the weather observation stations (black triangles) used for the validation of satellite rainfall datasets (AgCFSR, AgMERRA, ARC2, CHIRPS, PERSIANN, TAMSAT, WFDEI-CRU, WFDEI-GPCC) over the study domain (red rectangle); the stations are managed by the South African Weather Service (SAW).

navitics and Space Administration (NASA) Earth Exchange Global Daily Downscaled Projections (NEX-GDDP; hereafter, NEX). The local simulation datasets were generated with the Weather Research and Forecasting (WRF) model and WRF and the Model for Prediction Across Scales (MPAS).

CORDEX dataset

The World Climate Research Program (WCRP) developed the CORDEX framework to provide high-resolution regional climate data over regions worldwide to provide information for impact/adaptation work and the IPCC Fifth Assessment Report (AR5), as well as to promote greater interaction and communication between global climate modellers, the downscaling community, and end-users to better support impact/adaptation activities (Giorgi et al., 2009). The CORDEX framework categorizes the world into domains (Central America, Europe, Africa, South Asia, East Asia, Central Asia, Austral Asia, Antarctica, Arctic, Mediterranean, Middle East North Africa, and South-east Asia; CORDEX, 2022). In this study, the CORDEX dataset over the African domain was used. The dataset has a resolution of 50km (Nikulin et al., 2018) and spanned the period 1950 – 2100.

Several studies have established the credibility of the CORDEX dataset over Africa and analysed it for future climate projection (Abiodun et al., 2020; Nikulin et al., 2018; Mba et al., 2018; Klutse et al., 2016; Laprise et al., 2013; Diasso and Abiodun, 2017; Dosio and Panitz, 2016; Akinsanola et al., 2015). In the thesis, the CORDEX dataset is further evaluated and applied for climate change projection over the Drakensberg. Specifically, the version of the CORDEX dataset used was obtained by using RCM

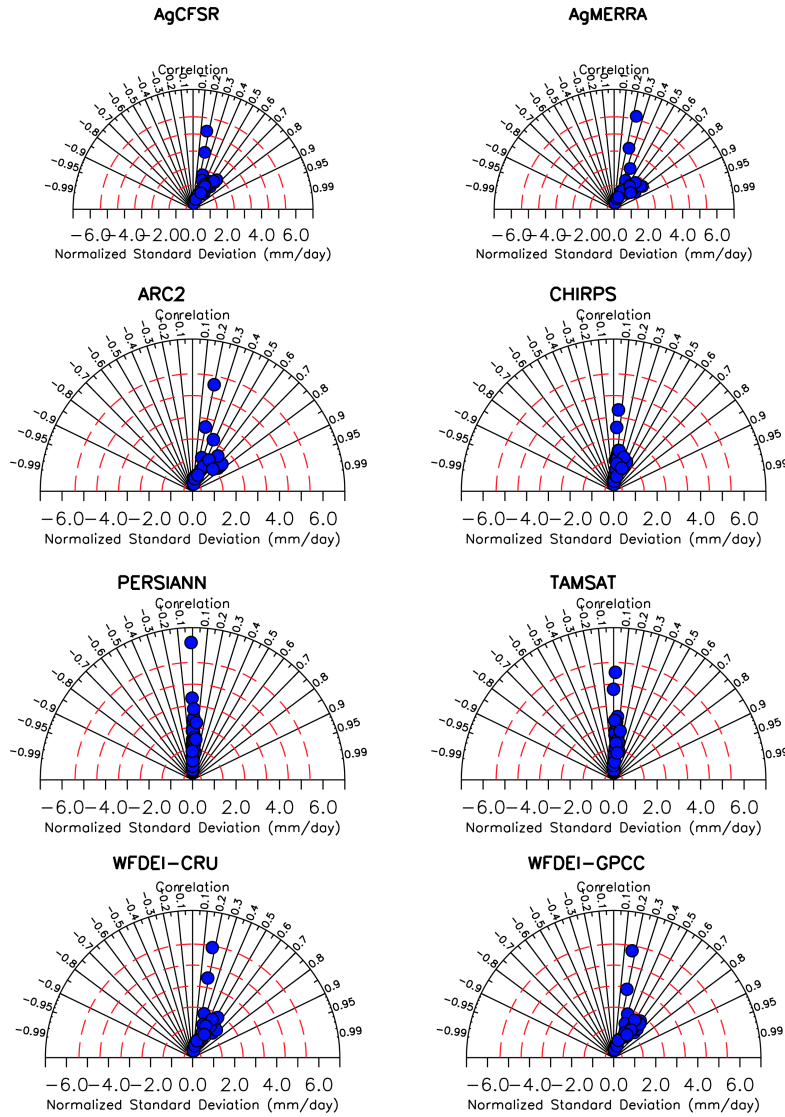


Figure 3.3: The Taylor diagrams (i.e. correlation and normalised standard deviation) used for the comparison of satellite rainfall datasets (AgCFSR, AgMERRA, ARC2, CHIRPS, PERSIANN, TAMSAT, WFDEI-CRU, WFDEI-GPCC) with South African Weather Service (SAW) station observation over the Drakensberg (stations depicted in Figure 3.2). In the panels, the blue circles represent the observation stations (normalised by the corresponding satellite rainfall dataset).

to downscale the simulations of the Coupled Model Intercomparison Project (CMIP5: [Taylor et al., 2012](#)) experiment over the Africa domain. The matrix RCM-GCM for the experiment consists of 25 simulations assuming RCP8.5 and RCP4.5 ([Nikulin et al., 2018](#)). However, only 20 simulations assuming the RCP8.5 scenario were used. The information on the 20 simulations is provided in Chapter 6.

NEX dataset

The NEX dataset was generated to help scientists study the effects of climate change on small- to medium-sized areas, as well as to help the public learn more about possible future climate patterns and their effects on cities, communities, and watersheds ([Thrasher et al., 2013](#)). Its objective is to generate a

series of bias-corrected, high-resolution, global climate change projections that can be utilized to study the impacts of climate change on processes that are sensitive to fine-scale climate gradients and to examine the influence of terrain on local climate. The NEX-GDDP dataset contains downscaled climate scenarios for the entire world derived from General Circulation Model (GCM) runs conducted during the Fifth Phase of the Coupled Model Intercomparison Project (CMIP5) and across two of the four greenhouse gas emissions scenarios known as Representative Concentration Pathways (RCPs) (Meinshausen et al., 2011). The downscaling was carried out using the Bias-Correction Spatial Disaggregation (BCSD) statistical downscaling algorithm (Wood et al., 2002, 2004). The BCSD algorithm utilizes the spatial detail provided by observationally derived datasets to interpolate GCM outputs to higher resolution grids. This makes the NEX data suitable for studying climate over complex terrain regions like the Drakensberg. However, aside from the increased spatial resolution and bias correction, this downscaling adds no information to the original CMIP5 scenarios and maintains the frequency of periods of abnormally high and low temperature or precipitation (i.e., extreme events) within each CMIP5 scenario.

The NEX dataset contains 42 climate projections from 21 CMIP5 GCMs and two RCP scenarios (RCP 4.5 and RCP 8.5) from 2006 to 2100, as well as the historical experiment for each model from 1950 to 2005. Each of these climate projections is downscaled to $0.25^\circ \times 0.25^\circ$ in spatial resolution (approximately $25\text{km} \times 25\text{km}$). The spatial coverage ranges from 180°W to 180°E , and from 90°S to 90°N . Hence, NEX has a spatial resolution of 0.25° , and its temporal coverage spans the period 1950–2100. This dataset only includes the variables daily minimum and maximum near-surface air temperatures, as well as precipitation. NEX data has been used in several studies (Abiodun et al., 2020; Chen et al., 2017; Yu et al., 2018; Bao and Wen, 2017). The NEX dataset is used in this study to further evaluate and apply over the Drakensberg. For this study, only RCP8.5 is examined. Table 3.2 shows the list of NEX models used in this study. individual CMIP5 scenario.

WRF model

The WRF model (Skamarock et al., 2005; Skamarock and Klemp, 2008; Powers et al., 2017) is a cutting-edge numerical weather forecasting model used for both research and operational forecasting. It is the most widely used atmospheric model in the world (Powers et al., 2017). It was first released in December 2000, and its development is being led by the National Center for Atmospheric Research (NCAR) in collaboration with the National Oceanic and Atmospheric Administration (NOAA) represented by NCEP, now known as the NOAA Earth System Research Laboratory (ESRL), and other US government agencies. The WRF model's initial release included two dynamical cores: the Advanced Research WRF model (ARW) and the Non-Hydrostatic Mesoscale Model (NMM). WRF can be run on a lat-lon grid as a Global model.

Several studies (e.g., Crétat et al., 2012; Ratnam et al., 2012; Vigaud et al., 2012) have used the WRF model to simulate weather and climate over Southern Africa. WRF is used in this study to investigate precipitation characteristics over the Drakensberg during weak synoptic days (Chapter 4) and widespread extreme rainfall events (Chapter 5). Because the WRF configuration for these studies differs, the model's WRF configuration is described in each chapter.

The MPAS

The MPAS (Skamarock et al., 2012) is a state-of-the-art global, fully compressible, non-hydrostatic variable resolution model. It uses finite volume numerics discretized on a centroidal Voronoi mesh. It is a family of Earth-System component models, namely, MPAS Atmosphere model, MPAS Ocean model, and MPAS Ice model. These are all stand-alone models and at the time of this writing, there exists

no coupler in MPAS. Its development is led by the Climate Modelling Group at Los Alamos National Laboratory (MPAS Ocean) and the National Center for Atmospheric Research (MPAS Atmosphere).

MPAS uses unstructured meshes to provide variable resolution and also addresses the pole problem encountered in models using traditional lat-lon grids (Ha et al., 2017). It can increase horizontal resolution locally by stretching and cell division, allowing for a smooth resolution transition to the desired high resolution. This smooth transition is accomplished by employing Voronoi tessellations to generate irregular multigonal grid cells around grid points, resulting in a global irregular grid (Skamarock et al., 2012). It makes use of scale-aware parametrizations. Heinzeller et al. (2016); Park et al. (2014); Maoyi et al. (2018); Maoyi and Abiodun (2022) are some studies that have used the MPAS model. Maoyi and Abiodun (2022) used MPAS to study the characteristics of the Botswana high and found that MPAS reproduces all the important features in Southern African climate, including vertical motion, 500 hPa geopotential height, rainfall and temperature. It also replicates the spatial and temporal variation of the Botswana High and captures its influence on droughts and deep convection over the subcontinent. In the present study, MPAS is evaluated and applied to investigate the characteristics of widespread extreme rainfall events over the Drakensberg (in Chapter 5). The chapter describes the MPAS model set used in the study.

3.3 Methods

Various methods were employed to do various analyses in the study. While some of the methods were used in all the result chapters of the thesis (Chapters 4 – 6), some methods were only employed in a chapter. However, the description of all the methods or definitions is provided in this section.

3.3.1 Identification of weak synoptic days and wet weak synoptic days..

Weak synoptic days over the Drakensberg are identified using the characteristics of geostrophic wind speed at 850 hPa. The geostrophic wind is a theoretical wind which results when the pressure gradient force is equal to the Coriolis force. Mathematically, it is defined as:

$$u_g = -\frac{1}{f\rho} \frac{\partial P}{\partial y} \quad (3.3.1)$$

$$v_g = \frac{1}{f\rho} \frac{\partial P}{\partial x} \quad (3.3.2)$$

$$u_g = -\frac{g}{f} \frac{\partial Z}{\partial y} \quad (3.3.3)$$

$$v_g = \frac{g}{f} \frac{\partial Z}{\partial x} \quad (3.3.4)$$

$$G = \sqrt{u_g^2 + v_g^2} \quad (3.3.5)$$

Where P is atmospheric pressure, Z is geopotential height, f is Coriolis parameter, ρ is air density, g is acceleration due to gravity, G is geostrophic wind, u_g is geostrophic wind zonal component and v_g is geostrophic wind meridional component. The equations show that the geostrophic wind is a function of pressure gradients which determines atmospheric flow(circulation) intensity, hence, the geostrophic wind can be used as a proxy for determining whether we are under strong or weak synoptic conditions. However, in the thesis, we used equation (3.3.3) and (3.3.4) for calculating zonal and meridional component of the geostrophic wind then used equation (3.3.5) to obtain the magnitude to the geostrophic wind.

Hence, a weak synoptic day (WSD) over the Drakensberg Mountains area (Figure 3.1) is defined as a day in which the average geostrophic wind speed is less than or equal to the 10th percentile of the daily geostrophic wind speeds over the mountain during the study period (1983 – 2012). If the daily rainfall for the day is equal to or greater than 1mm, the day is regarded as the wet WSD. The WSDs were obtained using the geopotential height data from the CFSR while the wet WSDs were obtained using rainfall data from the CFSR and two observation datasets that were available during the study (i.e., ARC2 and CHIRPS). The results of the analysis are presented and discussed in Chapter 4.

3.3.2 Definitions of rainfall and extreme rainfall indices.

Following Abiodun et al. (2020) and the Expert Team (ET) on Climate Change Detection and Indices (ETCCDI, 2022), the thesis used different indices to characterise rainfall and extreme rainfall over the Drakensberg. The definitions of the indices are provided in Table 3.3. The indices were employed to quantify the frequency, duration, and intensity of extreme events over each grid point in the Drakensberg domain. In Chapter 5, four of the indices (i.e., RTOT, SDII, RW95p, and R95pTOT) were calculated using six observations (ARC2, CHIRPS, PERSIAN, WFDE-CRU, WDDEI-GPCC), the reanalysis (CFSR), and the two locally generated simulation (i.e., WRF and MPAS) datasets to study the characteristics of extreme rainfall over the Drakensberg. In Chapter 6, all the indices were calculated using all the observation datasets (Table 3.2) and the two international simulation datasets (i.e., CORDEX and NEX) to study the potential impacts of climate change over the Drakensberg. The results of the analyses are reported in the respective chapters.

The thesis also characterised widespread extreme rainfall events (WERE) over the Drakensberg by adopting the WERE identification procedure of Omar and Abiodun (2017). The procedure identifies WERE over the Drakenberg in two steps. First, It identifies all the grid points that experience extreme rainfall in a day (NB: a grid point experiences an extreme rainfall event in a day if the rainfall at the grid point for the day equals or is greater than the 95th percentile of daily rainfall at the grid point). Second, it declares a day as WERE day over the Drakensberg if the number of grid points experiencing extreme events for the day exceeds a threshold (i.e. 40%). The sensitivity of the WERE identification to the threshold was studied in Chapter 5.

3.4 Quantifying phase synchronization between observed and simulated variables

The phase synchronisation analysis was used to quantify phase synchronization between the observed and simulated time series of the climate variables. The phase synchronization (η) is calculated as:

$$\eta = \left(\frac{n'}{n} \right) \times 100 \quad (3.4.1)$$

Where n' is the number years when simulation data is in phase with observation data and represents the total number of years used for the study ($n = 30$). A value of 0% means no synchronization between the simulated and observed datasets while a value of 100% means a perfect synchronisation between a given dataset and CHIRPS observation. The approach has been used by several studies (i.e., Maoyi et al., 2018; Araujo et al., 2016; Tozuka et al., 2014).

Table 3.3: Definition of extreme rainfall indices used in this study.

Index type	Rainfall Index	Definition
Mean intensity indices	RTOT	Annual total precipitation in wet days (Klein Tank AMG, 2009)
	WDays	Wet days. Annual count of days with daily precipitation greater or equal to 1 mm (Klein Tank AMG, 2009)
	SDII	SDII is the intensity of normal precipitation, calculated as RTOT divided by WDays (Klein Tank AMG, 2009).
	Rx5Days	Maximum consecutive 5-day precipitation
Strong intensity indices	R97.5p	All-day percentile. The R97.5 th percentile precipitation on all days (Schär et al., 2016). Any daily rainfall above this threshold (R97.5p) is considered an extreme event.
	R97.5pTOT	Annual total precipitation when daily rainfall is greater than or equal to RA97.5p (Schär et al., 2016).
	RW95p	Wet-day percentile. The 95th percentile of precipitation on wet days
	R95pTOT	Annual total precipitation when daily rainfall is greater than or equal to RW95p
Occurrence indices	R20mm	Annual count of days when daily precipitation \geq 20mm (Klein Tank AMG, 2009).
	R97.5pFREQ	Annual count of days when daily rainfall is greater or equal to RA97.5p of the present-day climate (Schär et al., 2016).
	WEREFreq	Annual count of days when daily rainfall is greater or equal to RA97.5p of the present-day climate over at least 40% area of DMR (Abiodun et al., 2017).
Duration indices	CWD	Maximum length of wet spell. Maximum number of consecutive days with daily precipitation greater than 1 mm (Klein Tank AMG, 2009)
	CDD	Maximum length of dry spell. Maximum number of consecutive days with daily precipitation less than 1 mm

3.5 Classification of rainfall patterns on WERE days.

We employed the Self-Organizing Map (SOM) analysis to classify rainfall patterns on WERE days. SOMs are a form of artificial neural network which are used for pattern recognition Kohonen (1990). It has been used in several synoptic analysis (Hewitson and Crane, 2002; Lennard and Hegerl, 2015; Odoulami et al., 2021). For a comprehensive review of the use of SOMs in synoptic climatology research, interested readers can take a look at Sheridan and Lee (2011).

Two SOMs analysis were performed in this study. The first SOM analysis consisted in classifying daily

mean sea level pressure from CFSR reanalysis, WRF, and MPAS simulations for the period 1st January 1987 to 31st December 2016 into 63 groups (9×7 map). This was done to identify the synoptic circulation features associated with WERE over the Drakensberg. After classifying the mslp into 63 groups, the WERE event days identified using the 40% threshold earlier indicated were mapped to the corresponding SOM nodes in which the associated mean sea level pressure was assigned. The second SOM analysis consisted in classifying grid points which experienced extreme rainfall during WERE events (period 1st January 1987 to 31st December 2016) over the Drakensberg into 12 groups (4×3 SOM nodes) to identify the patterns of strong rainfall areas during WERE events over the Drakensberg.

3.5.1 Classifying or grouping the spatial patterns of climate variables.

The thesis employed the Self-Organizing Maps (SOMs) analysis to classify or group climate variables. SOM is a form of artificial neural network used for pattern recognition [Kohonen \(1990\)](#). It takes high dimensional data as input and reduces it to a lower dimensional (typically two-dimension) input space of training samples called maps. SOM can be used for feature extraction, clustering, pattern recognition, dimensionality reduction, visualisation of complex structures that would otherwise be hardly recognizable by humans, supervised data classification, and data interpolation.

SOM works as follows. A map with a user-specified number of nodes is seeded with data set random values or eigenvectors. The number of nodes selected is governed by the user's desired degree of generalization/specialization. Unsupervised learning is used to train the SOM network after it is given a dataset (input vector or case). Each input vector (case) is added to the SOM, and the node with the shortest Euclidean distance from the input vector is identified as the 'winning' node ([Hewitson and Crane, 2002](#)). This node is then given a learning-rate parameter, thereby guiding it in the direction of the new scenario. A distance decay function is utilized to adjust the array neighbors of the winning node as well as the winning node itself. Finally, because of this spatialized pattern of adjustment, the array of nodes 'self-organizes' into a coherent pattern, with more identical nodes closer together and more different nodes further away. Outlier instances are less likely to be merged into an unrepresentative cluster if the four corners of the SOM are considered the most extreme nodes in terms of distance (i.e. more common weather situations). A Sammon map, which displays multidimensional vectors in two-dimensional (2-D) space, may be used to depict the SOM process outcomes, with distances effectively representing the amount of dissimilarity between distinct nodes.

SOM is topologically preserving in the sense that neighbourhoods are preserved (as much as possible) during the mapping process. In general, no matter how the network is trained, there will always be some difference between any given input pattern and the unit to which it is mapped. This difference is referred to as quantization error, and it is used to assess how well map units represent the input patterns. The SOM algorithm's performance is determined by two important parameters: learning rate and learning radius. The learning rate controls how quickly the weights move toward the data points. It must begin quite high for the map to move quickly towards the data distribution. It must be nearly zero in order for the map to stabilize and settle on a final solution. The learning radius determines how many nodes are updated around the winning node. This parameter should be set quite high to ensure that the map's topology is strongly maintained while it aligns itself with the data. It is then gradually reduced, allowing individual nodes to reach a final stable position.

Several studies have applied SOM to climate variable classification (i.e., [Hewitson and Crane, 2002](#); [Tadross et al., 2005](#); [Hope, 2006](#); [Lennard and Hegerl, 2015](#); [Odoulami et al., 2021](#); [Alexander et al., 2010](#); [Steynor et al., 2009](#)), but [Hewitson and Crane \(2002\)](#) was the first study to introduce the concept of self-organizing maps synoptic climatology. In the present study, SOM was applied to perform

a series of classifications. In Chapter 4, it was used to classify the rainfall patterns on the wet WSDs. In Chapter 5, it was used to identify synoptic weather patterns over Southern Africa and to group the rainfall patterns during the WERE days over the Drakensberg. In Chapter 6, it was applied to group the projected changes in climate variables. A more detailed description of how SOM is used in a chapter is provided in the chapter.

CHAPTER 4

Simulating rainfall distribution over the Drakensberg on weak synoptic days

This chapter reports the study of rainfall distribution over the Drakensberg during weak synoptic days (WSDs). The study, which analysed three types of datasets (satellite, reanalysis, and high-resolution climate simulation), compares annual distribution of rainfall over the Drakensberg from reanalysis and satellite datasets, identifies the dominant WSD rainfall patterns, and assess how well the reanalysis and the climate simulation reproduce the rainfall amount and patterns. The observation datasets used in the study are the African Rainfall Climatology version 2 (hereafter, ARC2) and the Climate Hazard Group Infrared Precipitation with Stations (hereafter, CHIRPS). The reanalysis dataset is the Climate Forecast System Reanalysis (hereafter, CFSR) from the National Centre for Environmental Prediction. In the study, CRSR was downscaled over Drakensberg using the Weather Research and Forecasting (WRF) model. A comprehensive description of ARC2, CHIRPS, CFSR and WRF are in Chapter 3.

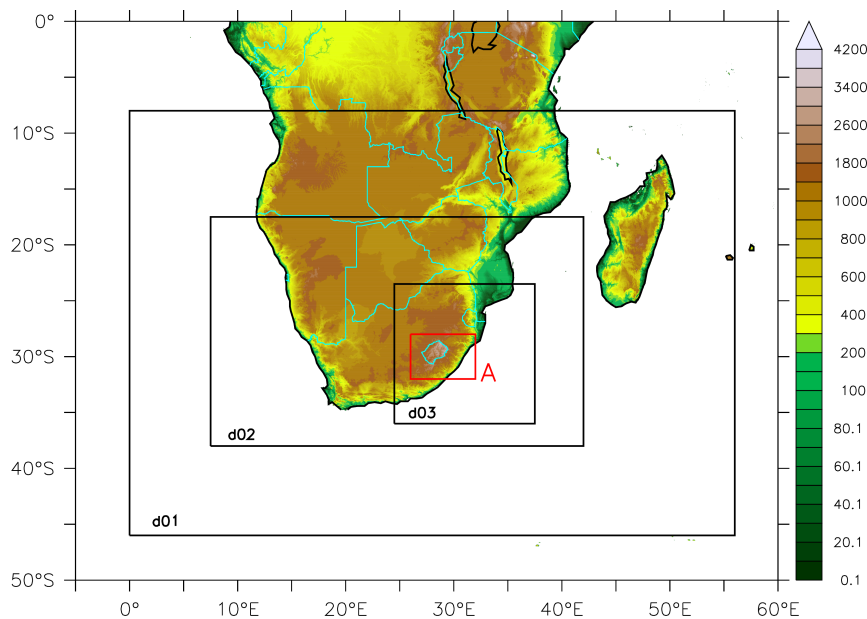


Figure 4.1: Southern African topography (colours; in meters) and WRF model nested domain (d01, d02 and d03). The red box **A** indicates the study area and region used in identifying weak, strong and extremely strong synoptic-scale conditions over the Drakensberg.

The WRF downscaling experiment consists of a one-way three-level nested domain (Figure 4.1). The outermost domain (d01) has the lowest resolution of 18km covering the whole of Southern Africa while the middle domain (d02) has a resolution of 6km spanning the whole of South Africa. The innermost domain (d03) has the highest resolution of 2km covering the Drakensberg Mountain area

and its adjacent. Hence, in the one-way nesting simulations, the WRF simulation over d01 (hereafter, WRF18) downscaled the forcing CFSR reanalysis, while the simulation over d02 (hereafter, WRF06) downscaled WRF18, and that over d03 (hereafter, WRF02) downscales WRF06. Each simulation covered a period of 54 hours (2 day, 6 hours). The first 6 hours of simulation were discarded as spin-up and the last 2-day simulation were analysed in the study. The list of WRF physics parameterization option used in the model simulation is shown in Table 4.1.

Table 4.1: WRF model configuration for simulation of rainfall patterns from SOM classification.

Model Physics Option	Option selected (18km)
Micro-physics scheme	Morrison
Short wave radiation Scheme	Goddard short wave
Long wave radiation Scheme	Rapid Radiative Transfer Model scheme
Surface-layer option	Monin-Obukhov (Janjic) scheme
Land-surface option	Unified Noah land-surface model
Boundary-layer option	Mellor-Yamada-Janjic TKE scheme
Cumulus option	Kain-Fritsch (new Eta) scheme (only in 18km and 6km domains)

4.1 Characteristics of weak synoptic days

Following the WSD identification procedure described in Chapter 3 (Section 3.1), WSDs were identified using the CFSR datasets and wet WSDs were identified for CFSR and observation datasets using the WSD from the CFSR dataset. From the analysis, 1146 days were identified as WSDs. However, while 489 ($\simeq 42\%$) and 402 ($\simeq 35\%$) of the WSDs were identified as wet WSDs in ARC2 and CHIRPS, respectively, only 255 ($\simeq 19\%$) of the WSDs were reported as wet WSDs CFSR. This buttresses the weakness of the reanalysis in reproducing the wet WSD over the mountain. The small discrepancy in wet WSDs of the two satellite datasets (ARC2 and CHIRPS) may be attributed to the differences in the resolution and orbit of the satellites.

Figure 4.2 presents the seasonal mean of WSD over the Drakenberg and the percentage contributions of weak, moderate, and strong synoptic days. The figure shows that a weak synoptic day (WSD) over the Drakensberg can occur in any season. WSD contributes up to 16% of weather conditions over the Drakensberg in JJA and 20% in May–June (MAM) but less than 5% in other seasons (Figure 4.2). A WSD in a season is often characterized by a higher-than-normal mean-sea-level pressure (MSLP) for the season, because it is usually associated with a high-pressure system or the ridging of the South Atlantic/Indian High over the mountain (Figure 4.2 b, f, j & n). Despite the high pressure, some WSDs are wet days, especially when the wind speed is between $5 - 7\text{ms}^{-1}$ (Figure 4.3). This may be because stagnating high pressure systems (i.e., anticyclones) are known to facilitate the development of small-scale circulations (Lennard and Hegerl, 2015). For example, Lennard and Hegerl (2015) showed that

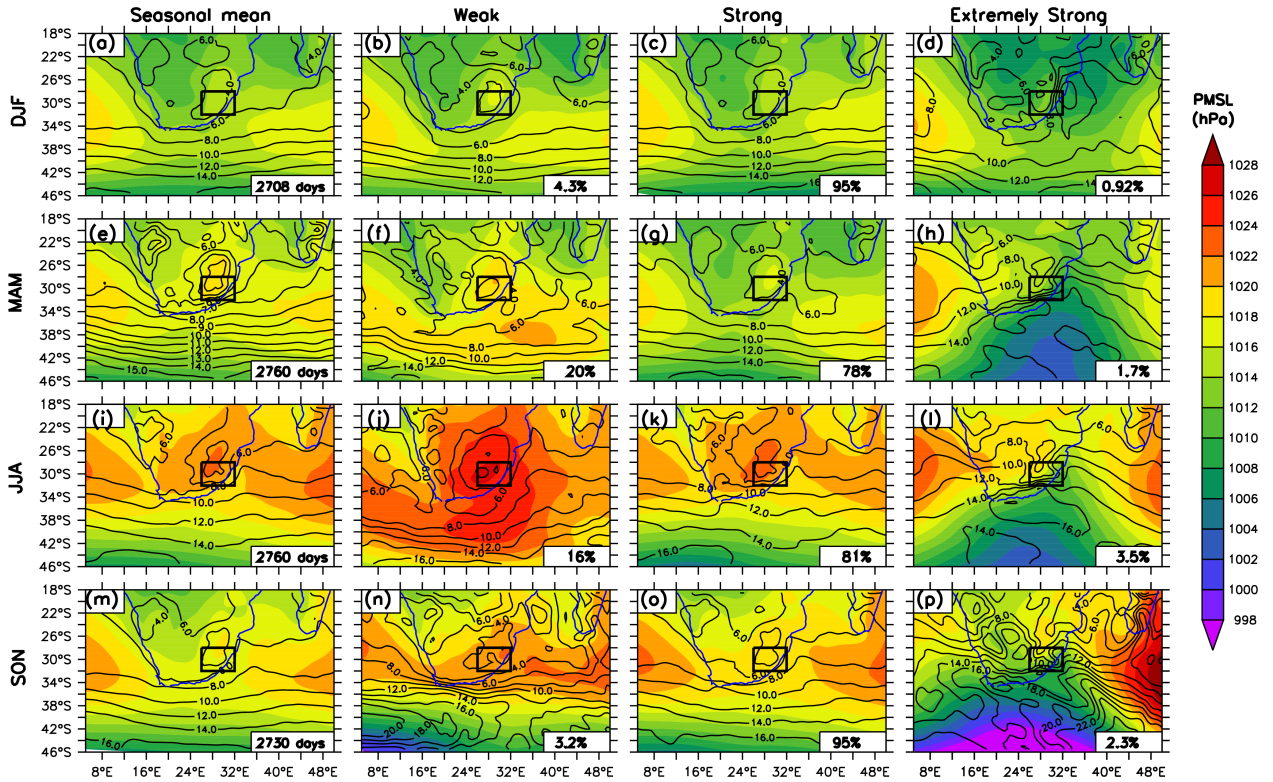


Figure 4.2: Composite of mean sea level pressure during different geostrophic wind (GW) conditions over the Drakensberg (black box) during different seasons (DJF, MAM, JJA, SON) in 1983 - 2012, as depicted by CFSR.

stagnating high pressure systems over the South-Western parts of South Africa facilitate small-scale processes such as mountain winds and land/sea breezes. These local-scale processes could enhance the advection of warm moist air by the north-easterlies from the Indian Ocean to the Drakensberg and trigger the local convection in the mountain's vicinity. However, the coarse horizontal resolution of the CFSR could compromise the representation of these local-scale features and underestimate the associated precipitation.

4.2 Rainfall over Drakensberg on wet weak synoptic days

Figure (4.3 and 4.4) compare the characteristics of wet WSDs in CFSR with the two rainfall observation datasets. Although CFSR agrees with other datasets that wet WSDs contribute more than 5% of the annual rainfall over the Drakensberg and that the majority of wet WSDs occur in MAM, the reanalysis CFSR produces the least number of wet WSDs among the datasets in all seasons (Figure 4.4). Although the correlation between CFSR and observation on the annual variation of WSD frequency is high ($r=0.8$; 95% significance level), the amplitude of the variability is lower in CFSR than in the observation (Figure 4.4) and the trend in the wet WSD frequency is lower in CFSR ($1.3 \text{ days decade}^{-1}$) than in observation (ARC2: $3.3 \text{ days decade}^{-1}$ and CHIRPS: $1.9 \text{ days decade}^{-1}$). All these stresses the shortcomings of CFSR in replicating the characteristics of wet WSD over the mountain. The shortcomings may be attributed to the low resolution of the CFSR model, or the inadequacy of the convection parameterizations schemes used in the model (Dedekind et al., 2016; Novella and Thiaw, 2013; Funk et al., 2014; Nikulin et al., 2012; Sylla et al., 2013; Abiodun et al., 2016; Omar and Abiodun,

2017).

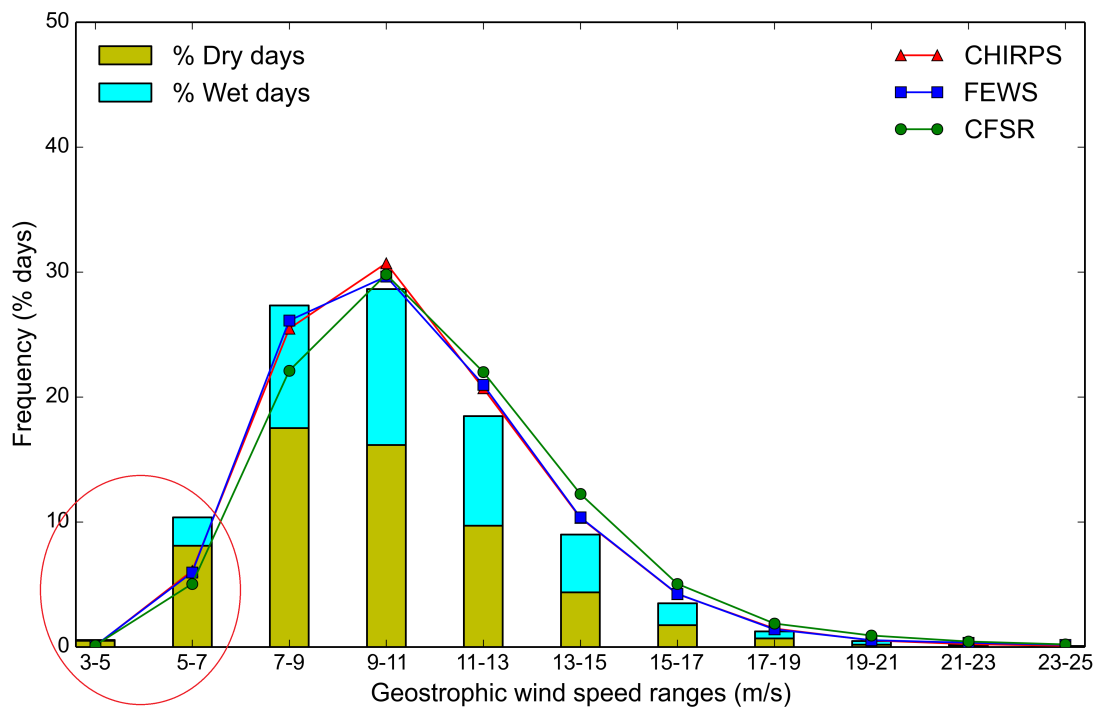


Figure 4.3: Percentage frequency distribution of geostrophic wind speed (GW bars: CFSR) and the percentage rainfall contribution (lines: CHIRPS, FEWS (i.e., ARC2), CFSR) of each GW range to the total rainfall over the Drakensberg in period 1983 - 2012. The range of GW designated as weak synoptic condition is indicated with a red circle. The maximum GW is 32.52 m s^{-1} , but GW greater than 25 m s^{-1} are not shown.

In the spatial distribution of WSD rainfall (Figure 4.4), CFSR shows a better agreement with ARC2 than with CHIRPS. For instance, there is a stronger pattern correlation between CFSR and ARC2 ($r = 0.97$) than between CFSR and CHIRPS (0.27). CFSR also reproduces the west–east rainfall gradient present in the ARC2 data, which is characterized by a drier west (rain shadow) and a wetter (high rainfall) east. In addition, it captures the southwest–northeast rainfall gradient with high rainfall in the northeast of the domain. The west–east gradient is consistent with previous studies (Dedekind et al., 2016; Ndarana et al., 2021; De Coning, 2013) that have reported a west-east rainfall gradient over the whole of South Africa. This is attributed to the increase in topographic elevation when traversing South Africa from west to east. Although previous studies agree on the tight coupling between rainfall and topography over the Drakensberg, there is an ongoing controversy on the precipitation–topography relationship over the Drakensberg (Nel, 2008). This controversy is with respect to the position of the maximum annual rainfall over the Drakensberg. While some researchers suggest that the maximum mean annual rainfall occurs at the mountain’s top, others argue that it occurs along the slope. However, our results suggest that maximum rainfall areas on the Drakensberg on wet WSDs are mostly located on the mountain top, although with some local maximum rainfall along the slopes (Figure 4.4d and Figure 4.4e).

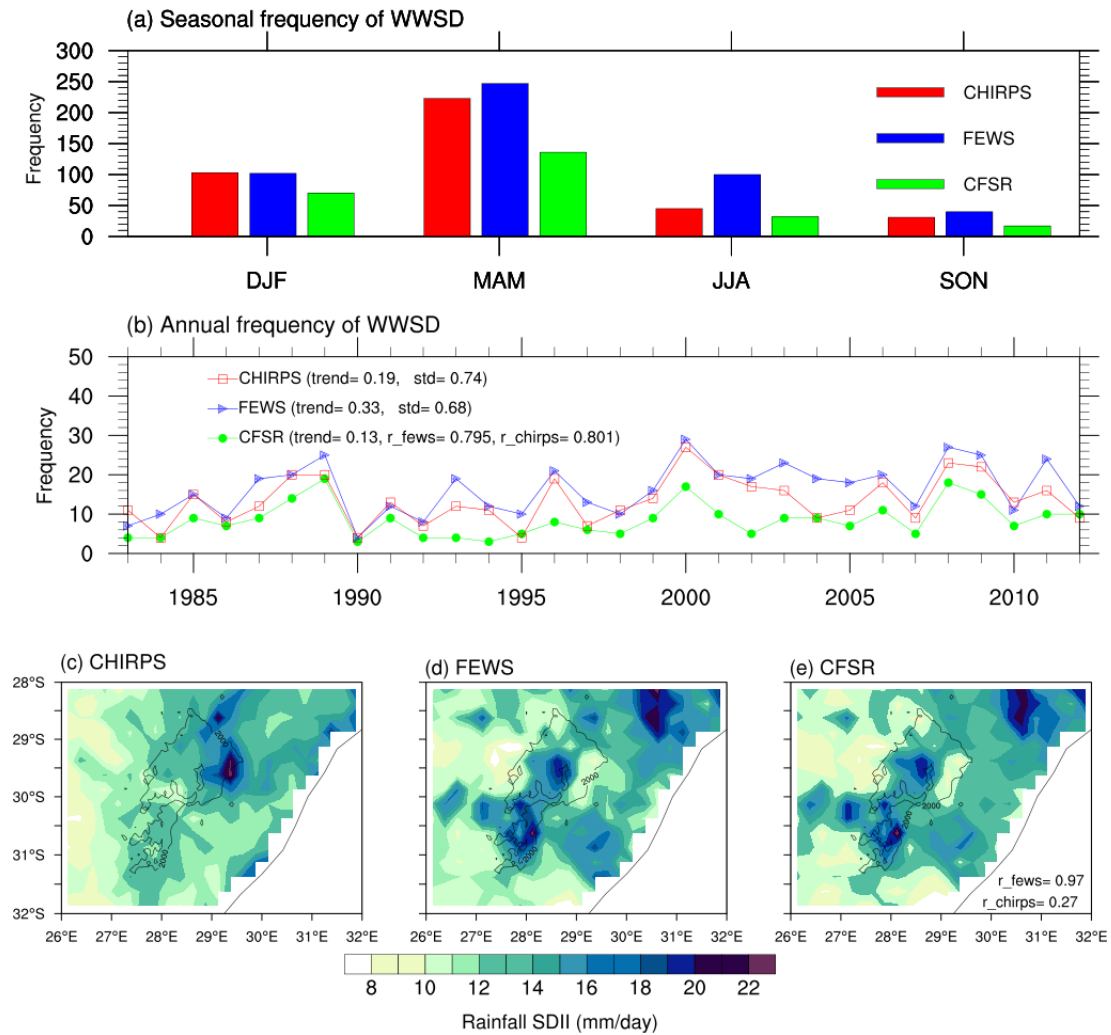


Figure 4.4: The temporal (annual and seasonal) and spatial variations of wet weak synoptic days (WWSD) over the Drakensberg as depicted by observation (CHIRPS and FEWS (i.e. ARC2)) and reanalysis (CFSR) in the period 1983 – 2012. The trend ($days\ year^{-1}$), normalised standard deviation (std), and the correlation between CFSR and each observation (r_{ARC2} and r_{chirps} for ARC2 and CHIRPS, respectively) for annual variability are indicated in panel (a). Panels (c) CHIRPS, (d) ARC2 and (e) CFSR show the pattern of simple precipitation intensity Index of the wet WSD. The correlation between the CFSR and observation patterns (r_{feWS} and r_{chirps}) are indicated in the bottom left of panel (d). The black contour (2000 m height) indicates the Drakensberg location.

4.3 Major patterns of WSD precipitation and the associated dynamics

For a better insight into the dominant spatial patterns of rainfall on WSD, Figure 4.5a presents the SOMs classification of the rainfall patterns, featuring the four most extreme patterns at the edges of the classification (i.e. Nodes: 1, 4, 9, and 12). Node 1 features heavy precipitation (about 10mm day^{-1}) throughout the domain and maximum precipitation (about 15mm day^{-1}) around the mountain peak, Node 12 shows little or no rainfall over most of the domain. Node 4 is characterized with moderate precipitation ($> 5\text{mm day}^{-1}$) at the south-west part of the domain and little or no precipitation ($< 1\text{mm day}^{-1}$) over the north-east. The reverse is the case in Node 9. The rainfall patterns in other nodes show a smooth transition among the four extreme patterns. However, the rainfall distribution patterns over the Drakensberg in wet WSD generally be classified in four major patterns, namely: Heavy Precipitation Over the Domain (hereafter, HPOD: Nodes 1 and 2), Weak Precipitation Over the Domain (hereafter, WPOD: Nodes 7, 8, 11, and 12), Moderate Precipitation Over the south-west (MPSW: Nodes 3 and 4) and Moderate Precipitation over the North-East (MPNE: Nodes 5, 6, 9 and 10). The high frequency of the intense rainfall patterns (e.g. Node 1) during the DJF season is logical given the location Drakensberg in the summer rainfall region of South Africa, which receives its maximum rainfall during the DJF season [Dedekind et al. \(2016\)](#); [Nel \(2008\)](#). On the other hand, the high frequency of the light rainfall patterns (e.g., Node 4) in MAM and JJA can be associated with the presence of stronger the continental high-pressure system over Drakensberg during this period of the year (Figure 4.2) over the Drakensberg.

Figure 4.6 shows that the transport of moisture from the Indian ocean into the sub-continent is the main source of moisture for precipitation over the Drakensberg during the wet SWD. However, the precipitation amount and spatial distribution depends on the trajectory of the moisture before reaching the mountain. This moisture trajectory is controlled by the orientation of the South Indian High and the continental trough. The south-easterly wind of the SIH transports the moisture into the sub-continent north of 30°S while the continental trough channels moisture southward towards South Africa and the Drakensberg. However, the more southerly the south-easterly is, the less the moisture that reaches the Drakensberg (e.g., Figure 4.6, Node 12). But the more easterly the wind is, the more the moisture that reaches the Drakensberg and the wider the precipitation over the mountain (e.g., Figure 4.6, Node 1). In addition, the north-west to south-east orientation of the trough favours precipitation over the Drakensberg Mountain because it channels more moisture towards the Drakensberg. This result is consistent with previous studies (e.g., [Omar and Abiodun, 2017](#); [Ndarana et al., 2022](#)) on South African precipitation and moisture transport from the surrounding oceans. For example, [Omar and Abiodun \(2017\)](#) linked the widespread extreme rainfall events over the East coast of South Africa with moisture from the Indian Ocean while [Ndarana et al. \(2022\)](#) showed that a ridging high brings moisture from different parts of the Indian Ocean into the south African subcontinent at different times steps of its evolution.

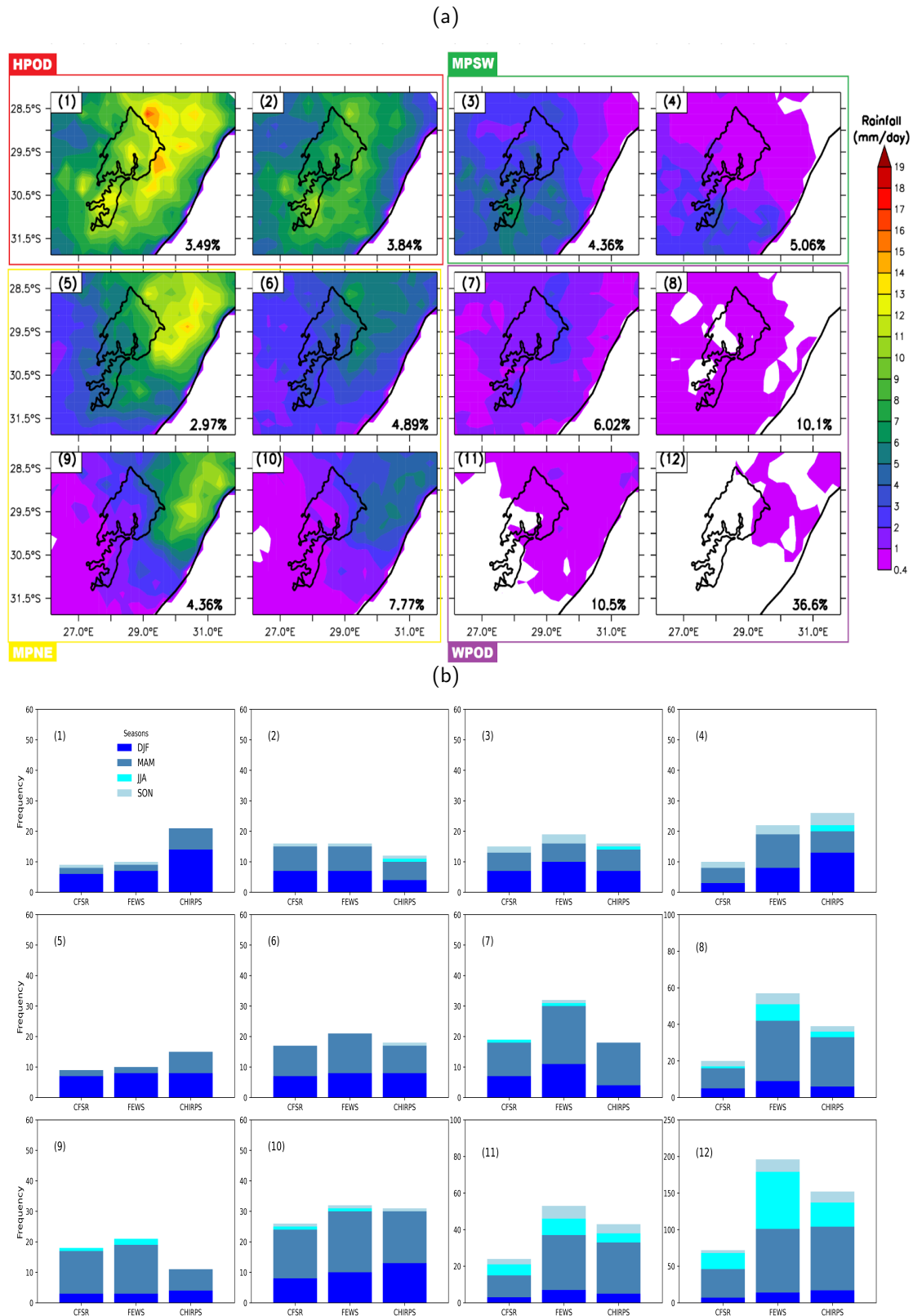


Figure 4.5: The SOM classification of wet WSD rainfall patterns (panel a; 4x3 nodes) and the seasonal frequency of the patterns (panel b) as depicted observations (ARC2 and CHIRPS) and reanalysis (CFSR) in the period 1983–2012. The identification number for each node is indicated at the upper left corner. In panel (a), the rainfall over the ocean has been masked out; the black contour (2000m topographic contour) shows the location of the mountain peak; the percentage contribution of each node to the total wet WSDs are indicated at the lower left corner of each panel; and similar patterned nodes are grouped: as HPOD (Heavy Precipitation Over the Domain), WPOD (Weak Precipitation Over the Domain), MPSW (Moderate Precipitation over the South-West), and MPNE (Moderate Precipitation over the North-East).

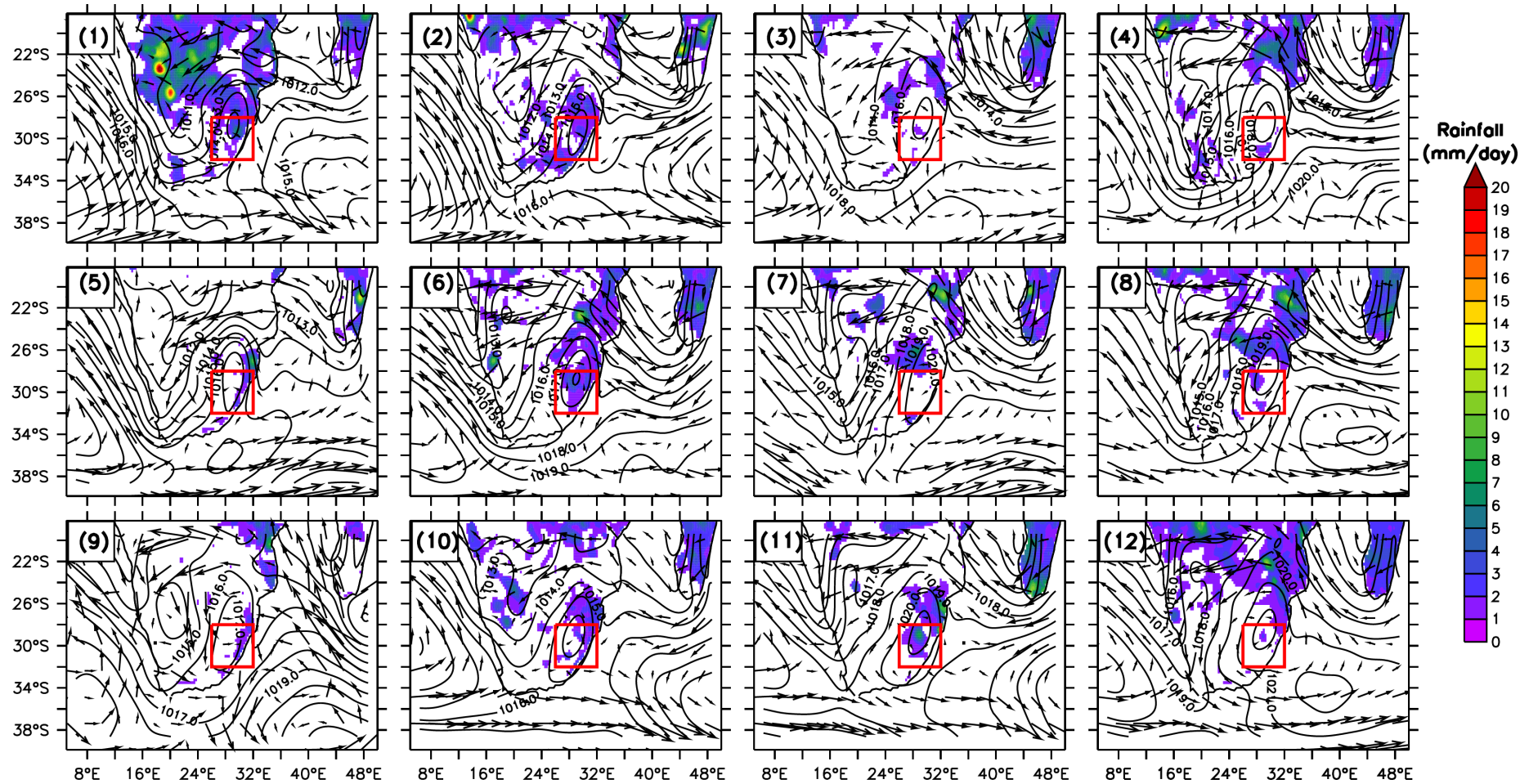


Figure 4.6: The composites of synoptic atmospheric conditions associated with wet WSD rainfall patterns shown in Figure 4.5a: FEWS and CHIRPS rainfall (SDII, shaded); CFSR mean sea level pressure (contour) and CFSR 850-hPa moisture flux (vectors). The season used for each pattern (i.e., when the pattern is most frequent) and the corresponding geostrophic wind (averaged over the red box) are indicated in the bottom left and right respectively.

4.4 WRF simulation over the Drakensberg

The results in the previous section indicated that CFSR underestimates precipitation amounts during the wet WSDs because the coarse resolution of the reanalysis make it to compromise the representation of small-scale features over the mountain. To examine the extent to which downscaling of CFSR can improve the product, WRF was applied to downscale the CFSR dataset. The WRF downscaling experiment was discussed earlier in the chapter. The simulation in the experiment focused on the downscaling CFSR results in Nodes 1, 3 and 9 which are good representations of HPOD, MPSW and MPNE patterns, respectively.

Figures 4.8–4.11, which compare the results of the WRF downscaling with CFSR and observation, show that the downscaling improves the quality of simulated rainfall fields. For example, in contrast to CFSR results, all the WRF simulations (WRF18, WRF6 and WRF2) reproduce the observed widespread precipitation over the Drakenberg in Node 1, the moderate precipitation over the north-eastern part of the mountain in Node 5 (Figure 4.9), and the moderate precipitation over the south-west part of the mountain in Node 9 (Figure 4.10). In addition, the downscaling increases the correlation between the simulated and observed precipitation fields and lowers the biases in the simulated precipitation fields by increasing the magnitude of the precipitation. This is because the local scale circulations and their contributions to precipitation on WSD are better captured in the high-resolution WRF simulations than in coarse resolution CFSR results. This is consistent with previous studies that show that dynamical downscaling of reanalysis adds values to the simulated precipitation fields (e.g., Giorgi, 1990; Marbaix et al., 2003). These studies show that the higher the resolution of the regional climate models, the better the representation of topography and other surface characteristics.

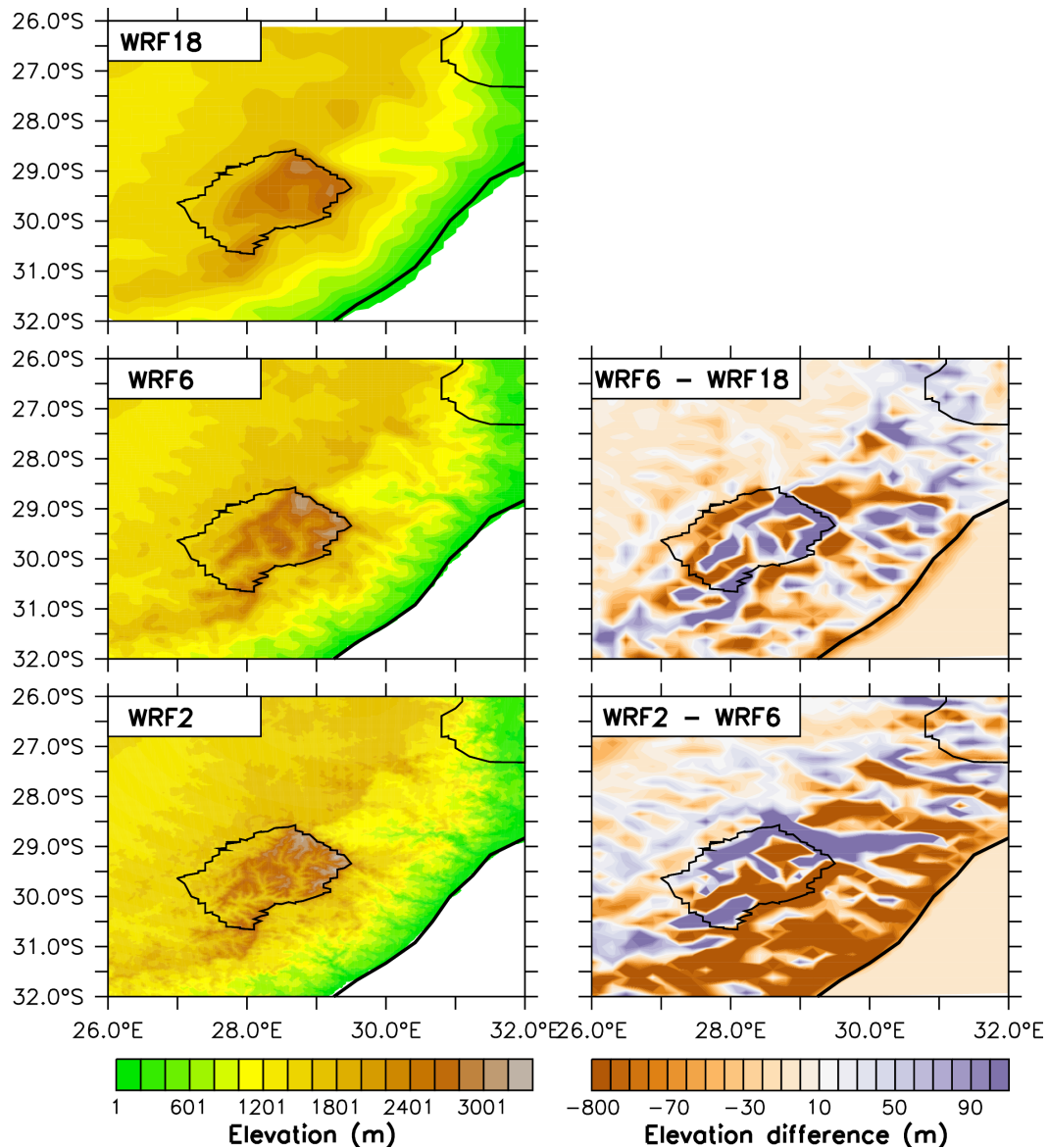


Figure 4.7: Comparison of WRF model topography at different horizontal resolutions (i.e. 18km, 6km and 2km and respectively denoted WRF18, WRF6 and WRF2). The left panels shows the terrain height (elevation in metres) at the default grid size/resolution used for the simulations. The right panels show the difference between the low resolution and high resolution topography after regriding to the 18km grid.

To examine the extent to which the WRF model topography is sensitive to the horizontal resolution over the Drakensberg, the model topography at different horizontal resolutions (i.e., 18 km, 6 km and 3 km and respectively denoted WRF18, WRF6 and WRF2) are compared in Figure 4.7. Figure 4.7 shows that the higher the resolution, the higher the terrain height (left panels). However, some areas in the domain are characterised by higher terrain height (elevation) in the lower resolution grid compared to the higher resolution grids as shown by the right panels in Figure 4.7.

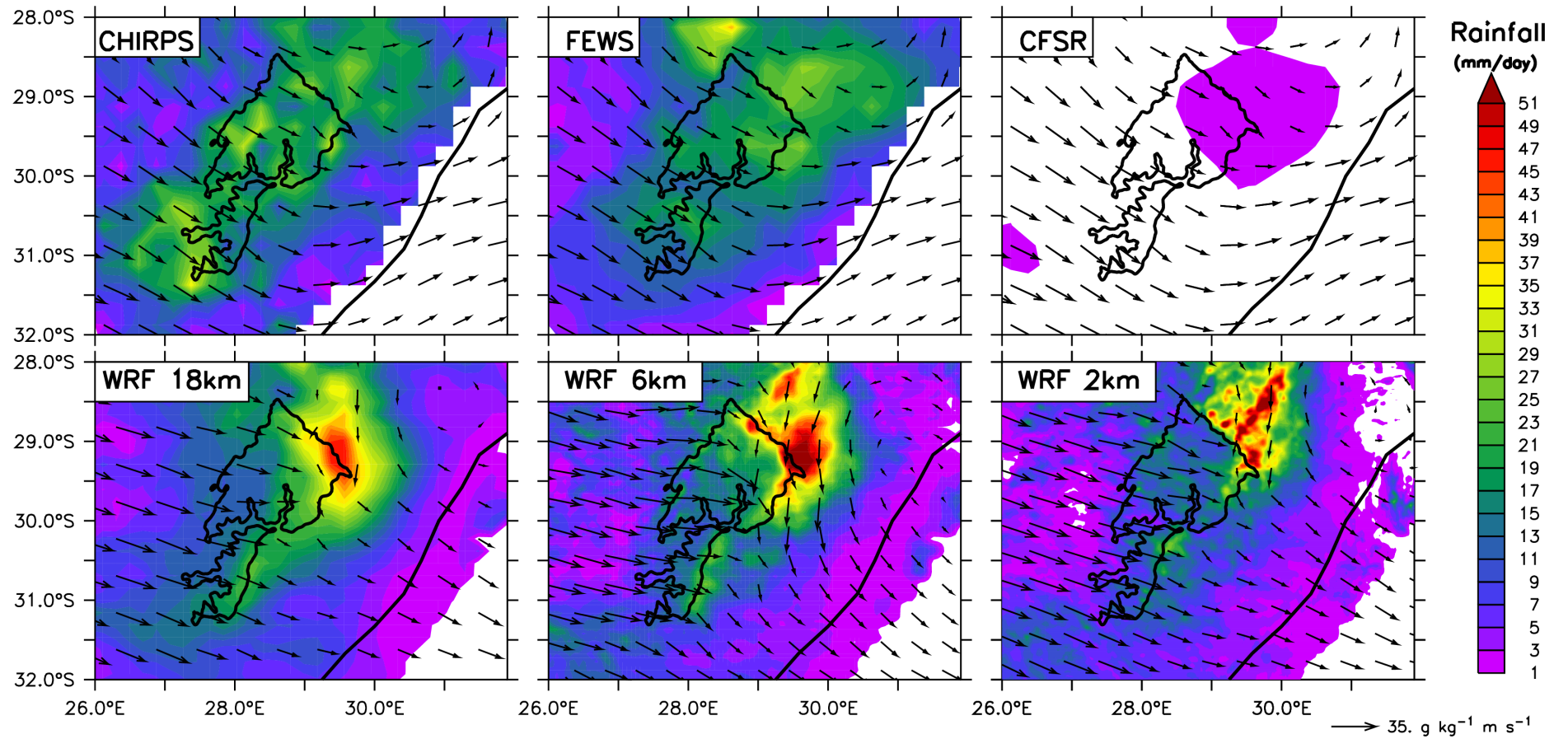


Figure 4.8: The composite of Node 1 as observed by CHIRPS and ARC2, and depicted by CFSR, and simulated by the WRF model (at 18km, 6km, and 2km).

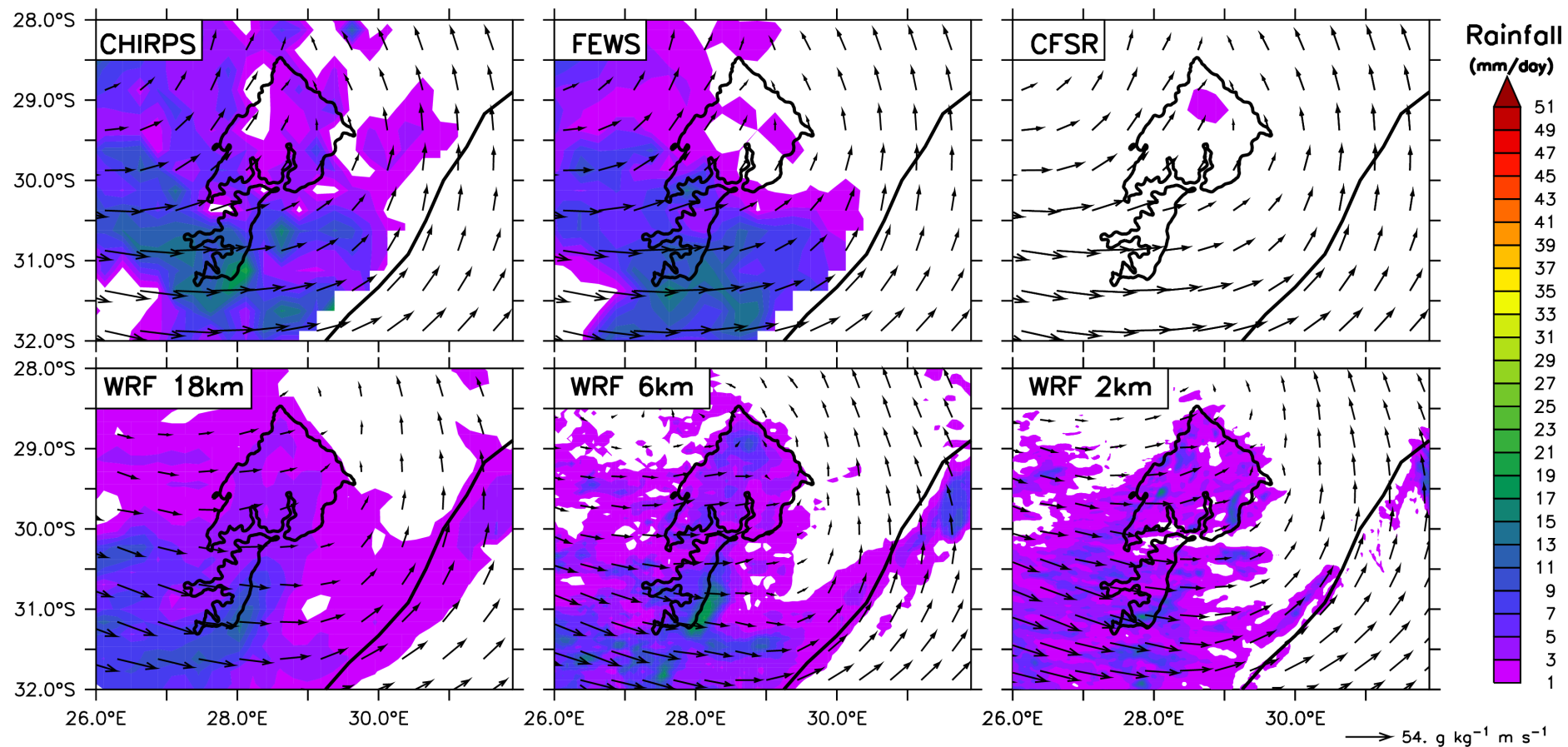


Figure 4.9: Same as in Figure 4.8 but for Node 3.

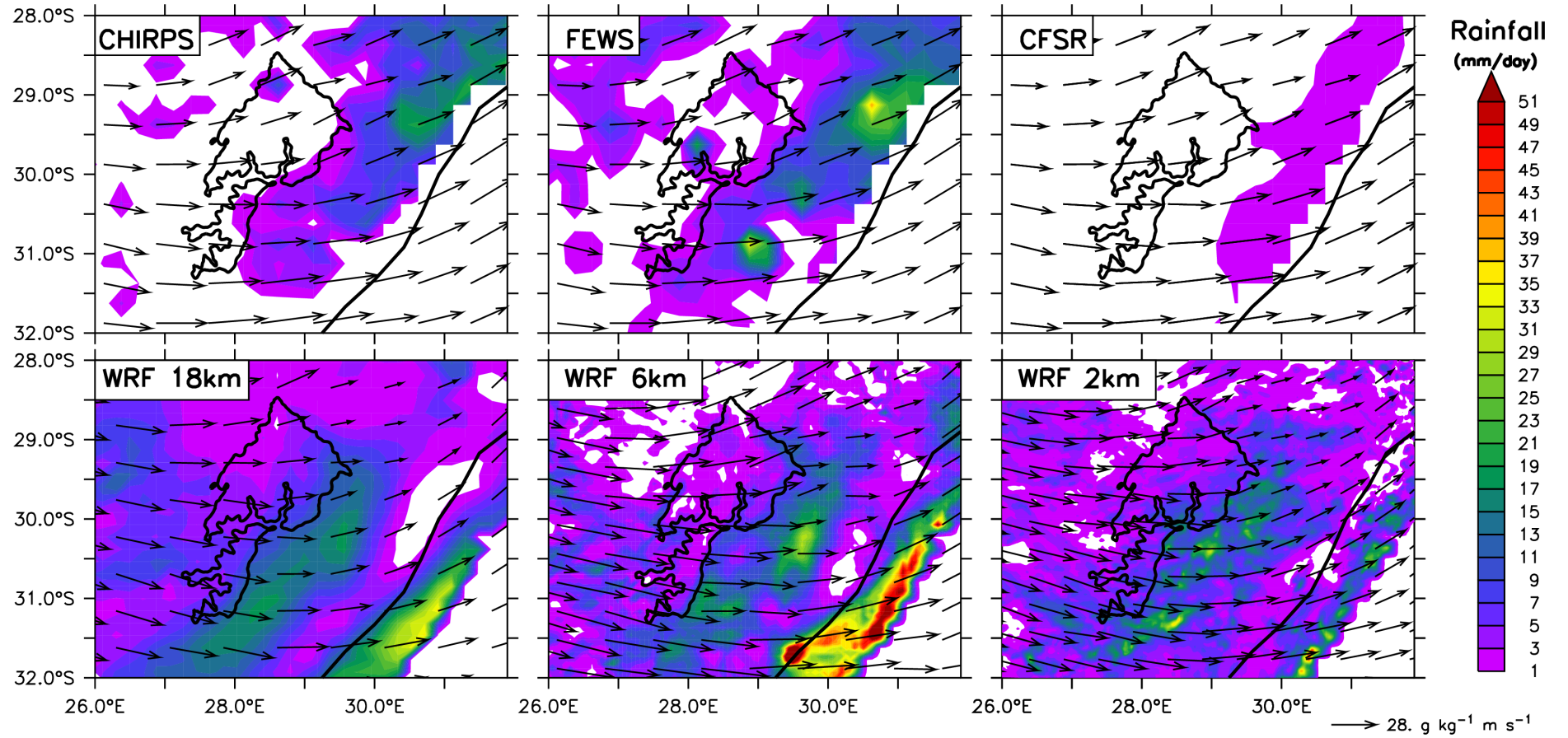


Figure 4.10: Same as in Figure 4.8 but for Node 9 of pattern WSD3.

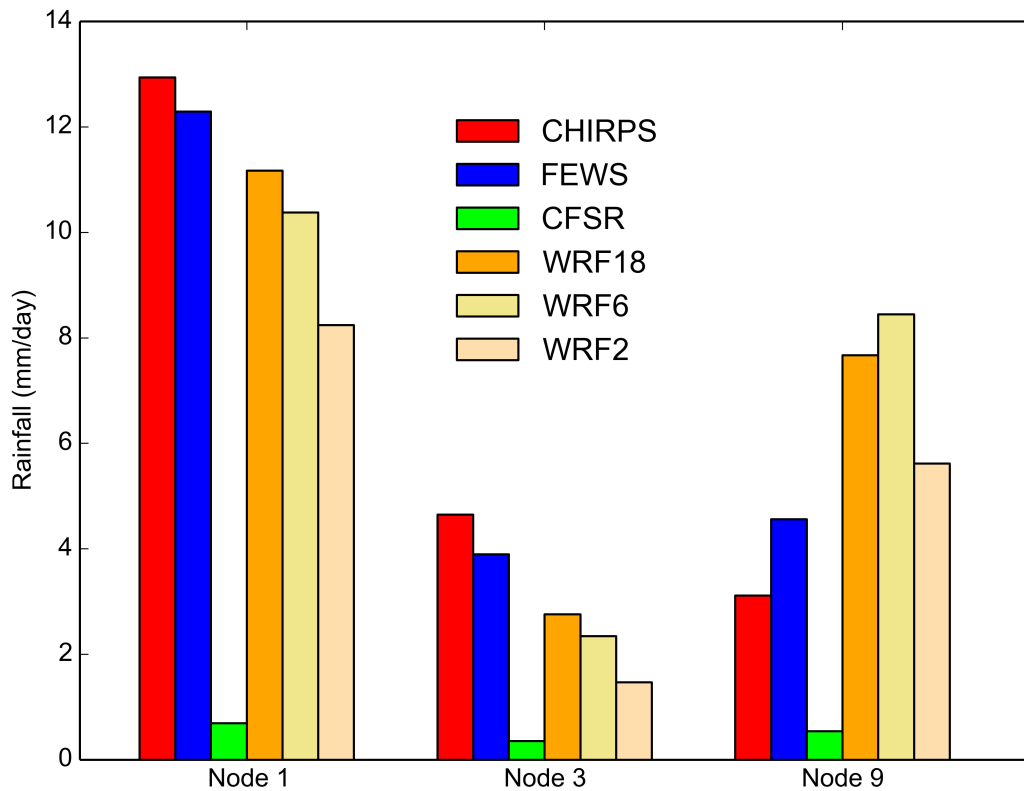


Figure 4.11: A comparison of observed (CHIRPS and FEWS (i.e. ARC2)), reanalysis (CFSR), and simulated (WRF) rainfall over the Drakensberg for Nodes 1, 2 and 9.

However, while the WRF downscaling improves the simulation of the precipitation, there are still notable biases in the WRF simulations. For example, the simulations grossly overestimate precipitation at the north-east of the mountain peak in Node 1 (Figure 4.8) and underestimate it in Node 9 (Figure 4.10). In addition, they overestimate the precipitation at the south-east in Node 9. In total, they underestimate the mean precipitation over the mountain in Nodes 1 and 3 but overestimate it in Node 9. The bias can be attributed to several reasons. Firstly, it could be due to the quality of the boundary condition data provided by the CFSR. For instance, the area of wet bias in WRF simulations in Node 1 corresponds to where CFSR also produces precipitation due to moisture convergence synoptic-scale moisture convergence. An overestimation in the moisture transport and convergence at the synoptic scale could lead to wet-bias in precipitation simulation at the local scale (Sahana et al., 2019). Secondly, the bias may be attributed to deficiencies in the WRF dynamic core or parameterization schemes (e.g. convection and boundary layer parameterization schemes). The convection scheme may be too sensitive to topography or moisture convergence. Lastly, the differences between the observation and WRF simulations may be due to uncertainty in the satellite observation datasets. For example, in all the nodes, there are noble disagreements between the two datasets on the magnitude and spatial distribution of precipitation of the Drakensberg. Several studies have reported uncertainties in satellite datasets and attribute them to the differences in satellite resolutions and orbits. The results of the downscaling also reveal that an increase in WRF simulations does not necessarily imply a better simulation of WSD

precipitation (Figures 4.11). While the increase in the model simulation enhances the quality of the simulated precipitation in some cases (i.e., WRF18 and WRF2 in Node 9), it deteriorates in other cases. The non-linear relationship between model performance and horizontal resolution may be attributed to the sensitivity of the parameterization schemes to model resolution.

Figure 4.12 shows that local features (like sea breeze, local mountain winds) modulate the location of maximum rainfall and hence rainfall spatial distribution during weak synoptic days over the Drakensberg. The zonal cross sectional profile (bottom panel Figure 4.12) through the points A, B and C depicted on Figure 4.12 (top panel) for the different nodes (Node 1, Node 3 and Node 9) shows the location of peak rainfall corresponds to the sea breeze front location rather than the mountain peak (around $30^{\circ}E$ for point A, about $31^{\circ}E$ for point C). The sea breeze front is characterised by convergence around the points A, B and C of low level air flow from the Indian oceans and downslope mountain winds. This convergence resulted in uplift which produced the rainfall peak (diurnal rainfall peak- 16h00 on 30th January 1999 at point A, 20h00 on 10th March 2004 at point B and 21h00 on 13th May 2009).

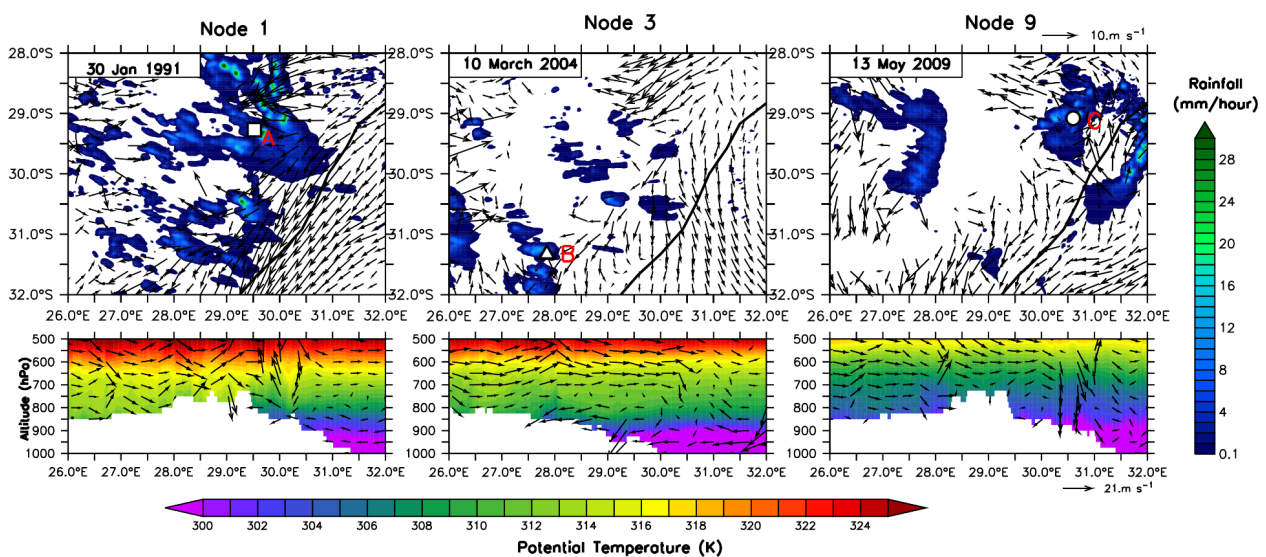


Figure 4.12: Precipitation over the Drakensberg Mountains during the wet weak synoptic condition (Nodes 1, 3 and 9) and the associated local scale atmospheric circulations. The top panels show the spatial distribution of the precipitation and the circulations during peak of the diurnal rainfall (Node 1: time 16h00; Node 2:20h00, Node 3:21h00) while the lower panels zonal cross section of potential temperature and wind (zonal and vertical wind times ten) through the points A, B and C at the same hour.

Figure 4.13 shows that on most of the weak synoptic days shown, the diurnal rainfall maximum over the Drakensberg occurs in the late afternoon– early evening (Figure 4.14). Particularly, between 16h00 and 22h00 local time. This rainfall maximum (peak) is due to the thermodynamically direct circulations caused by the diurnal cycle of insolation as presented in Figure 4.13. For example, on the 30th January 1991 at the Giant Castle station (Node 1 simulation, point A), the potential temperature vertical profile shows that near the surface (800 – 850hPa) there is a cold layer of air (potential temperature 303 – 304K) between midnight and morning (10h00). Following sunrise, heating of the shallow cold air layer in contact with the ground by way of sensible heating flux (Markowski and Richardson, 2011) induces vertical mixing and turbulence which disrupts the cold air layer in contact with the ground. This is because mixing promotes homogeneity. Water vapour concentration, wind speed and potential temperature also tend towards constant values with height. This is shown by the uniformly warm

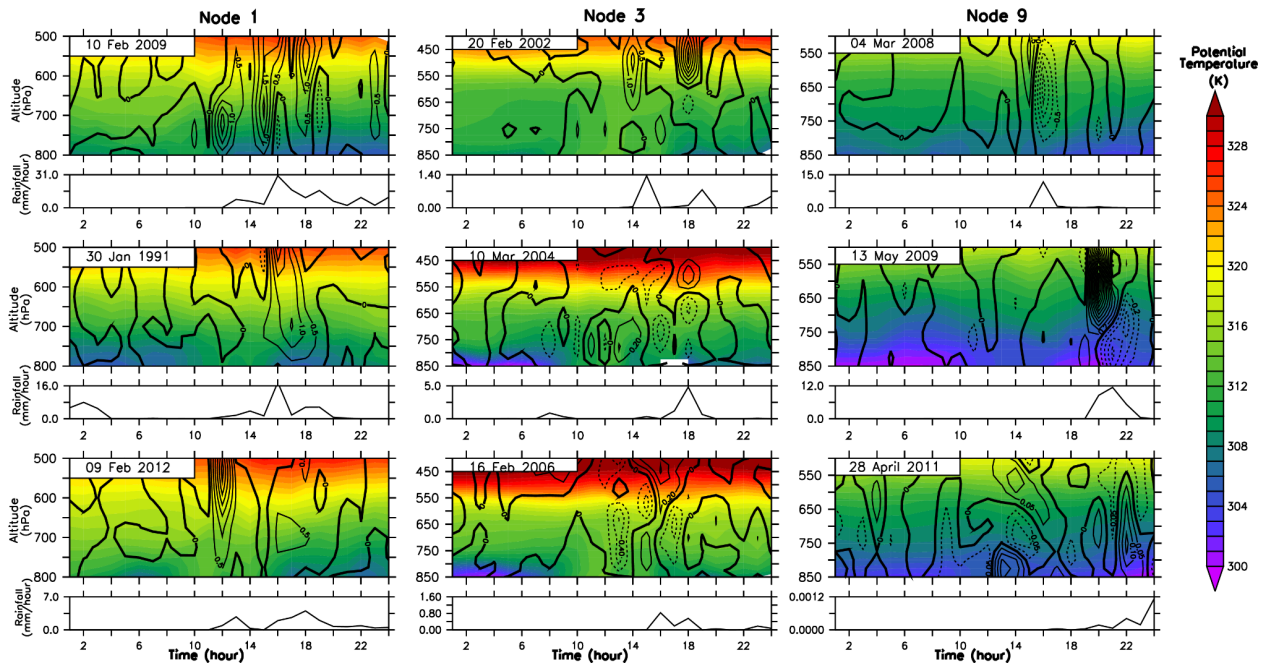


Figure 4.13: Vertical cross section of the diurnal variation of potential temperature (color fill), vertical velocity (contours: dashed and continuous lines) and associated diurnal cycle of rainfall (bottom rectangle in each panel) at three different points.

surface layer ($800 - 850 \text{ hPa}$) with potential temperature of $308 - 309 \text{ K}$ between $10\text{h}00$ and $16\text{h}00$. Continuous solar heating of the surface between $10\text{h}00$ and $16\text{h}00$ results in upward-moving thermals (positive vertical velocity contour lines). Water vapour in the rising thermals cools with height, then condenses and falls back to the surface between midday and evening ($22\text{h}00$) as rain with the peak rainfall occurring at $16\text{h}00$. The rainfall combined with sunset (decreasing sensible heat flux) result in surface cooling near the ground. This results in the re-establishment of a cool surface layer (potential temperature of $303 - 304 \text{ K}$) between $16\text{h}00$ and $22\text{h}00$ (30th January 1991, Figure 4.13). The morning ($08\text{h}00$) rainfall peak on the 10th of March 2004 (Figure 4.13) may be attributed to the land-sea differential radiative heating/cooling which results in the reduction in stability in the early morning and in turn facilitates the formation of an early morning maximum in rainfall. This shows that rainfall formation was dominated by the local-scale processes. Similar explanations hold for the late afternoon and evening rainfalls on the other WSD (see Figure 4.14).

The late-afternoon–evening rainfall over the DMR is consistent with other diurnal rainfall studies which have reported that continental convection peaks in the evenings whereas oceanic convection peaks in the early mornings. The evening rainfall peak is also consistent with the findings of Preston-Whyte et al. (1991) who used observed rainfall data from three stations (Durban, Cedera and Shaleburn near the Drakensberg escarpment) to study the relationship between diurnal rainfall events and rainfall producing types over KwaZulu–Natal. They reported that rainfall peaked in the early evening at Durban when Tropical Temperate Troughs and Ridging High Synoptic types produced rainfall but in the mid- and early-afternoon when Westerly wave types produced rainfall.

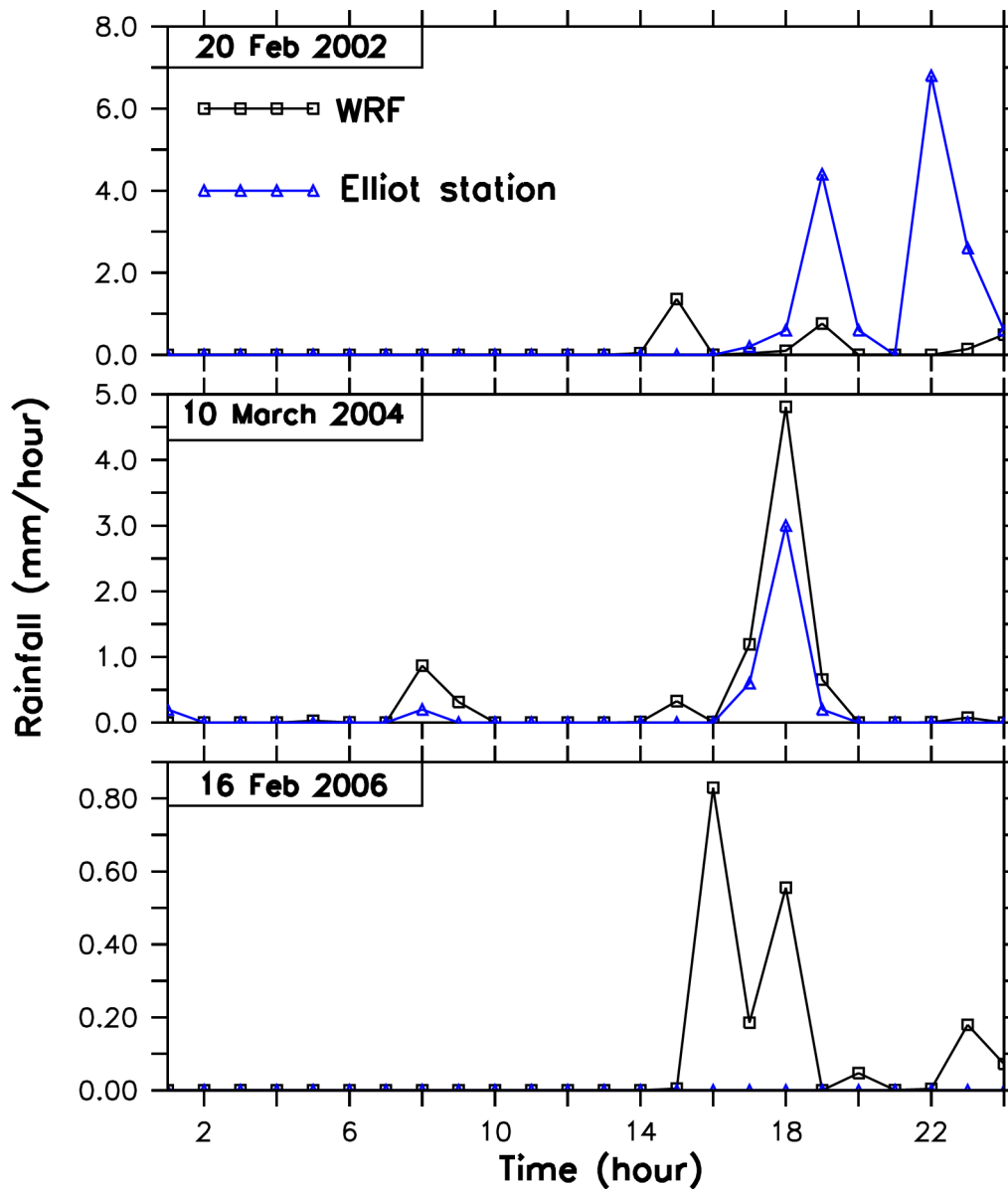


Figure 4.14: Temporal variation of rainfall at Point B (Elliot station) in Figure 4.12) on wet weak synoptic day, as simulated by WRF model and as observed by South African Weather Service.

4.5 Summary

In this study, we have investigated the characteristics of rainfall distribution over the Drakensberg under weak synoptic conditions— a condition when local scale processes dominate large scale processes. Using a combination of observation and reanalysis datasets, we identified the different rainfall patterns over the Drakensberg using SOM. We showed the weakness of CFSR in depicting the precipitation over the Drakensberg in wet weak synoptic days, then showed the extent to which the dynamical downscaling CFSR dataset can improve precipitation. The results of the study can be summarized as follows:

- Weak synoptic day (WSD) over the Drakensberg can occur in any season but mostly MAM and JJA when it accounts for 20% and 16% of the weather conditions, respectively. The occurrence

of WSD over the Drakensberg is usually associated with a high pressure system or the ridging of the South Atlantic High Pressure or South Indian Anticyclone over the mountain.

- While CFSR agrees with the observation that the wet weak synoptic days contribute more than 5% of the annual rainfall over the Drakensberg and occur mostly MAM, it underestimates the number of wet WSDs over the mountain.
- The SOM classification of precipitation during the WWSD revealed the four major patterns: heavy precipitation over the whole study domain; weak precipitation over the Domain, moderate precipitation over the south-west part, and moderate precipitation over the North-East part.
- The WWSD precipitation is fueled by moisture transport from the South West Indian Ocean into Southern Africa, but the magnitude of precipitation depends on the orientation of Indian Ocean Highs and the continental trough, both of which modulate the trajectory path of the moisture transport.
- CFSR underestimates the magnitude of precipitation in all the major WWSD precipitation patterns but the downscaling of CFSR dataset with WRF improves the quality of the simulated precipitation fields. However, WRF simulation improvement is not linear with increase in the model horizontal resolution.

CHAPTER 5

Simulating widespread extreme rainfall events over the Drakensberg using WRF and MPAS models

This chapter reports the study on widespread extreme rainfall events over the Drakensberg. The major goal of the study was to evaluate performance of two climate models in simulating the characteristics of Widespread Extreme Rainfall Events(WERE) over the Drakensberg and in linking them with synoptic systems over Southern Africa. The two climate models are the Weather Research and Forecasting (WRF) model and the Model for Prediction Across Scales (MPAS) presented in Chapter 3. The model simulations datasets were evaluated using upper-air atmospheric data from the Climate Forecast System Reanalysis (CFSR) and rainfall data from eight satellite products described in Chapter 3. The chapter starts by evaluating the capability of the models to simulate the climatology of rainfall and extreme rainfall indices over Southern Africa before examining the performance of the models in simulating characteristics synoptic features and WERE. The WRF experiment to simulate the atmospheric conditions over the Drakensberg used one way nesting. The WRF domain (Figure 5.1) has a horizontal resolution of $25km$ by $25km$ with 300 grid points in the west-east and 225 grid points in south-north directions. The number of vertical levels was 60 (bottom-top grid dimension). The model was applied to simulate the atmospheric condition for the period 1st January 1987 - 31st December 2016, using CFSR as initial and boundary condition dataset. The physics parameterization schemes employed for the simulations are listed on Table 5.1.

Table 5.1: MPAS and WRF model physics parameterization setup.

Parameterization scheme	WRF model	MPAS model
Microphysics	WSM-3	mp_wsm6
Longwave Radiation	RRTM	cam_lw
Shortwave Radiation	Dudhia	cam_sw
Surface Layer	Rev. MM5	sf_monin_obukhov
Land Surface	Noah	Noah
Planetary Boundary Layer	Yonsei Univ.	bl_ysu
Convection	Betts-Miller-Janjic	cu_ntiedtke

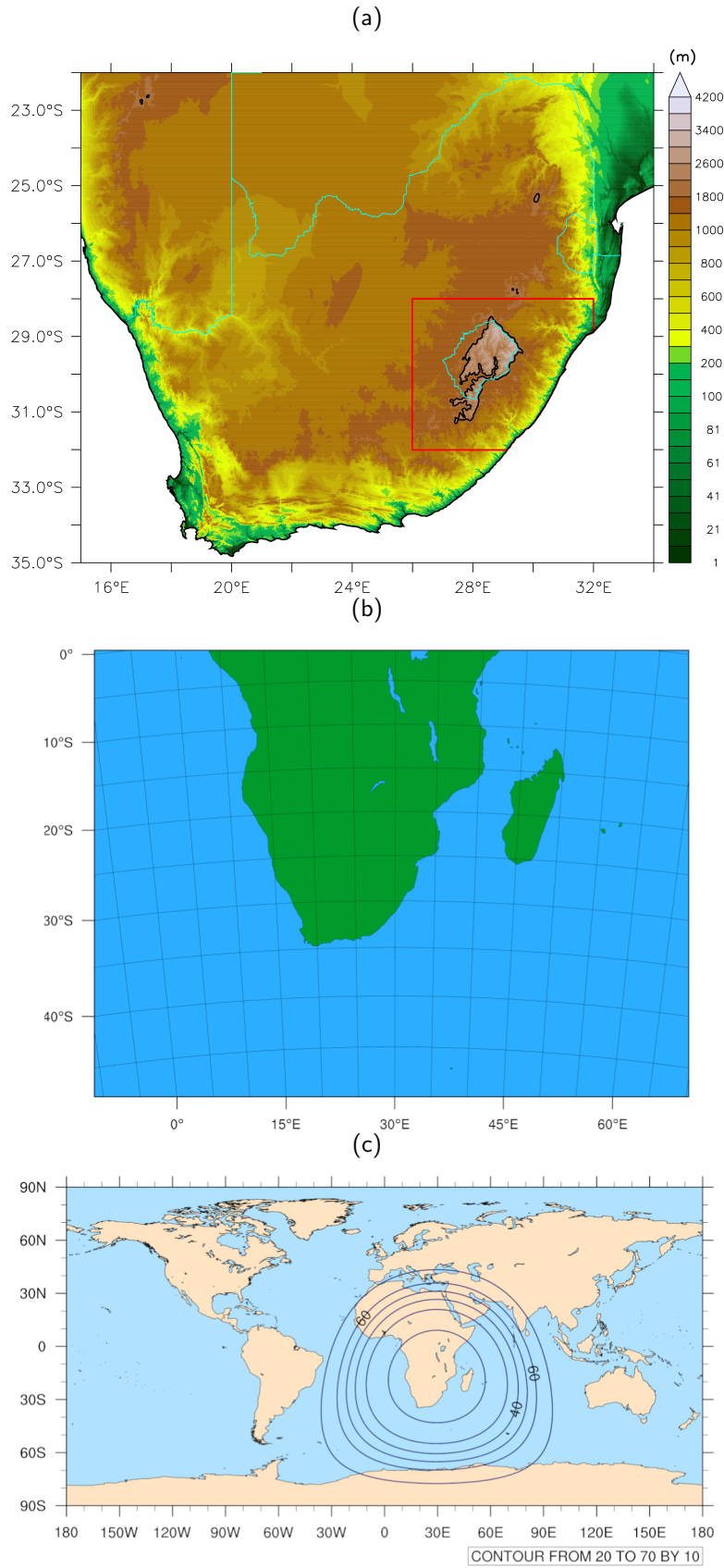


Figure 5.1: The Southern African topography (shaded; panel **a**) showing the Drakensberg Mountains area (red polygon) as used in this study. The elevation above 2000m above mean sea level is enclosed in a black contour. The simulation domain for WRF (panel **b**) and MPAS (panel **c**). The area of fine refinement for the MPAS domain is indicated by the concentric circles. The innermost circle encloses the high-resolution area of interest.

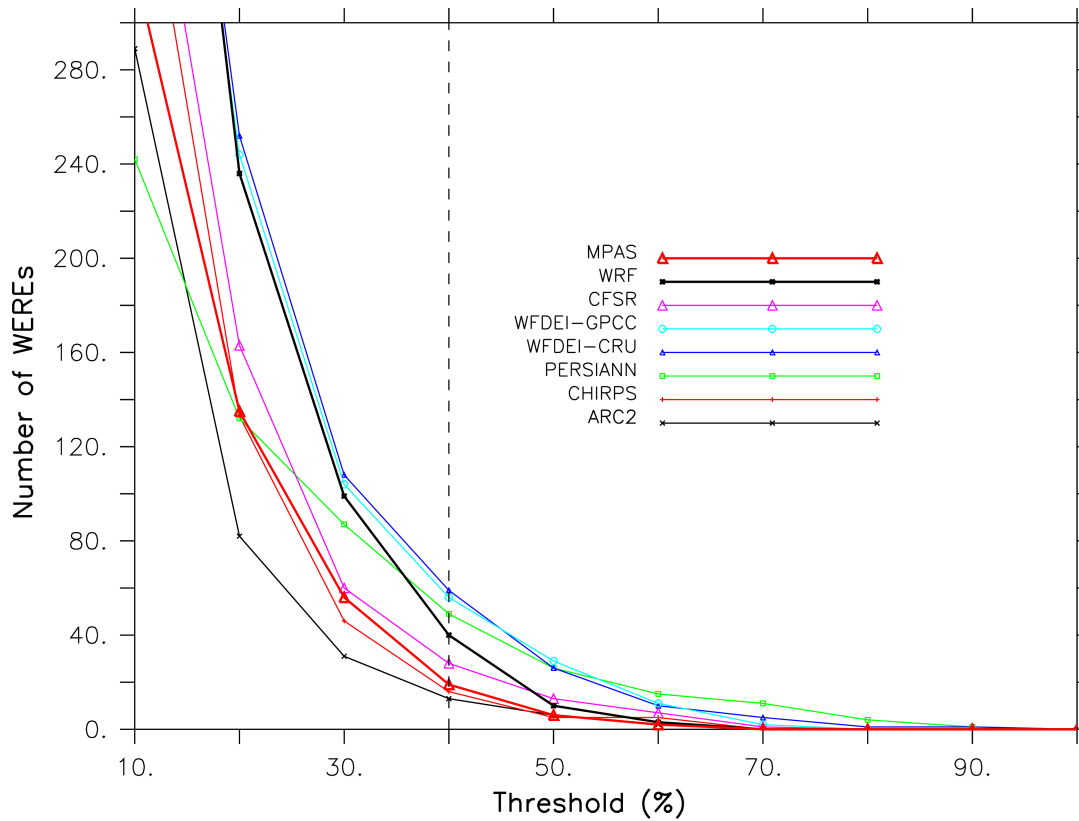


Figure 5.2: Variation in number of WEREs (over DMR) with WERE threshold criteria (i.e. the minimum percentage area of DMR the experiencing an extreme event simultaneously), as depicted by observation (ARC2, CHIRPS, PERSIANN, WFDEI-CRU, and WFDEI-GPCC), reanalysis (CFSR), and model(WRF and MPAS) datasets. The dashed vertical line indicates the threshold (i.e. 40%) used in study.

The MPAS Atmospheric model was used to simulate global atmospheric conditions but with a variable high-resolution refinement that centred on the Drakensberg. The variable resolution mesh had 163842 grid cells with resolution ranging from 92km for parts of the globe to 25km in the area of refinement (Southern Africa) as depicted by the oval shaped contours in Figure 5.1. The mesoscale reference physics suite which consists of the schemes listed on Table 5.1 except the long wave and shortwave radiation schemes that were overridden by the cam_lw and cam_sw physical parameterization schemes respectively was employed. The simulation is 1st January 1987–31st December 2016, with CFSR as initial datasets.

5.1 Rainfall and extreme rainfall indices

This section presents and discusses the capability of the models to simulate the rainfall and extreme rainfall indices presented in Chapter 3 (Section 3.4.1). Both models (WRF and MPAS) give realistic simulations of the rainfall characteristics over Southern Africa, especially over South Africa and DMR (Figure 5.2). For all the rainfall indices (RTOT, SDII, R95p, and R95pTOT), the models capture the west-east rainfall gradient over South Africa and reproduce the local rainfall maxima over the DMR as well as along the south and south-east coasts of South Africa. Nevertheless, there are notable differences in the performance of the models. While MPAS performs better than WRF in some cases, WRF performs better than MPAS in other cases. For instance, in RTOT, the spatial correlation of the simulation with

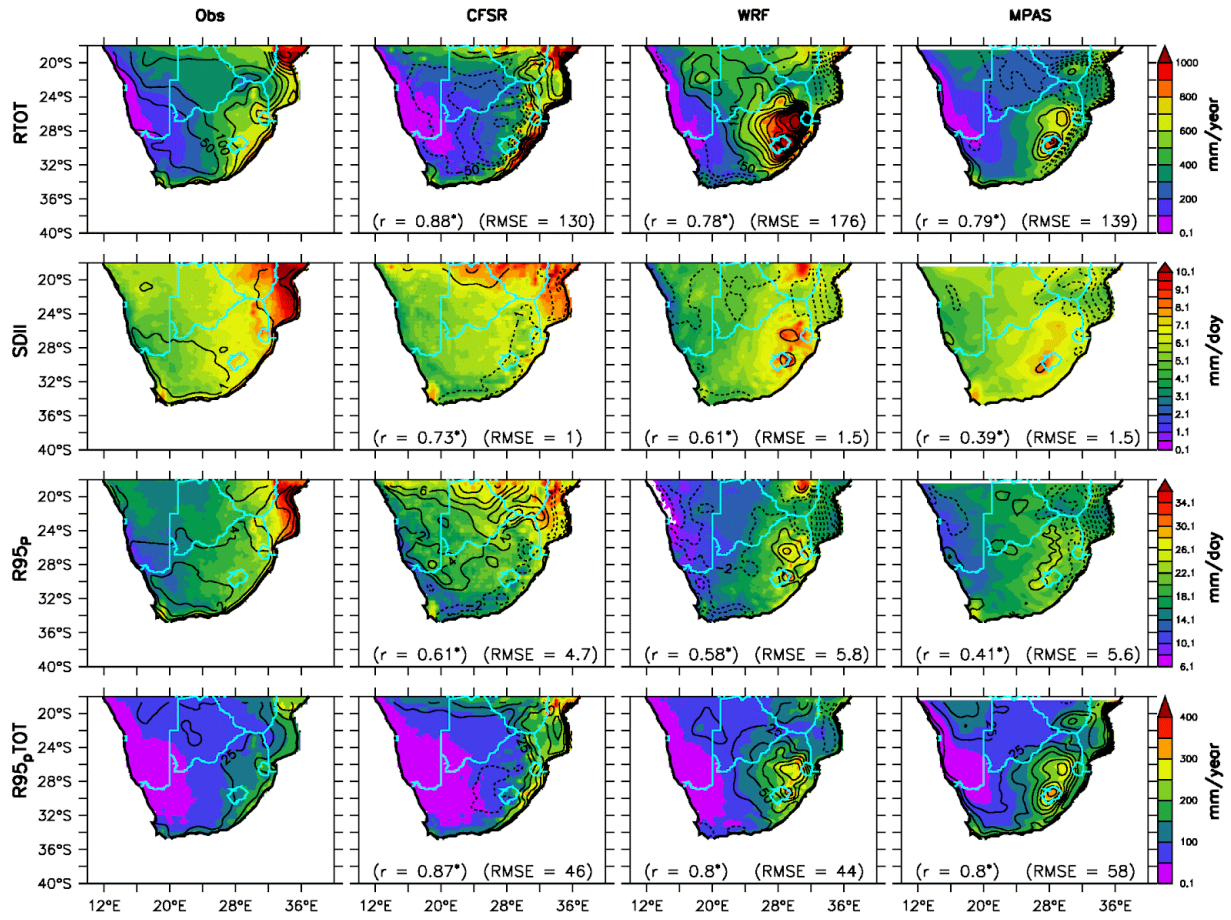


Figure 5.3: Spatial distribution of rainfall indices (RTOT, R95pTOT, SDII and R95pWET) over the Southern Africa as depicted by observation (Obs: mean of FEWS, CHIRPS, PERSIANN, WFDEI–CRU, WFDEI–GPCC), a reanalysis (CFSR) and simulations (WRF and MPAS). The contours in observation panels (Obs) show the uncertainty in the observations dataset (i.e. standard deviation), the contours in other panels (CFSR, WRF and MPAS) show biases (with respect to the Obs), while the corresponding spatial correlation (r) and root mean square error (RMSE) are also indicated. The correlation values that are significant are asterisked.

observation is higher for MPAS ($r = 0.79$) than for WRF ($r = 0.78$); the RMSE of the stimulation is also lower for MPAS (RMSE = 139 for MPAS; RMSE = 176 for WRF). The major shortcoming of both models in simulating RTOT is their failure to capture the RTOT peak over Mozambique, suggesting that the simulations might not sufficiently capture the landfall of tropical cyclones over the country. Both models also overestimate RTOT over the DMR, but the magnitude of the overestimation is larger in WRF than in MPAS. This suggests that while both models exaggerate orographic rainfall over DMR, WRF, in addition, overestimates RTOT from the Tropical Temperate Through (TTT). In general, the performance of WRF in simulating RTOT is worse than the CFSR that provides its boundary condition, but the MPAS performance is similar to the CFSR.

In contrast to the RTOT case, WRF outperforms MPAS in simulating the spatial pattern of SDII. Although both models feature the same RMSE (i.e. 1.5 mm day^{-1}), the simulated pattern is much closer to the observed in WRF ($r = 0.61$) than in MPAS ($r = 0.39$). The models underestimate the SDII over Mozambique, but the underestimation is more pronounced in MPAS ($> 5 \text{ mm day}^{-1}$) than in

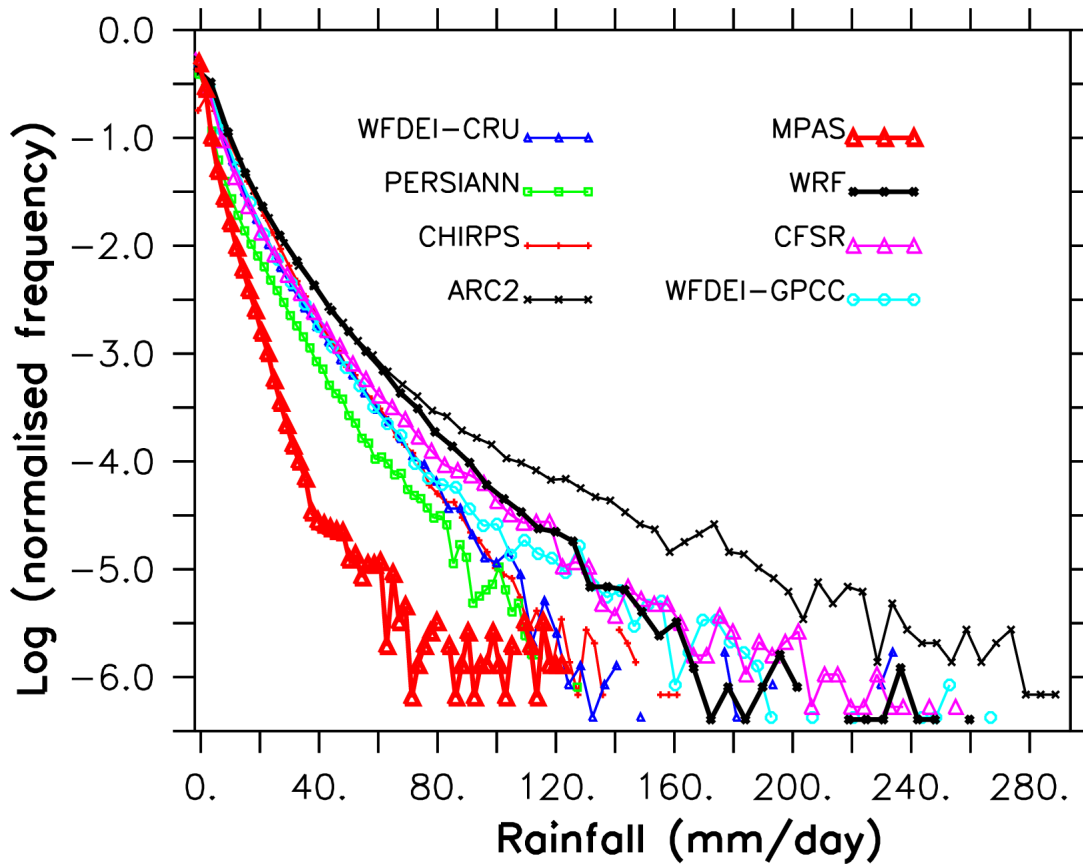


Figure 5.4: Rainfall intensity–frequency curves over the Drakensberg as depicted by observation (FEWS, CHIRPS, PERSIANN, WFDEI-CRU and, WFDEI-GPCC), reanalysis (CFSR) and simulation (WRF and MPAS) datasets.

WRF ($< 5 \text{ mm day}^{-1}$). While both models fail to capture SDII maxima over Mozambique, WRF still simulates the observed peak SDII over Zimbabwe. Nevertheless, despite the substantial wet biases of WRF in simulating RTOT over DMR and along the TTT band, the model still simulates SDII well over these areas. This inconsistency indicates that WRF overestimates the number of rainy days over these areas. The inconsistency also features in MPAS results over DMR, but it is less pronounced than that of WRF. In addition, while MPAS captures the SDII maximum over the south-west tip of South Africa, WRF does not. However, apart from the dry bias over Mozambique, both give a good simulation of SDII over Southern Africa, in that, their biases are within the observation uncertainty.

For all the datasets (observation, CFSR, WRF, and MPAS), the spatial distribution of R95p is similar to that of SDII. While the WRF simulated pattern ($r = 0.58$) is better than that of MPAS ($r = 0.41$), MPAS features less bias ($\text{RMSE} = 5.8$ in MPAS, $\text{RMSE} = 5.8$ in WRF). The performances of both models in reproducing the spatial pattern of R95pTOT are the same ($r = 0.8$), but the RMSE is lower in WRF ($\text{RMSE} = 44$) than in MPAS ($\text{RMSE} = 54$). In general, both models overestimate extreme rainfall activities (R95p and R95pTOT) over DMR and grossly underestimate R95p over Mozambique. Figure 5.4 shows that WRF and MPAS give realistic simulations of the rainfall–intensity frequency curve over the DMR. In agreement with the observation, the simulated curves feature a sharp decrease in rainfall frequency as the rainfall intensity increases. Nevertheless, the WRF performs better than MPAS in simulating the curves. While the WRF simulated curve stays within the observation spread,

MPAS simulated curve moves outside the observation spread when rainfall intensity is greater than 120mm day^{-1} . This implies the MPAS simulation tends to produce a higher frequency of heavy events than observed.

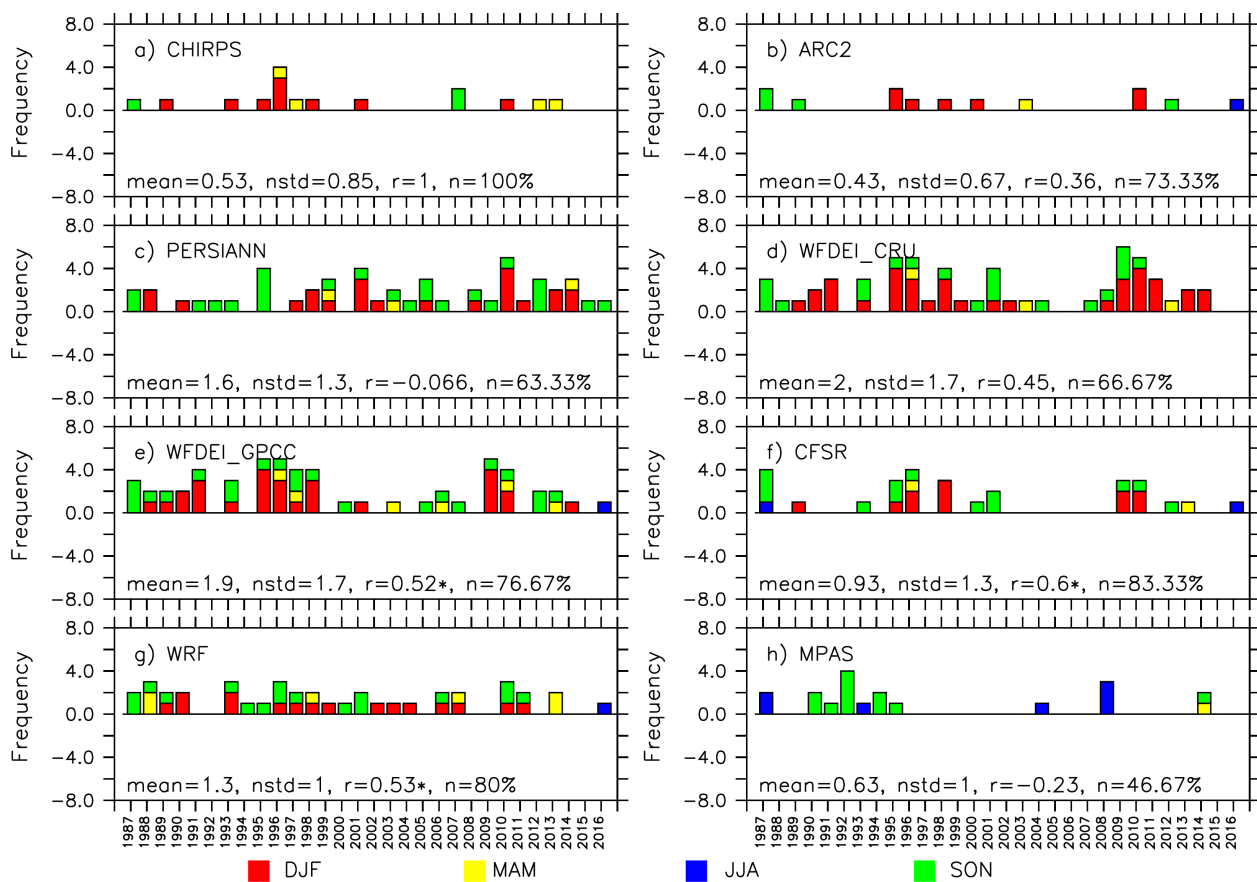


Figure 5.5: The annual variation of WERE frequency anomalies over the DMR in the period 1987–2016, as depicted by observation (FEWS, CHIRPS, PERSIANN, WFDEI_CRU, WFDEI_GPCC), reanalysis (CFSR) and simulation (WRF, MPAS) datasets. The mean and standard deviation (nstd) of the frequency are shown. The normalized standard deviation (nstd), correlation (r) and synchronization (n) of each dataset with respect to CHIRPS are indicated. The asterisk (*) shows the correlations that are statistically significant (99% significance based on t-test).

All the observation datasets (ARC2, CHIRPS, PERSIAN, WFDEI_CRU, and WFDEI_GPCC) agree that WERE mostly occurs in three seasons (DJF, MAM, and SON) over DMR and does not occur every year. However, there are substantial discrepancies among the datasets on the climatology and annual frequency of the WERE. For example, while CHIRPS and FEW feature the 60 lowest number of WERE (mean = 0.43), WFDEI_GPCC, and WFDEI_CRU feature the highest (mean = 1.9 and 2.0 respectively). The inter-annual variability of the WERE frequency is also largest in WFDEI_GPCC and WFDEI_CRU (std = 1.7 and 1.8) and lowest in FEW (std = 0.67). The datasets feature their maximum WERE frequency in different years (e.g. CHIRP in 1996 and WFDEI_CRU in 2010). The discrepancy among the observation datasets makes the performance evaluation of the models difficult. However, the statistics of WRF results (mean = 1.3 and std = 1.1) tend more towards that of PERSIAN, that of MPAS (mean = 0.57 and std = 0.67) follows the FEWS. Nevertheless, the results of both models lie within the observation datasets. Although the correlation of WRF and MPAS with CHIRPS is poor ($r = 0.49$ and

−0.02, respectively), the synchronization is high ($n = 77\%$ and 60.0% , respectively). This suggests a good agreement between the sign of the simulated and observed anomalies.

Mpungose et al. (2022) have noted that extreme rainfall at a local level over the Drakensberg are a summer phenomenon (occur in late summer) while the current study shows that they occur in three seasons (DJF, MAM, and SON). Particularly, they examined early (October–December) and late summer rainy seasons (January–March) from 1984 to 2019 using CHIRPS daily rainfall data and found that Over 60% of the top 50 extreme rainfall events occurred during late summer (January–March) with tropical lows being by far the main contributor.

5.2 Synoptic atmospheric features and WERE over the DMR

To identify dominants synoptic atmospheric features over Southern Africa, the Self-Organising Maps (SOMs, described in Chapter 3) was used classifying daily mean sea level pressure from the reanalysis (CFSR) and the two climate simulations (WRF and MPAS) into 63 groups (9×7 map). After the classification, the WEREs were mapped to the corresponding SOM nodes.

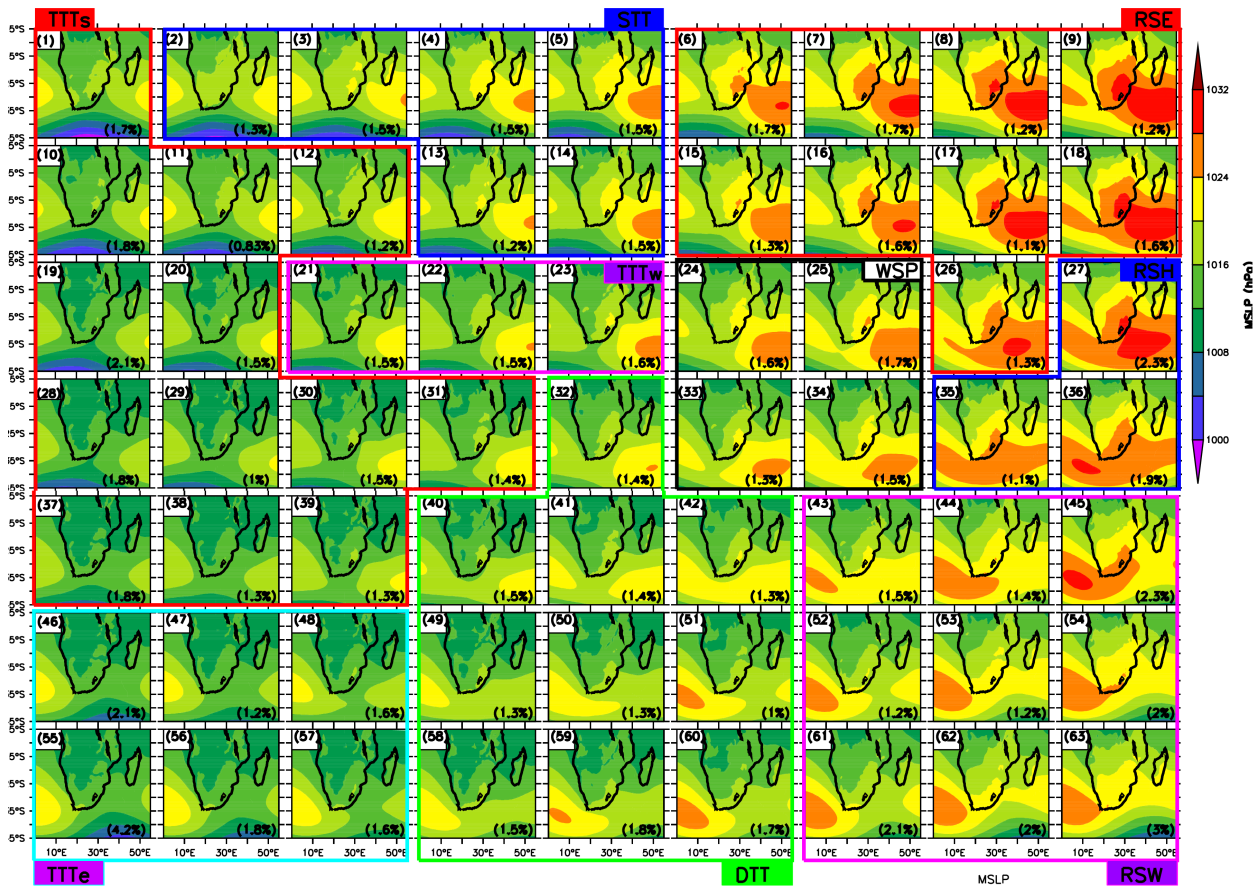


Figure 5.6: SOM analysis of daily mean sea-level pressure (MSLP) over Southern Africa (1987 - 2016), as CFSR, WRF and MPAS.

Figure 5.6 presents the SOM classification of MSLP patterns over the study domain. In the classification, the edge nodes (Nodes 1, 9, 55 and 63) show the most extreme patterns while other nodes present a smooth transition between the extreme patterns. However, a closer look at the figure shows that the

SOM nodes can be roughly divided into nine groups (i.e., TTTs, TTTe, TTTw, DTT, STT, RSW, RSE, RHS and WSP) based on the location of the dominant synoptic features in the patterns. Table 5.2 provides a brief description of each group. The SOM classification and groups agree well with those reported in previous studies (e.g., Lennard and Hegerl, 2015; Engelbrecht et al., 2015). However, the groups here show a more defined classification of the synoptic patterns than those in the previous studies. For example, while the previous studies showed only one pattern for TTT, the present study shows three groups for TTT with different locations of the temperate trough. Also, in contrast to the previous studies, the present grouping identifies DTT (also known as truncated TTT), a synoptic pattern that some studies showed to produce WERE over the south-west and south-east coasts of South Africa (i.e. Abiodun et al., 2016; Omar and Abiodun, 2017). However, the identification of more synoptic patterns in the present SOM analysis may be due to the higher number of nodes (63; 9x7) and datasets (CFSR, WRF and MPAS) used in the analysis.

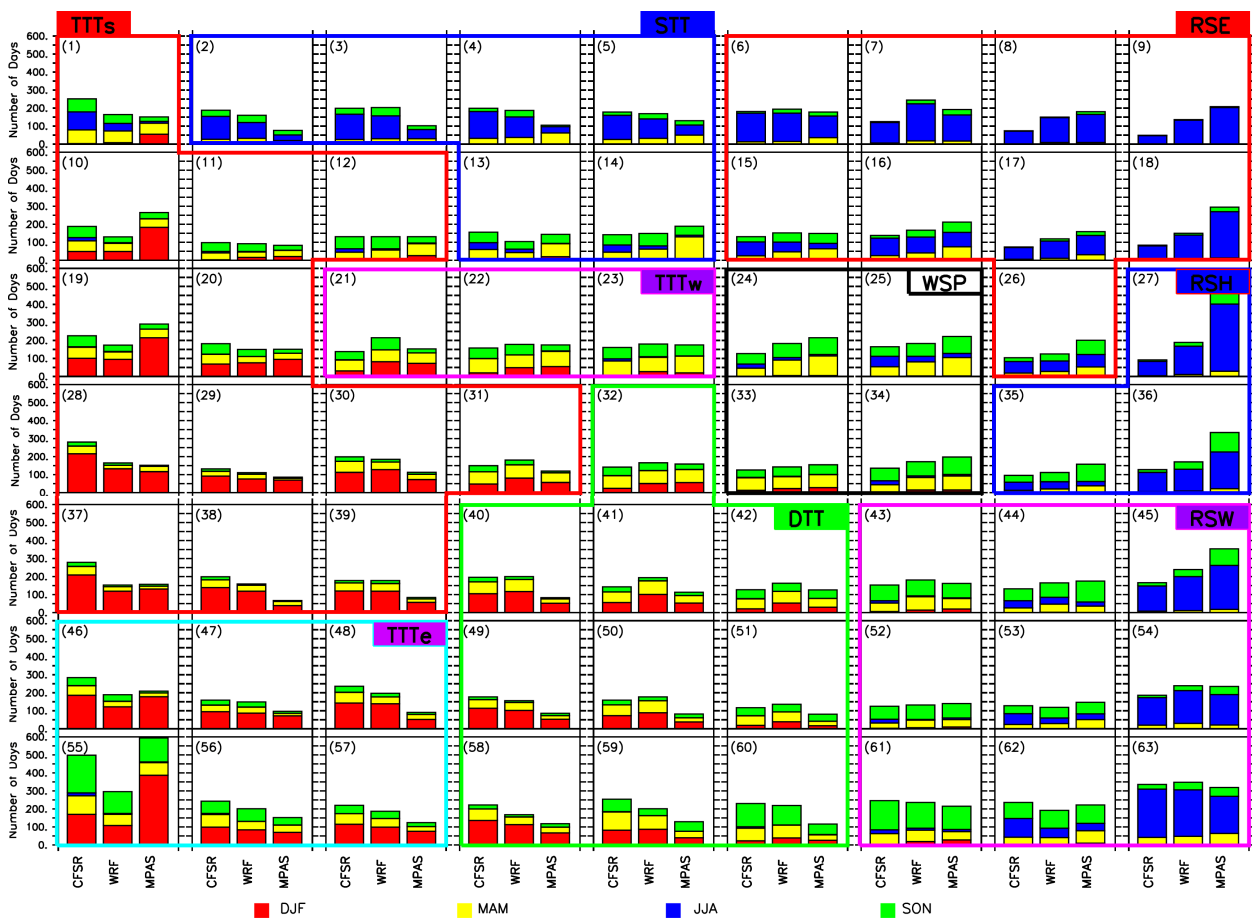


Figure 5.7: Seasonal frequency of synoptic patterns identified with SOM in Figure 5.6

There is a good agreement among the three datasets (CFSR, WRF and MPAS) on the frequency and seasonal distribution of the synoptic patterns (Figure 5.7). For example, they all agree that all the patterns along topmost row (i.e. Nodes 1-9), north-east corner (Nodes 17, 18, 26 and 27) and along the leftmost column of the SOM classification have preference for the winter (JJA) while majority of the patterns in the south-west half of the classification are most frequent in the summer (DJF). They also agree on how the change in season influences the characteristics of nodes in a group. For example, the TTTs nodes that occur most frequently in DJF (e.g. Nodes 37) have a deeper tropical trough and

Table 5.2: Description of the nine dominant synoptic weather patterns (i.e., TTTs, TTTe, TTTw, DTT, STT, RSW, RSE, RHS and WSP) identified in Figure 5.6 and the percentage contribution of each dataset (CFSR, WRF and MPAS) to the dominant patterns and to the occurrence of WERE during the major event.

Name	Description of the patterns	Frequency (%) [CFSR, WRF, MPAS]	WERE Frequency (%) [CFSR, WRF, MPAS]
TTTs	A tropical-temperate trough (TTT) with the temperate trough located south of the continent and separating the SAOH and SIOH	[39, 31, 30]	[35, 60, 5]
TTTe	A tropical-temperate trough (TTT) with the temperate trough located south-east of the continent and separating the SAOH and SIOH	[40, 29, 31]	[47, 40, 13]
TTTw	A tropical-temperate trough (TTT) with the temperate trough located south-west of the continent and separating the SAOH and SIOH	[30, 37, 33]	[0, 0, 100]
DTT	A deep tropical trough that is truncated from becoming TTT by either the link between SAOH and SIOH or the ridging of SAOH. This is also known a truncated TTT	[39, 39, 22]	[27, 59, 14]
STT	Temperate trough located at the south or south-west of the continent, featuring no tropical trough or ridging high.	[38, 35, 27]	[60, 0, 40]
RSW	Ridging high at the south-west and temperate trough to the south-east	[31, 33, 36]	[0, 50, 50]
RSE	Riding high to the south-east and temperate rough to the south-west.	[23, 34, 43]	[50, 33, 17]
RHS	High pressure at the south of the continent due to the merging of SAH and SIH	[18, 27, 55]	[50, 25, 25]
WSP	Weak synoptic pattern	[27, 34, 39]	[0, 50, 50]

weaker temperate trough than TTTs nodes that occur mostly in other seasons (i.e., Node 1). This is because in DJF, when both systems (tropical trough and temperate trough) attain their most southward positions, the core of the tropical trough presides over the sub-continent while the core of temperate

trough is shifted south of the study domain. Furthermore, in most cases, the frequency of occurrence of the synoptic pattern groups are comparable in the simulations (WRF and MPAS) and reanalysis (CFRS) datasets, especially for RSW (Table 5.2). However, there are some notable discrepancies. For example, both simulations substantially underestimate the frequency of TTTs and TTTe and grossly overestimate the frequency of RSE, RHS and WSP. In addition, WRF overestimates the frequency TTTw while MPAS underestimates that of DTT and STT.

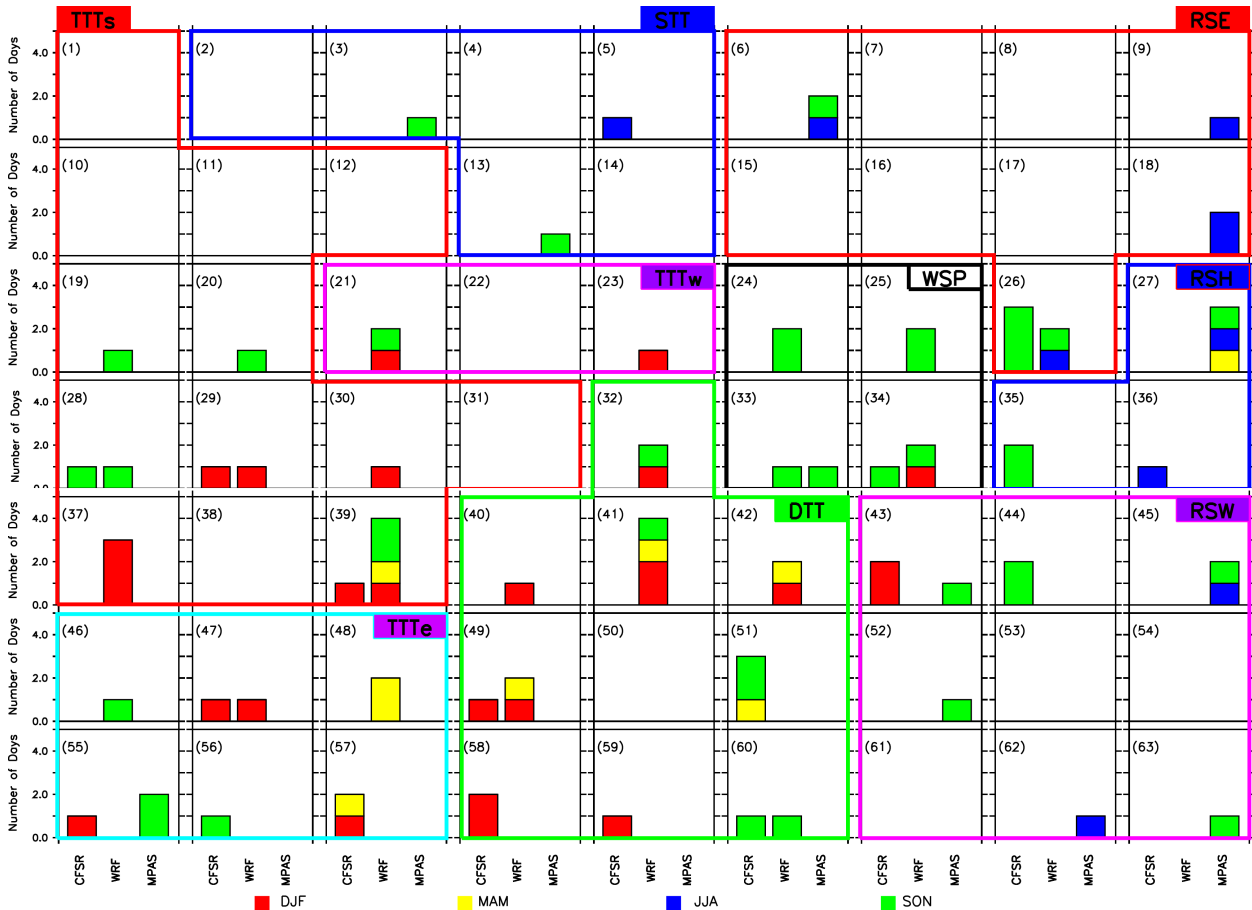


Figure 5.8: Frequency of WERE occurrence during the synoptic patterns identified with SOMs in Figure 5.3.

The datasets generally agree on the mapping of the WERE over DMR to the synoptic pattern groups, but they disagree on the WERE frequency in each group (Figure 5.8). For example, the models (WRF and MPAS) agree with reanalysis that TTTs, TTTe, DTT, RSE and RHS can induce WERE over the mountain, but underestimate the frequency of WERE in TTTe, RSE, and RHS. While WRF overestimates the frequency of WERE in TTTs and DTT, MPAS underestimates the frequency in these two groups. In addition, contrary to the reanalysis, the models produce WERE in RSW and WSP. While only MPAS features WERE in TTTw, only WRF fails to induce WERE in STT. The discrepancy among the dataset on the mapping of the WERE to the synoptic pattern groups can be attributed to several factors. The group of the synoptic patterns on only one atmospheric variable (MSLP) meanwhile several atmospheric variables (e.g. atmospheric moisture, moist static energy, etc) combine shaping the suitable atmospheric condition for WERE over the mountain. Furthermore, the discrepancy can also relate to shortcomings in the model simulations or in the reanalysis datasets. It can also be attributed to the uncertainty in

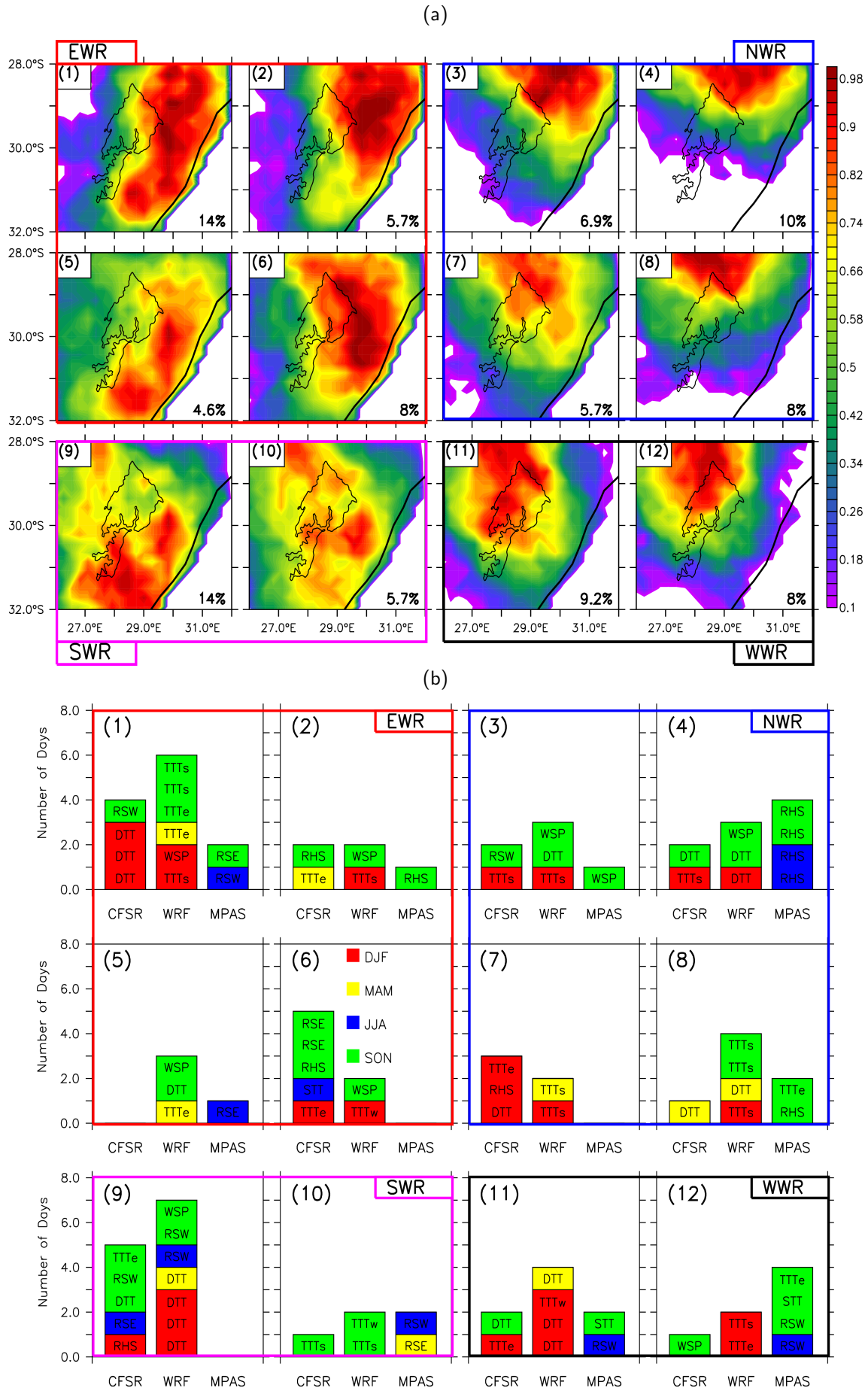
the sampling, as the number of WERE events analysed in the datasets (especially in MPAS) may be too small.

5.3 Spatial patterns of WERE over the Drakensberg

To identify the major patterns of WERE over the Drakensberg, the Self-Organizing Map (SOM, described in Chapter 3) was employed to classify rainfall patterns on WERE into 12 groups (4x3 SOM nodes).

The SOM classification of WERE patterns over DMR shows that the patterns can be further classified into four major groups based on locus of the WERE (Figure 5.9). In the first group (EWR: Nodes 1, 2 5 and 6), the core of the extreme rainfall is on the eastern side of the mountain, stretching from north-east to the south-west along the coastline. This group accounts for 34.4% of the WERE days in the combined dataset. All the datasets feature EWR (CFSR:10, WRF:13, and MPAS:6) and agree that it usually occurs in SON and MAM. However, CFSR and WRF still feature it in DJF. In the second group (NWR: Nodes 3, 4, 7 and 8), the center of the extreme event is within the north and northeast slope of the mountain. The group, which represents 23.4% of WERE days in the combined dataset, is well featured in the three datasets (CFSR:9, WRF:13, and MPAS:6). CFSR and WRF agree that NWR mostly occurs in DJF, MPAS does not feature it in DJF. In the third group (SWR: Nodes 9 and 10), clusters of extreme rainfall occur over different parts of DMR but mostly over the southern slope. This group represents 18% of WERE in the combined dataset but rarely occurs in MPAS simulation (CFSR:6, WRF:9, and MPAS:1). However, CFSR and WRF agree that SWR mostly occurs in DJF and SON. In the fourth group (WWR; Nodes 11 and 12), the core of the extreme rainfall is over the north-western slope of the mountain. WWR accounts for 14.3% of the WERE days in the combined dataset and features well in the three datasets (CFSR:3, WRF:5, and MPAS:4). All the datasets agree that WWR is most prominent in DJF and SON. However, WRF features an event of WWR in MAM while MPAS features it in JJA. Despite the disagreements among the datasets on the frequency of occurrence of the WERE groups, they all agree that EWR and NWR are the most common WERE groups, indicating that the northern and the eastern slopes are most favourable for location for WERE occurrences. The northern and the eastern slopes may be more favourable for location for WERE occurrences because of the moisture rich atmosphere. This high moisture content is due to moisture transport from the surrounding oceans (Ndarana et al., 2021). Ndarana et al. (2021) showed that moisture that is brought by ridging highs into South Africa originates from different parts of the Indian Ocean at different times steps of its evolution. The moisture is added by the ridging process from the Mozambique Channel and this moisture accumulates over the north eastern parts of South Africa, Swaziland and southern Mozambique and leads to large rainfall anomalies in Mozambique.

The areas of strong rainfall depicted by the SOM (in Figure 5.9a) indicate potential areas for damage, destruction of property, erosion, floods and loss of human life during WERE events. For example, pattern 1 depicts extreme rainfall over areas like Durban which appears to be a hotspot for extreme events (Singleton and Reason, 2006). For instance, in September 1987, a heavy rainfall (exceeding 900mm over a 3-day period) induced a severe flooding that affected the coastal areas of the KwaZulu-Natal province, damaged more than 30,000 houses, left more than 50,000 people homeless, and killed 506 people (Singleton and Reason, 2006). A similar event occurred in April 2019 and 2022 (Mpungose et al., 2022). Therefore, knowledge of the spatial extent of the hot spot areas for extreme rainfall events as identified by the SOM analysis could help in the development and implementation of mitigation strategies to protect against extreme rainfall damage in the hotspot areas.



5.4 Thermodynamic and dynamic conditions associated with the EWR pattern.

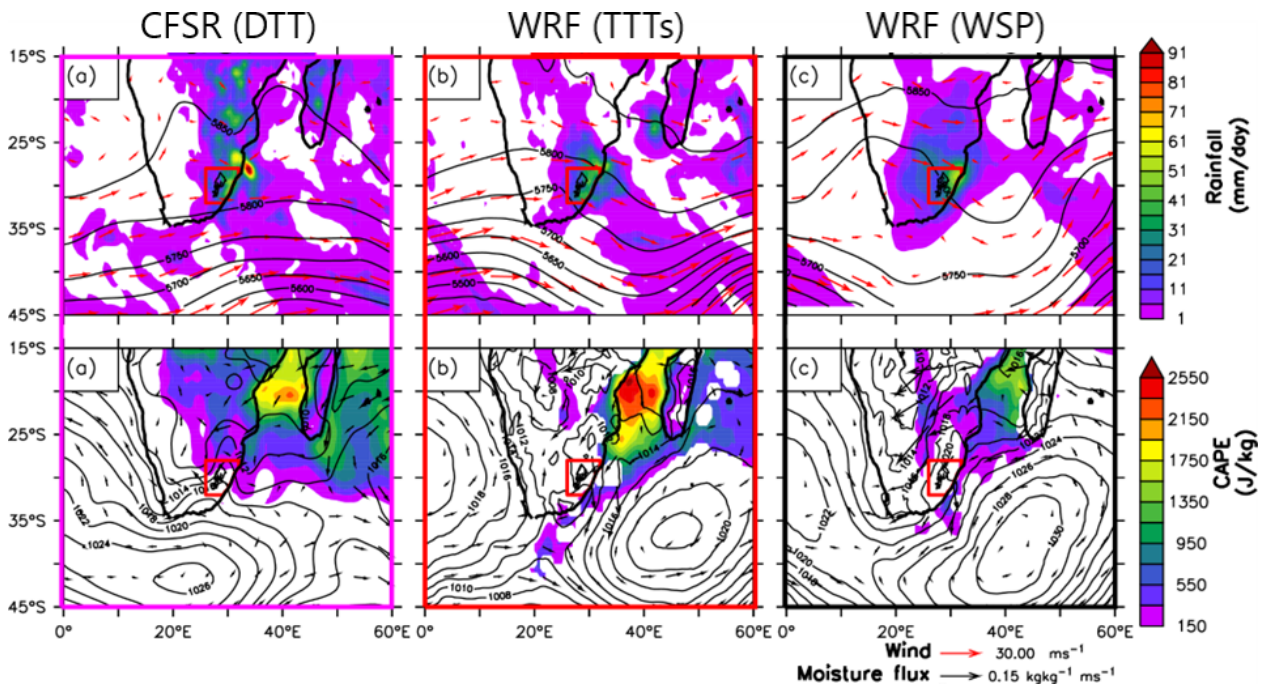


Figure 5.10: Thermodynamic and dynamic conditions associated with occurrence of EWR patterns over the Drakensberg in summer. The upper panels show the rainfall (shaded), 500hPa geopotential height and wind flow (arrows) while lower panels show the associated convective available potential energy (CAPE, shaded), the 850hPa geopotential height (contour), and moisture flux (arrows). The first column is for CFSR results under DTT synoptic pattern while the second and third columns are for WRF results under TTTs and WSP respectively.

The thermodynamic and dynamic conditions associated with the EWR pattern (in which the core of the heavy rainfall occurs on the eastern side of the mountain) as depicted by CFSR and WRF during the summer period (DJF) are presented in Figure 5.10. We focus on the EWR pattern because it gives the widest and the most intense extreme rainfall events among the four patterns (Figure 5.9). Both datasets agree moisture transport from the tropical Indian Ocean and the Mozambique channel is the major source of moisture for EWR events. This is evident by the large values of convective available energy over these areas. In CFSR results, the moisture is transported to the Drakensberg by the easterly flow induced by the ridging of the South Atlantic High (DTT) while in WRF the moisture is channelled to the mountain by the north-easterly flow from the South Indian Ocean (TTTs and WSP). The results are consistent with previous studies (Ndarana et al., 2018; Stander et al., 2016; Crimp and Mason, 1999). For example, Crimp and Mason (1999) found a confluence of tropical low and a ridging anticyclone were associated with extreme rainfall over eastern South Africa in February 1996. Stander et al. (2016) described how a ridging Atlantic Ocean high provided the moisture needed for widespread snowfall over South Africa in August 2012. Ndarana et al. (2018) showed how different types of ridging anticyclone influence the moisture transport from the ocean into the sub-continent. However, the overlapping of low CAPE and high rainfall over the Drakensberg shows that the mountain terrain plays an important role triggering the heavy rainfall. The orographic lifting along the slopes of the Drakensberg forces the conditionally unstable moist air from the Indian Ocean and Mozambique Channels to rise to the level

of free convection where the CAPE is made available. As the resulting thunderstorm, which stabilizes the atmosphere, reduces the CAPE value over the mountain.

5.5 Summary

This study has investigated the capability of the WRF and MPAS models in re-producing the characteristics of WERE events over the Drakensberg. The model simulations were compared with 5 observation datasets (ARC2, CHIRPS, PERSIANN, WFDE-CRU and WFDEI-GPCC), CFSR reanalysis to evaluate their capacity to represent past characteristics of extreme rainfall over the DMR. The rainfall characteristics were represented with four rainfall indices (RTOT, SDII, R95.5p and R95.5pTOT). Then SOM analysis was used to identify the different patterns of strong rainfall areas during WERE events and their associated synoptic circulation features.

The results of this study may be summarised as follows:

- Both models (WRF and MPAS) give realistic simulation of the rainfall characteristics over Southern Africa, especially over South Africa and DMR. For all the rainfall indices, the models capture the west-east rainfall gradient over South Africa and reproduce the local rainfall maxima over the DMR as well as along the south and south-east coasts of South Africa. Nevertheless, there are notable differences in the performance of the models. While MPAS performs better than WRF in some cases, WRF performs better than MPAS in other cases.
- All the observation datasets agree that WERE mostly occurs in three seasons (DJF, MAM, and SON) over DMR and does not occur every year. However, there are substantial discrepancies among the datasets on the climatology and annual frequency of the WERE.
- SOM analysis of grid points where extreme rainfall occurred during WERE events shows that there are four major spatial patterns of strong rainfall areas during WERE events over the Drakensberg. This study found that WEREs are associated with tropical temperate troughs, cold fronts and ridging high.

CHAPTER 6

Projected changes in precipitation characteristics over the Drakensberg Mountains

This chapter reports the study on projected impacts of climate change on the characteristics of precipitation over the DMR, using both dynamically and statistically downscaled datasets. The impact of climate change is considered at various global warming levels (GWLs) under RCP8.5. The projection is based on the two international experiment datasets described in Chapter 3. The datasets are the simulation datasets used were the Coordinated Regional Climate Downscaling Experiment (CORDEX) and the National Aeronautics and Space Administration (NASA) Earth Exchange Global Daily Downscaled Projections (NEX-GDDP, hereafter NEX). Table 6.1 shows the list of the models used in both datasets. Only the RCP8.5 (i.e., high emission scenario) datasets were analysed for this study. We used this scenario because it has the largest number of simulation ensemble members in both datasets. For most models, the RCP4.5 simulation does not attain 2.5°C or 3.0°C . Using the few available RCP4.5 simulations will compromise the comparison at these two warming levels.

This study adopted the definition of timings for GWLs used by Nikulin et al. (2018). Specifically, the timing of the GWL is the first year of a 30-year period, when the global temperature is above the desired warming level (i.e., 1.5° , 2.0° , 2.5° and 3.0°) relative to pre-industrial levels (which are defined as 1861 – 1890). The timing of the GWL can either be defined using GCM only (Nikulin et al., 2018) or using both GCMs and observation (Dosio and Fischer, 2018; Vautard et al., 2014). Both approaches consist of choosing a baseline period (i.e., an averaged window period of 15, 20 or 30 years, which is usually from the pre-industrial period) and computing the temperature difference between the baseline period (pre-industrial) and the period when the specific GWL of interest (1.5°C or higher) is reached (Dosio and Fischer, 2018; Vautard et al., 2014). However, they differ in that the approach, which uses both observation and GCM data, computes the GWL by calculating the observed global temperature rise between the pre-industrial period and the present period, before adding this to the GCM projected future warming relative to the present. This approach may result in less spread in GWLs across the models, as all GCMs are brought to the same level of warming relative to the present climate. This is because the approach assumes equal climate sensitivities across all GCMs from the pre-industrial periods to the present; it may also be affected by observational uncertainty and artificially reduced/enhanced GCM climate sensitivities (Nikulin et al., 2018). In contrast, the GCM only approach (which was used in this study and in Nikulin et al. (2018) determines GWLs from GCM experiments that are run from the pre-industrial period through to the 21st century. This provides a spread of GWLs across models (see Table 6.1) as a result of different climate sensitivities across the GCMs. This approach defines the pre-industrial period as defined in all the historical simulations of the CMIP5 models. For each downscaling approach used in this study, we have used the same GWL timing as defined by the corresponding driving GCM to extract a 30-year period for analysis.

The indices used in this study to characterize the characteristics of extreme rainfall events are discussed in Chapter 3. For each downscaled simulation (CORDEX and NEX), we computed each index during the

Table 6.1: The GCMs simulations, corresponding 30-year period for various global warming levels (1.5°C , 2°C , 2.5°C and 3.0°C) under RCP8.5 scenario, and the models used for downscaling the GCM simulations used in the study. The downscaled simulations are from NEX (i.e., SDM) and CORDEX (i.e., ALADIN, CCLM, HIRLAM, RACMO, RCA, and REMO). Detailed information on the GCMs and downscaled simulations in Déqué et al. (2017). The alphabets (b - x) and numbers (1 – 7) in brackets of the GCMs and RCMs (respectively) are used tags to represent the simulations (e.g., b7 represents BNU-ESM.SDM simulation).

GCM	Period of Global Warming levels				Downscaling models
	1.5°C	2.0°C	2.5°C	3.0°C	
BNU-ESM ^(b)	1995–2024	2009–2038	2020–2049	2031–2060	SDM ⁽⁷⁾
CanESM2 ^(c)	1999–2028	2012–2041	2024–2053	2034–2063	SDM ⁽⁷⁾ , RCA4 ⁽⁵⁾
CCSM4 ^(d)	1999–2028	2016–2045	2031–2060	2042–2071	SDM ⁽⁷⁾
CESM1-BGC ^(e)	2017–2046	2029–2058	2038–2067	2048–2077	SDM ⁽⁷⁾
CNRM-CM5 ^(f)	2015–2044	2029–2058	2041–2070	2052–2081	SDM ⁽⁷⁾ , ALADIN ⁽¹⁾ , CCLM ⁽²⁾ , RCA4 ⁽⁵⁾
CSIRO-Mk3-6-0 ^(g)	2018–2047	2030–2059	2040–2069	2050–2079	SDM ⁽⁷⁾ , RCA4 ⁽⁵⁾
EC-EARTH-r1 ^(h)	2003–2032	2021–2050	2035–2064	2046–2075	RACMO ⁽⁴⁾
EC-EARTH-r12 ^(j)	2005–2034	2021–2050	2034–2063	2047–2076	CCLM ⁽²⁾ , REMO ⁽²⁾ , RCA4 ⁽⁵⁾
GFDL-CM3 ^(k)	2009–2038	2021–2050	2032–2061	2041–2070	SDM ⁽⁷⁾
GFDL-ESM2G ^(l)	2023–2052	2040–2069	2054–2083	2066–2095	SDM ⁽⁷⁾
GFDL-ESM2M ^(m)	2020–2049	2037–2066	2052–2081	2066–2095	SDM ⁽⁷⁾
HadGEM2-ES ⁽ⁿ⁾	2010–2039	2023–2052	2033–2062	2042–2071	RACMO ⁽⁴⁾ , CCLM ⁽²⁾ , RCA4 ⁽⁵⁾
INMCM4 ^(o)	2029–2058	2044–2073	2056–2085	2070–2099	SDM ⁽⁷⁾
IPSL-CM5A-LR ^(p)	1997–2026	2013–2042	2024–2053	2034–2063	SDM ⁽⁷⁾ , RCA4 ⁽⁵⁾
IPSL-CM5A-MR ^(q)	2002–2031	2016–2045	2027–2056	2036–2065	SDM ⁽⁷⁾ , RCA4 ⁽⁵⁾
MIROC5 ^(r)	2019–2048	2034–2063	2047–2076	2058–2087	SDM ⁽⁷⁾
MIROC-ESM5 ^(s)	2006–2035	2016–2045	2027–2056	2038–2067	SDM ⁽⁷⁾
MIROC-ESM-CHEM ^(t)	2004–2033	2016–2045	2026–2055	2036–2065	SDM ⁽⁷⁾
MPI-ESM-LR ^(u)	2004–2033	2021–2050	2034–2063	2046–2075	SDM ⁽⁷⁾ , RCA4 ⁽⁵⁾ , CCLM ⁽²⁾ , REMO ⁽⁶⁾
MPI-ESM-MR ^(v)	2006–2035	2024–2053	2036–2065	2046–2075	SDM ⁽⁷⁾
MRI-CGCM3 ^(w)	2026–2055	2038–2067	2050–2079	2061–2090	SDM ⁽⁷⁾
NorESM1-M ^(x)	2019–2048	2034–2063	2047–2076	2059–2088	SDM ⁽⁷⁾ , RCA4 ⁽⁵⁾ , HIRAM ⁽³⁾

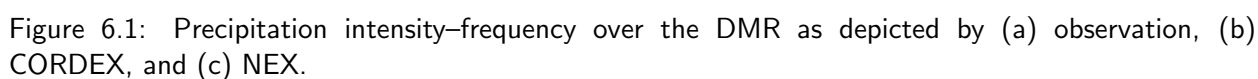
control period (1971–2000) as well as during the 30-year period when the simulation (GCM) reached a given GWL. The GWL varies from one GCM to another. We chose the period (1971–2000) as the control period because want to our results comparable with other CORDEX Africa studies (Maúre et al., 2018; Abiodun et al., 2019; Nikulin et al., 2018) and impact application studies (e.g., Sakalli et al., 2017) that used the period as their control period. To determine the impact of climate change at different GWLs, we subtracted the simulation of the reference climate from that of the GWL. This was done for each grid point within our study domain (Figure 3.1). Following Abiodun et al. (2020) and Nikulin et al. (2018), the significance of the change was assessed by using two conditions. The first condition used a t-test to check that the climate change at a given grid point was statistically significant for at least 80% of the simulations (with respect to the inter-annual variability of the reference climate (present-day)). The second condition checked that at least 80% of the simulations agreed on the sign of the change at the grid point. The climate change signal at every grid point was considered robust when both conditions are met. The threshold value of 80% was selected following Abiodun et al. (2020) and Nikulin et al. (2018).

To test the robustness of the projected changes in spatial patterns of the rainfall indices, Self-Organizing Maps (SOM) were used to classify the simulations into groups. The SOM was used to classify the projected spatial patterns of four extreme rainfall indices, the rainfall total (RTOT), the number of wet days (WDAYS), the extreme rainfall threshold (R97.5p) and the rainfall frequency (R97.5pFREQ) at four GWLs into 12 groups (i.e., a 4x3 nodes). We tested the sensitivity of our SOM classification the choice of 12 groups (4x3), 9 groups (3x3), and 16 groups (4x4) found that the general patterns of the classification do not change much. However, the 12 groups classification gives a better distinction of the pattern than 9 groups, while the 16 groups classification produces a node with no frequency, indicating too many numbers of groups. To perform the SOM, the NEX dataset was re-gridded onto the CORDEX grid. Then, both CORDEX and NEX datasets were combined to form a single dataset, which was used in the SOM analysis. However, the SOM analysis was performed for each precipitation index separately. For each SOM analysis, the contributions of the CORDEX and NEX simulations to the SOM nodes at the four GWLs were determined. This use of SOM analysis helped to reveal the diversity in the projection patterns that is usually hidden in ensemble mean results.

6.1 Evaluation of CORDEX and NEX datasets

This section discusses the capability of the CORDEX and NEX simulations to reproduce the characteristics of the rainfall indices (Table 3.3) over the DMR by comparing the simulation results with the observation results. The evaluation focuses on how well the datasets capture the rainfall intensity and frequency distribution, as well as the mean value and spatial distribution of the rainfall indices over the Drakensberg. However, to put the model evaluation into the right perspective, we first present the differences (i.e., uncertainties) in the results of the eight observation datasets (ARC, CHIRPS, PERSIANN, TAMSAT, AgCFSR, AgMERRA, WFDEI-CRU and WFDEI-GPCC) before discussing the evaluation of the model.

There is a good agreement among the eight observation datasets on the precipitation intensity-frequency curves over the DMR, but there are some discrepancies as well (Figure 6.1). While all the observation curves agree on a decrease in the rainfall frequency with an increase in the rainfall intensity, the rate of the decrease differs among the datasets. The decrease is fastest in PERSIANN and TAMSAT (which lie at the lower edge of the observation spread) and slowest in AgCFSR (which lies at the upper edge of the observation spread). This implies that, over the DMR, AgCFSR reports the most frequent heavy rainfall, while PERSIANN and TAMSAT report the least frequent heavy rainfall. The tail of the AgCFSR curve



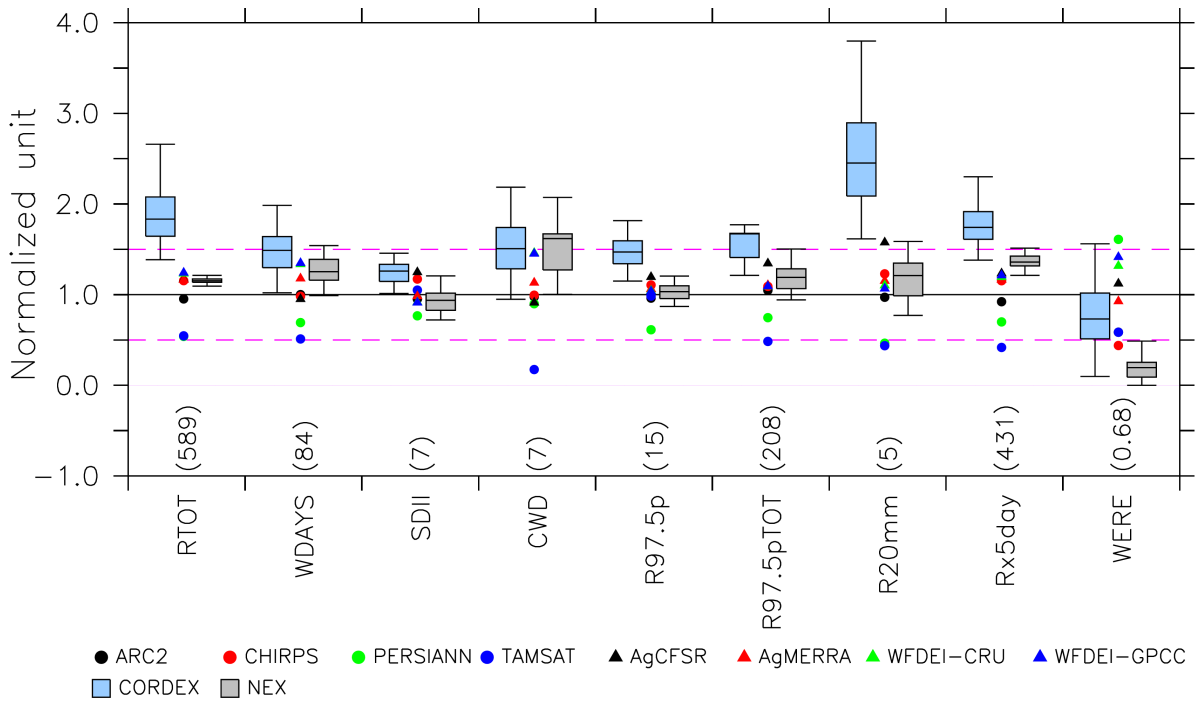


Figure 6.2: A comparison of biases in the CORDEX and NEX simulation datasets using a boxplot. The boxplot shows the minimum, 1st quartile, median, 3rd quartile and maximum values in the simulation spread. All the values are normalized with the mean of the eight observation datasets. The mean value is shown at the top of each index. The reference value for each index is 1. The purple dashed line indicates the threshold of $\pm 50\%$ bias for all the indices with reference to the observed mean.

extends beyond 120mm day^{-1} , whereas that of TAMSAT truncates below 80mm day^{-1} . Other datasets cluster together between these two extremes. The differences between AgCFSR and TAMSAT may be attributed to their data sources. TAMSAT is a satellite product, while AgCFSR is a reanalysis product (Table 3.2). It is difficult to determine which of these two sources is better. This is because cloud cover and orbiting of satellites could make the satellite product miss a heavy rainfall event or underestimate the intensity of the event; conversely, though, the interpolation and extrapolation of the data in reanalysis could also make the reanalysis product overestimate the intensity of heavy rainfall. Several studies have reported a similar discrepancy among observation products over Africa (e.g., Abiodun et al., 2020; Sylla et al., 2013). Abiodun et al. (2020) even demonstrated that the outlier datasets vary over Southern Africa cities. For example, PERSIANN and CHIRPS were identified as outliers over Cape Town, TAMSAT and PERSIANN over Lilongwe, and AgCFSR over Johannesburg. This makes it difficult to isolate outlier datasets from the model evaluation. Nevertheless, it does confirm a need for more studies on how to reduce disparities among the observation datasets used for model evaluation.

The simulation datasets (CORDEX and NEX) give a realistic representation of the precipitation-intensity-frequency curves; of the two, NEX gives a better representation (Figure 6.1). With CORDEX (Figure 6.1b), about half of the simulated curves fall within the observation spread, while the other half produce longer tails than those of the AgCFSR curve (i.e., they simulate more frequent heavy rainfall events). With NEX (Figure 6.1c), however, only four of the simulated curves (i.e., 25%) fall outside the observation spread (i.e., have a longer tail than that of the AgCFSR curve). For the mean values of

the precipitation indices over the DMR (Figure 6.2), the spread of the NEX simulations is closer to the observations than are those of the CORDEX simulations. For instance, all the NEX simulation fall within $\pm 50\%$ threshold of the observed values in six indices (i.e., RTOT, WDAY, SDII, R95.7p, R95.7pTOT, and Rx5day), and more than half of the models fall within the threshold in the three indices (CWD, R20mm and WERE). In contrast, all the CORDEX simulations only fall within this threshold in one index (i.e., SDII) and more than half of them fall within this threshold in four indices (WDAYS, CWD, R95.7, and WERE), while all the simulations overestimate the remaining indices (RTOT, R97.5pTOT, R20mm and Rx5day). The better performance of NEX than CORDEX in this regard may be because the NEX dataset is bias-corrected while the CORDEX dataset is not. The bias-corrected CORDEX dataset was not available for the study.

In simulating the spatial distribution of the precipitation indices (Figure 6.3), NEX also performs better than CORDEX in most indices, except with regard to the extreme rainfall threshold (R97.5p). Consistent with Cr  tat et al. (2012), Figure 6.3 shows that the annual rainfall (RTOT) over the DMR increases from about 500mm year^{-1} in the interior (in the west) to about 700mm year^{-1} along the coast (in the east). While both datasets reproduce this east-west rainfall gradient and extend the maximum RTOT from the east to the north-eastern top of the mountain, their maximum RTOT is higher than observed. The bias in the NEX RTOT simulation (about 100mm year^{-1}) is lower than the uncertainty in the observation datasets (i.e., the standard deviation of the datasets; about 300mm year^{-1}), but that of CORDEX (more 650mm year^{-1}) is more than the observation uncertainty. Also, the spatial correlation between NEX and the observation ($r = 0.98$) is higher than the one between CORDEX and the observation ($r = 0.89$). The CORDEX bias in RTOT can be linked to an error in the simulated number of wet days (WDAY; Figure 6.3e) and in the amount of precipitation from extreme rainfall events (R97.5pTOT; Figure 6.3q). This suggests that the rainfall parameterization scheme in the CORDEX models may be too active in triggering or releasing precipitation over the mountain. Several studies Favre et al. (2016); Fosser et al. (2015); Hohenegger et al. (2008); Pathak et al. (2019); Ratna et al. (2014) have reported that many climate models overestimate rainfall over mountains because their convective parameterizations are too sensitive to the orographic lifting of moist air. Nevertheless, CORDEX does give an excellent representation of the extreme rainfall threshold (R97.5p; $r = 0.99$), and it performs better than NEX ($r = 0.92$) in this regard. The better performance of CORDEX (than NEX) may be because the physics in the CORDEX downscaling correctly captures the extreme rainfall events from the orographic lifting of moist air, whereas the NEX statistical downscaling does not incorporate such physics. This may also explain why NEX underestimates R97.5p over the DMR (by more than 8mm day^{-1} on the mountain top). Nevertheless, while CORDEX outperforms NEX in simulating R97.5p, it underperforms NEX in simulating the other indices, because it produces too many extreme rainfall events and generates too much rainfall from these extreme events. Hertig et al. (2012) also showed that the frequency of extreme precipitation events over the Mediterranean mountains was better captured with statistical downscaling than with dynamical downscaling.

However, in general, our result corroborates previous studies that found no preference between RCM and SDM in downscaling GCMs simulations over complex topography but advocated for a combination (hybrid) of both methods (Tang et al., 2016; Yhang et al., 2017; Tran Anh and Taniguchi, 2018). For instance, Yhang et al. (2017) found that while RCM overestimated precipitation over East Asia, SDM understated the precipitation variance, but a combination of both methods produced the best results in time and space. The hybrid dynamical-statistical downscaling combines the ability of RCM to resolve fine-scale atmospheric features with low computational cost of statistical downscaling (Tran Anh and Taniguchi, 2018).

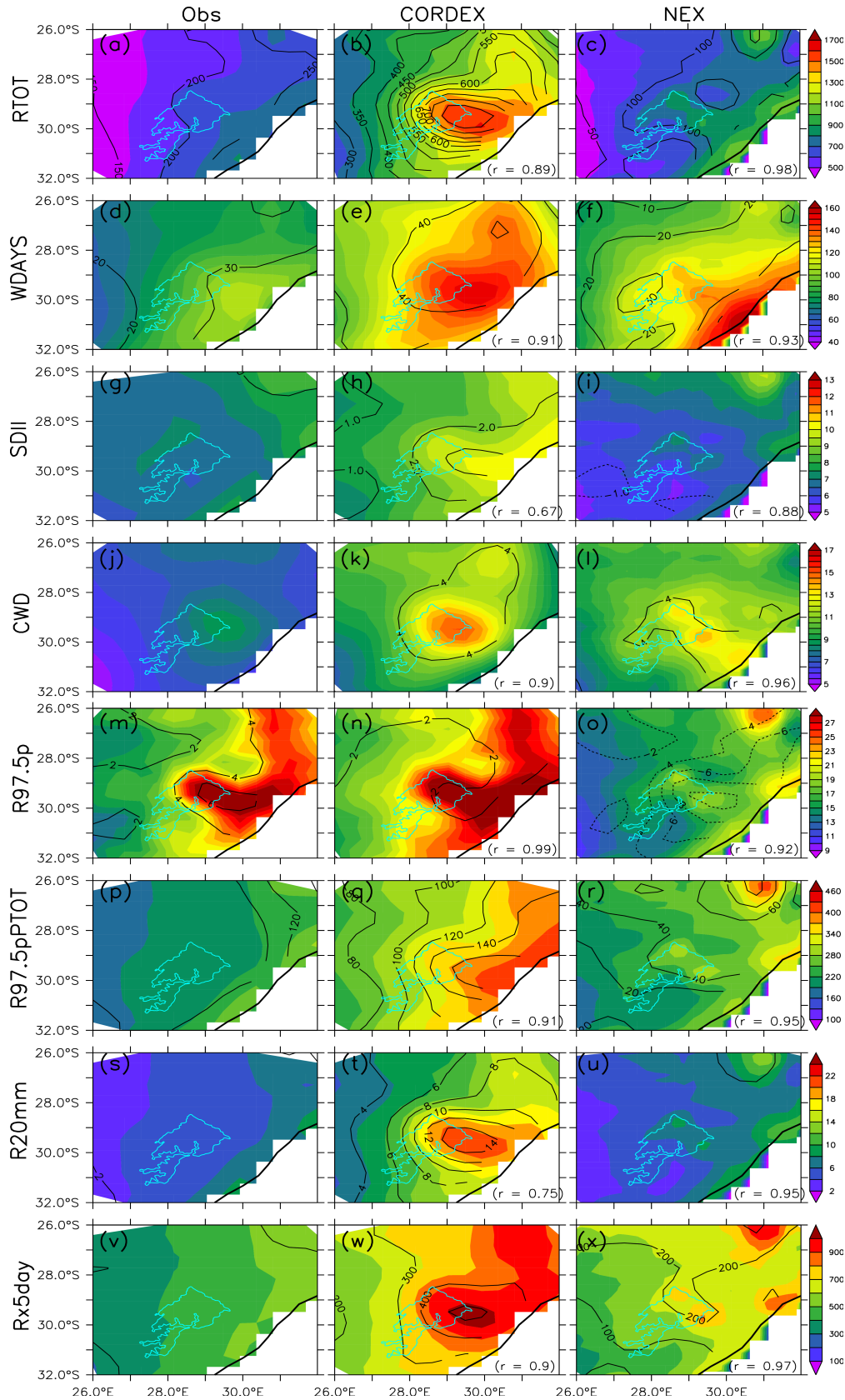


Figure 6.3: Spatial distribution of the precipitation indices over the Drakensberg, as depicted by observation (Obs; the mean of ARC2-FEWS and CHIRPS) and simulation (i.e., ensemble mean from CORDEX and NEX-GDDP) datasets. The difference and correlation between the two observation datasets are indicated with contours and correlation coefficients (r), respectively, in the Obs panels, while the model bias (with reference to Obs) and the correlation between simulation and observation are indicated in the other panels (CORDEX and NEX-GDDP). The precipitation indices are defined in Table 3.3.

6.2 Future Projections over the Drakensberg Mountains

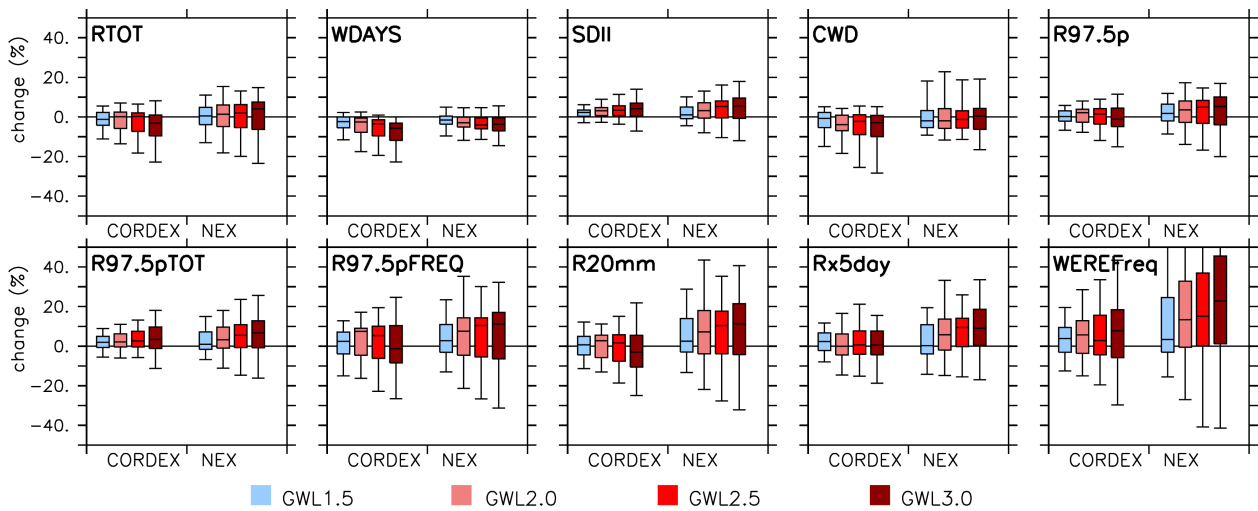


Figure 6.4: Projected changes in extreme precipitation indices over the Drakensberg at various warming levels, as simulated by CORDEX and NEX.

6.2.1 Projected changes in mean rainfall intensity.

There are substantial differences between the CORDEX and NEX projections for RTOT over the DMR; the magnitude of the differences increases with the increase in the GWLs (Figures 6.4 and 6.5). For instance, with regard to the spatial average of the RTOT changes (Figure 6.4), while the majority of the CORDEX simulations project a decrease in RTOT (the median is -2mm year^{-1} at GWL1.5 and -6mm year^{-1} at GWL3.0), the majority of the NEX simulations suggest an increase (the median is 0.5mm year^{-1} at GWL1.5 and 8mm year^{-1} at GWL3.0), although the projections of both datasets are associated with a large uncertainty. In terms of the spatial distribution of the RTOT changes (Figure 6.5), the greatest disagreement between the datasets occurs at high altitude ($> 2000\text{m}$ above sea level), where CORDEX projects a decrease in RTOT (up to 60mm year^{-1} at GWL3.0), while NEX projects an increase (up to 30mm year^{-1} at GWL3.0). At the lower altitudes (i.e., below 2000m above sea level), both datasets project a decrease in RTOT, but the magnitude of the decrease is higher in the CORDEX projection than in the NEX. The discrepancy between CORDEX and NEX with regard to the RTOT projection may be attributed to a number of reasons. It may be due to the differences in the set of GCMs simulations downscaled by the two experiments. While CORDEX downscaled 11 GCMs and NEX downscaled 19 GCMs, the two sets only have 9 GCMs in common. The discrepancy may also be due to how the two downscaling approaches handle climate feedback from local-scale forcing (land-sea boundary, topography, land use and land cover change). Several studies (e.g., Vaittinada Ayar et al., 2016; Hewitson and Crane, 2006) have shown that feedback from these local-scale features can modify (i.e., either amplify or reduce) large-scale climate signals (from GCMs) over an area. While the CORDEX RCMs used parameterized convection and turbulence to represent the local-scale feedback, the NEX Statistical Downscaling Model (SDM) does not have these. Hence, the NEX SDM (which assumes a stationary relationship between GCM output and observation) may preserve the trends in the GCMs simulations, but the CORDEX RCMs may alter the trends because of the local-scale feedback.

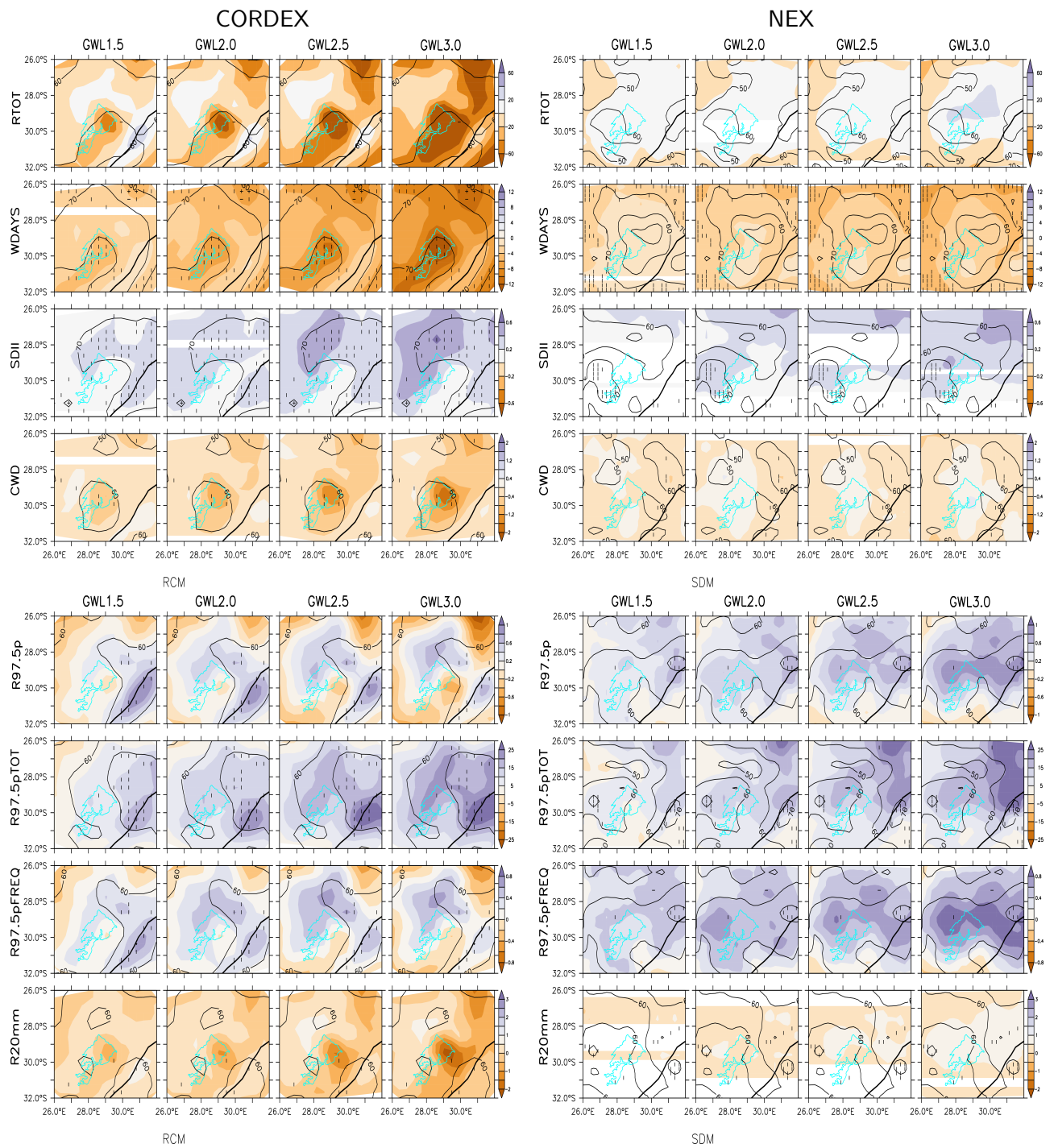


Figure 6.5: CORDEX and NEX projected changes in rainfall indices over Drakensberg at four GWLs (GWL1.5, GWL2.0, GWL2.5 and GWL3.0). The horizontal strip (—) shows where at least 80% of the simulations agree that the projected change is statistically significant (at 99% confidence level) while the vertical strip (|) depicts where at least 80% of the simulations agree on the sign of the changes. The cross (+) denotes where both conditions are satisfied; hence the change is robust.

Despite the disagreement between CORDEX and NEX with regard to the RTOT projections, the two datasets agree on the projected change in WDAY and SDII (Figures 6.4 and 6.5). For instance, the ensemble means of both datasets project a decrease in WDAY and an increase in SDII over the DMR at all GWLs (suggesting fewer but more intense rainfall events in the future). This tendency for fewer but more intense rainfall events may be a regional extension to the Drakensberg area because studies (i.e., Pohl et al., 2017; Abiodun et al., 2019; Thoithi et al., 2021) have projected similar results over most parts of Southern Africa. In addition, both datasets agree that the magnitude of the changes grows as the GWL increases, except that, for WDAY, the growth is faster in CORDEX, and for SDII, the growth is faster in NEX. Furthermore, in both datasets, the level of uncertainty in the WDAY and SDII projections is lower than in the RTOT projection, because more than 70% of the simulations agree with the ensemble mean on the direction of the projected changes in WDAY and SDII. Nevertheless, there are a few differences in the CORDEX and NEX projections for these indices. For example, in the spatial distribution of the WDAY changes (Figure 6.5), the magnitude of the projection is higher in CORDEX than in NEX (especially, in the area located more than 2000m above the sea level). In addition, going by the relationship between three variables (RTOT, WDAY, and SDII), the consequence of RTOT and SDII changes on RTOT changes differ for both datasets. Although NEX suggests that the annual water surplus from the increased SDII may be greater than the annual water deficit from the decreased WDAYs, which would result in an increased RTOT, CORDEX indicates that the annual water excess from the enhanced SDII could be less than the annual water deficit from the lesser WDAYs. Nevertheless, Table 6.2 shows that projected changes in mean rainfall intensity over DMR are lower than the present-day inter-annual variability (i.e., standard deviation).

6.2.2 Projected changes in duration indices.

In both datasets (CORDEX and NEX), most simulations project a decrease in the mean wet spell duration (CWD) over the DMR and indicate that the magnitude of the projection varies non-linearly with the increase in GWLs (Figure 6.4). However, the magnitude of the decrease is generally higher in the CORDEX dataset, where the projection uncertainty is also lower. The spatial distribution of projected changes is like that of RTOT (Figure 6.5). While both datasets agree on a decreased CWD at the mountain base, they disagree on the changes near the mountain top, where CORDEX projects a decrease (> 2 days) and NEX projects a weak increase (< 0.5 day) or no change. This discrepancy, which is consistent with the one in RTOT, may be attributed to how the climate feedbacks from the topography are handled in the datasets. However, the wet spell metric used here needs to be considered with caution because it is very sensitive to threshold effects and is also less realistic under current climate conditions. In addition, the projected changes are lower than the present-day natural variability (Table 6.2).

6.2.3 Projected changes in extreme rainfall indices.

For RTOT (Figure 6.5), the SOM analysis reveals that the spatial distribution of the projected changes can be grouped into three major patterns. The first pattern features a decrease in RTOT (with different magnitude) over the entire DMR domain (i.e. Figure 6.5a 7a: Nodes 3, 4, 7, 8, 11 and 12 in). This most frequent pattern accounts for about 47% of the total RTOT projections (i.e. 50% in CORDEX and 43% in NEX). This implies that while the ensemble mean of NEX projections indicates an increase in RTOT over the domain, 43% of the projections actually indicate a decrease in RTOT over the domain. The second pattern shows an increase in RTOT (with different magnitude) over most part DMR domain (i.e. Figure 6.5: Nodes 5, 6, 9 and 10), accounting for 46% of the total RTOT projections (i.e. 36% in CORDEX and 57% in NEX). This also implies that while the ensemble mean of CORDEX projections

Table 6.2: The simulated mean and standard deviation (σ) of rainfall indices over DMR during the present-day and the projected changes under various global warming as depicted by ensemble mean of CORDEX and NEX(*in italics*). All the values are averaged over DMR.

Rainfall Index	Present-day		Changes under Global Warming Levels			
	Mean	σ	GWL15	GWL20	GWL25	GWL30
WDAYS (days $year^{-1}$)	123.5	13.3	-3.0	-4.6	-6.1	-8.5
	<i>107.2</i>	<i>12.5</i>	<i>-1.7</i>	<i>-2.8</i>	<i>-3.5</i>	<i>-4.1</i>
RTOT (mm $year^{-1}$)	1097.0	190.2	-8.6	-14.9	-25.0	-43.8
	<i>680.6</i>	<i>139.9</i>	<i>2.5</i>	<i>3.5</i>	<i>2.3</i>	<i>3.5</i>
SDII (mm day^{-1})	8.7	1.1	0.2	0.2	0.3	0.3
	<i>6.4</i>	<i>1.0</i>	<i>0.1</i>	<i>0.2</i>	<i>0.3</i>	<i>0.3</i>
Rx5day (mm)	759.3	359.7	15.7	4.8	13.8	11.6
	<i>590.4</i>	<i>282.1</i>	<i>18.8</i>	<i>33.2</i>	<i>40.1</i>	<i>54.1</i>
R97.5p (mm day^{-1})	22.4	4.7	0.1	0.2	0.1	0.0
	<i>15.7</i>	<i>3.9</i>	<i>0.3</i>	<i>0.4</i>	<i>0.4</i>	<i>0.5</i>
R97.5pTOT (mm $year^{-1}$)	320.4	136.4	6.8	9.9	12.1	14.7
	<i>244.1</i>	<i>108.9</i>	<i>6.5</i>	<i>10.4</i>	<i>12.6</i>	<i>14.7</i>
R20DAYS (days $year^{-1}$)	12.5	3.9	0.0	0.0	-0.1	-0.3
	<i>5.9</i>	<i>2.7</i>	<i>0.3</i>	<i>0.4</i>	<i>0.4</i>	<i>0.5</i>
R97.5pFREQ (days $year^{-1}$)	9.1	3.5	0.1	0.2	0.2	0.1
	<i>9.1</i>	<i>3.6</i>	<i>0.4</i>	<i>0.4</i>	<i>0.4</i>	<i>0.5</i>
WEREFreq (days $year^{-1}$)	20.5	NA	0.7	1.0	1.2	1.3
	<i>5.7</i>	<i>NA</i>	<i>0.6</i>	<i>0.9</i>	<i>1.0</i>	<i>1.3</i>
CWD (day $year^{-1}$)	10.7	3.2	-0.2	-0.3	-0.4	-0.5
	<i>10.4</i>	<i>3.3</i>	<i>-0.1</i>	<i>0.0</i>	<i>-0.1</i>	<i>-0.1</i>

indicates a decrease in RTOT over the domain (Figure 6.5), 36% of them suggest an decrease in RTOT over most part of the domain. The third pattern is characterized by a band decrease in RTOT over the mountain top and along the coast but an increase RTOT elsewhere (Figure 6.5:Nodes 1 and 2). The pattern, which only accounts for about 7.2% of the total RTOT projections (14% in CORDEX) does not feature in NEX simulations.

There is a good agreement between the CORDEX and NEX datasets with regard to the projected changes in the characteristics of extreme rainfall events over the DMR (Figure 6.5). In both datasets, most simulations project an increase in mean extreme rainfall intensity (RA97.5p, RA97.5pTOT and Rx5days) and frequency (RA97.5pFREQ, R20mm and WEREFreq) over the DMR, showing that the magnitude of the increase generally grows with an increase in the GWLs (Figure 6.5). For instance, with NEX, the median of the projected increase jumps from 1% (at GWL1.5) to 8% (at GWL3.0) in R95pTOT, from 2% (at GWL1.5) to 11% (at GWL3.0) in RA97.5pFREQ, and from 2% (at GWL1.5) to 22% (at GWL3.0) in WEREFreq. Both datasets also agree that, at GWL3.0, the percentage increase in WEREFreq may be more than RA97.5pFREQ, suggesting that the future extreme rainfall event may be more from organized or mesoscale convective systems (MCS). However, given that the resolution of both datasets is too coarse to resolve MCS, further studies with higher resolution datasets are needed to investigate this further. The agreement between the datasets also features in the spatial distribution of the extreme precipitation indices (RA97.5p, RA97.5pTOT, RA97.5pFREQ and R20mm) (Figure 6.5). For instance, in some indices (e.g. RA97.5p, RA97.5pTOT, and RA97.5pFREQ), both datasets feature a region of increase that extends from the Indian Ocean to the mountain top and that is surrounded by an area of decrease. However, the area of increase is wider in NEX than in CORDEX. The link between the increase of extreme rainfall activities over the Indian Ocean and the mountain top suggests a transport of warmer and moisture laden (i.e., more buoyant) air from the Indian Ocean to the mountain top in the future. This is consistent with the findings from previous studies that linked precipitation over the DMR to moisture transport from the Indian Ocean (Tyson et al., 1976; Ndarana et al., 2021). For instance, Tyson et al. (1976) shows that the northeast part of the gradient winds around the Indian Ocean high advect moisture-laden air over the Drakensberg.

6.2.4 Scaling of extreme precipitation changes.

To present the results in the light of ongoing discussion in climate communities on how well precipitation extreme changes in a warming climate scale with Clausius-Clapeyron (CC) relationship (Allen and Ingram, 2002; Drobinski et al., 2018; Schröder and Kirchengast, 2018), Figure 6.6 presents the scaling of extreme precipitation (R97.5p) changes with the regional temperature changes at various warming levels in comparison with the CC theoretical values (about $6.2\% K^{-1}$ over DMR). For both CORDEX and NEX, the figure shows that there is a large discrepancy among the simulations on the scaling. While some simulations suggest a higher scaling than the CC (i.e., super-CC scaling), some show a lower scaling (sub-CC scaling), and others feature a negative scaling (Figure 6.6). However, the ensemble means of both datasets agree on a sub-CC scaling over DMR, with the maximum scaling ($0.2 \times CC$) featuring over the eastern coast and the mountain's top. The projected sub-CC scaling of extreme precipitation changes over the DMR can be attributed to number of factors. Firstly, the projection assumes a constant relative humidity with the warming. Meanwhile, the changes in moisture availability may not increase as fast temperature, leading to a decrease in relative humidity. The possibly explains why the magnitude of the scaling drops as the warming level increases (Figure 6.6). Using the dew point temperature (T_d , which is the temperature to which an air parcel must be cooled to reach saturation) instead of temperature may give a more reliable the scaling, because T_d is a measure of specific humidity translated to temperature using the CC relationship. Kendon et al. (2019) reported a

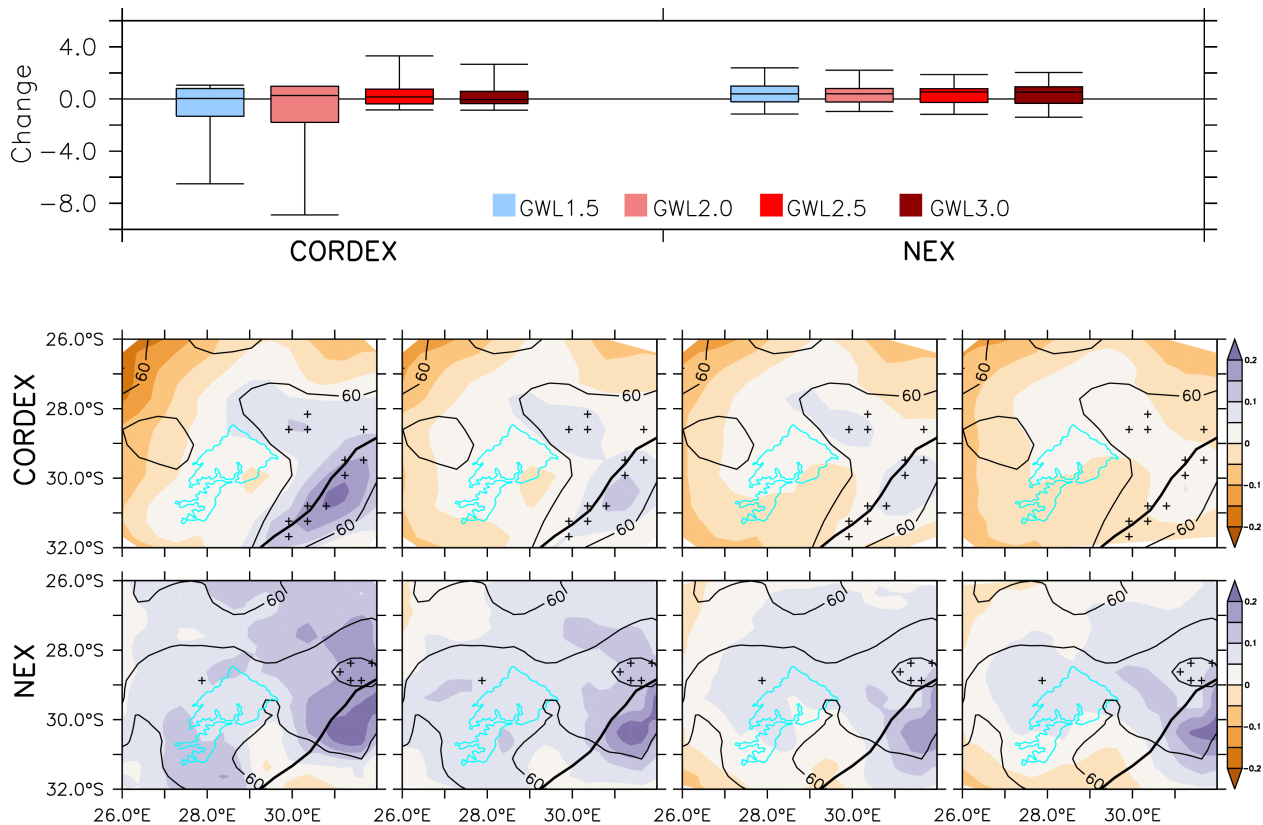


Figure 6.6: Scaling between future changes in extreme rainfall-temperature and the temperature over DMR at various global warming levels as depicted by CORDEX and NEX datasets. The scaling coefficient is obtained as the future changes in logarithm of extreme precipitation intensity divided by future changes in mean temperature and has been normalized by the theoretical Clausius–Clapeyron relationship (about $6.0 - 6.2\% K^{-1}$ over DMR); Hence a value of 1 corresponds to Clausius–Clapeyron scaling. The upper shows the simulation spread of the scaling averaged over DMR while the last two rows show the spatial distribution from the ensemble mean. In the spatial distribution plots, the cross (+) indicates where at least 80% of the simulations agree on the sign of the changes.

super-CC scaling over most part of Africa (especially over DMR) when used Td for the scaling and but a sub-CC scaling when used temperature. Secondly, the projection also assumes that storm dynamics do not change with the warming. However, the environment in which the storms develop may change, altering characteristics (e.g., direction and vertical vertical) of air that feeds the storm. Lastly, the convection parameterization schemes used in RCM and the empirical equations used in the SDM could also influence the scaling. Kendon et al. (2019) found higher scaling in convection-permitting simulation than in convection-parameterized simulations.

6.3 The SOM classification of the future projections

To reveal spatial patterns of the projection that might be hidden in the ensemble mean projections, this section discusses the SOM classification (4x3 nodes) of the CORDEX and NEX projection over Drakensberg, focusing on the projected changes in the annual rainfall (RTOT, Figure 6.7), extreme rainfall intensity (R97.5p, Figure 6.8) and extreme rainfall frequency (R97.5pFREQ, Figure 6.9). The

goal is to identify the most distinct or major patterns in these projected changes in these indices and examine how they differ from the ensemble mean patterns in Figure 6.5. Note that for any SOM classification, the most distinct patterns are usually the four edge nodes (i.e. Nodes 1, 4, 9 and 12).

For RTOT (Figure 6.7), the SOM analysis reveals that the spatial distribution of the projected changes can be grouped into three major patterns. The first pattern features a decrease in RTOT (with different magnitude) over the entire DMR domain (i.e., Figure 8a: Nodes 3, 4, 7, 8, 11 and 12). This most frequent pattern accounts for about 47% of the total RTOT projections (i.e., 50% in CORDEX and 43% in NEX). This implies that, while the ensemble mean of the NEX projections indicates an increase in RTOT over the domain, 43% of the projections actually indicate a decrease in RTOT over the domain. The second pattern shows an increase in RTOT (with different magnitude) over most parts of the DMR domain (i.e., Figure 6.7: Nodes 5, 6, 9 and 10), accounting for 46% of the total RTOT projections (i.e., 36% in CORDEX and 57% in NEX). This also implies that, while the ensemble mean of the CORDEX projections indicates a decrease in RTOT over the domain (Figure 6), 36% of them suggest a decrease in RTOT over most parts of the domain. The third pattern is characterized by a band decrease in RTOT over the mountain top and along the coast, but an increase in RTOT elsewhere (Figure 6.7: Nodes 1 and 2). This pattern, which only accounts for about 7.2% of the total RTOT projections (14% in CORDEX), does not feature in the NEX simulations.

The SOM classification of the projected changes in R97.5p (Figure 9) can be generally grouped into two patterns. The first pattern features an increase in R97.5p over most parts of the DMR (i.e., Nodes 1, 2, 5, 11, 9 and 10) and accounts for 54% of the total R97.5p projections (50% in CORDEX and 58% in NEX). In contrast, the second pattern shows a decrease in R97.5p over most parts of the DMR (Nodes 3, 4, 7, 8, 11 and 12). While this pattern accounts for 46% of the total R97.5p projections (50% in CORDEX and 58% in NEX), it does not reflect in the ensemble mean projections for both NEX and CORDEX. The pattern of the SOM classification for R97.5pFREQ projections (Figure 6.9) is similar to the pattern of R97.5p, and in most cases the simulations that projected an increase in R97.5p over most parts of the DMR also produce an increase in R97.5pFREQ over most parts of the DMR, while those that projected a decrease in R97.5p also produce a decrease in R97.5pFREQ over the domain.

The SOMs results can guide climate modelling communities in selecting a fewer but meaningful set of GCMs for downscaling (dynamical, statistical and hybrid) and climate impact studies, with aim capturing the ensemble mean projection as well as diversity in the projected changes using a subset of the GCMs. For example, Table 6.3 shows ranking the GCMs based on their contributions to the diverse patterns of changes in RTOT and R97.5p in the SOMs results. The table shows that NorESM1-M^(x) has the highest ranking because it features all the extreme patterns of RTOT patterns (i.e., Dipole, Wetter, and Drier) and of R97.5p (i.e., Stronger and Wetter). It should be noted that the ranking might be bias because all the simulations we not downscaled by the same number of downscaling models (see Table 6.1). However, the ranking shows that downscaling NorESM1-M^(x) simulation features a more diverse pattern (i.e., larger uncertainty) than downscaling HadGEM2-ES⁽ⁿ⁾ (for example). Previous studies (Mizuta et al., 2014; Monerie et al., 2017) have employed similar approach (cluster analysis) to group GCMs based model bias historical climate simulations as well as future changes temperature, precipitation, and sea surface temperature. These studies also alluded to the usefulness of the raking/grouping in situations for which it is not possible to downscale or use a large ensemble of models for impact studies. Table 6.4 summarizes the projected changes in precipitation over the Drakensberg and the potential impacts of these changes as well as some suggested adaptation strategies.

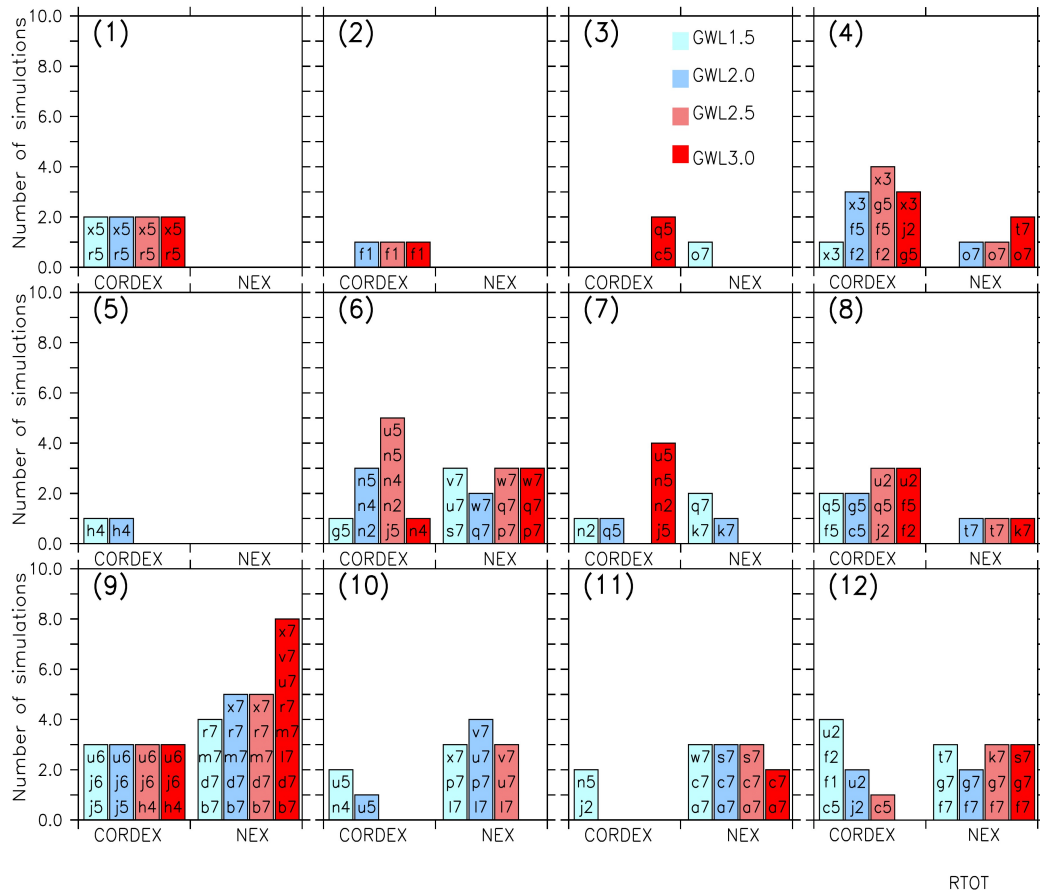
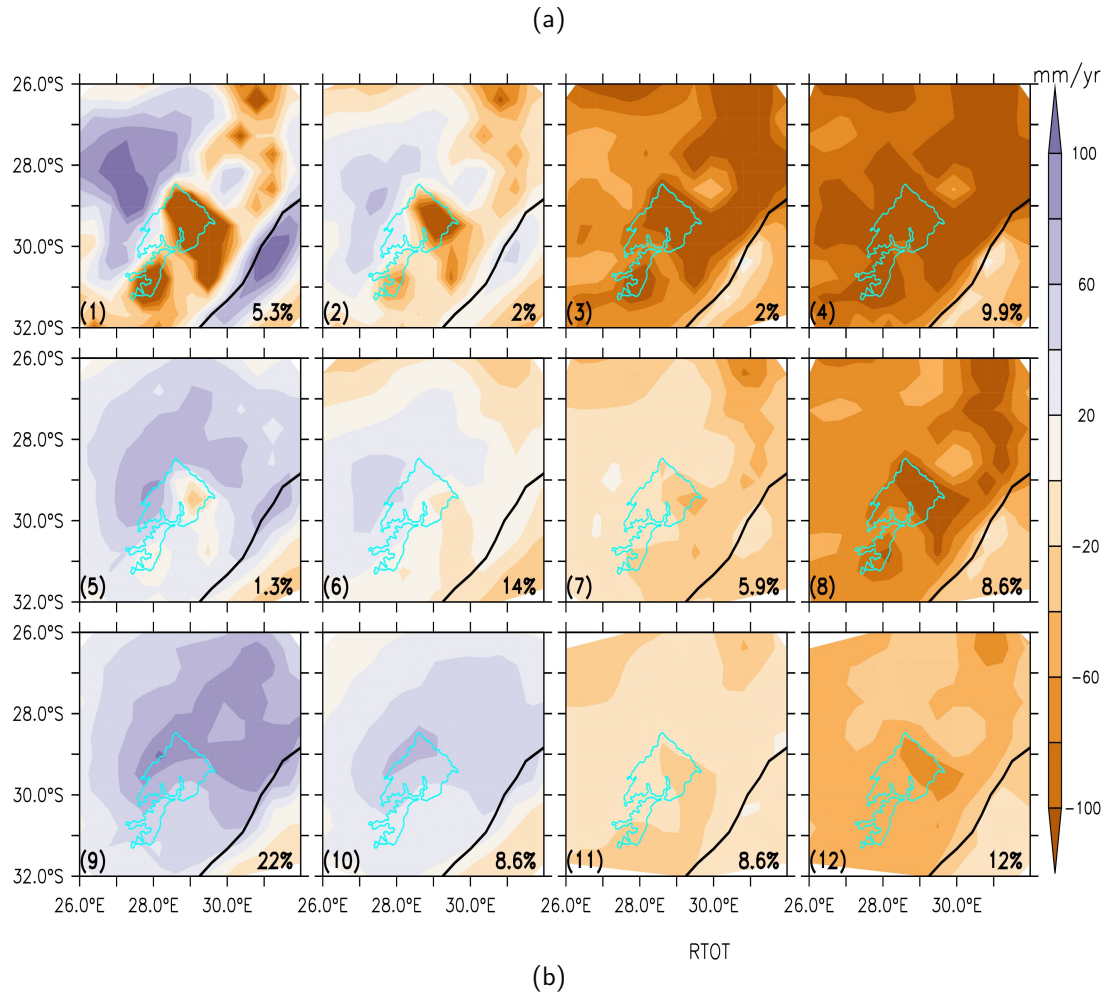


Figure 6.7: SOMs classification of projected changes in annual rainfall (RTOT) over DMR; (a) SOMs nodes and (b) contribution of CORDEX and NEX to the SOMs nodes at various GWLs.

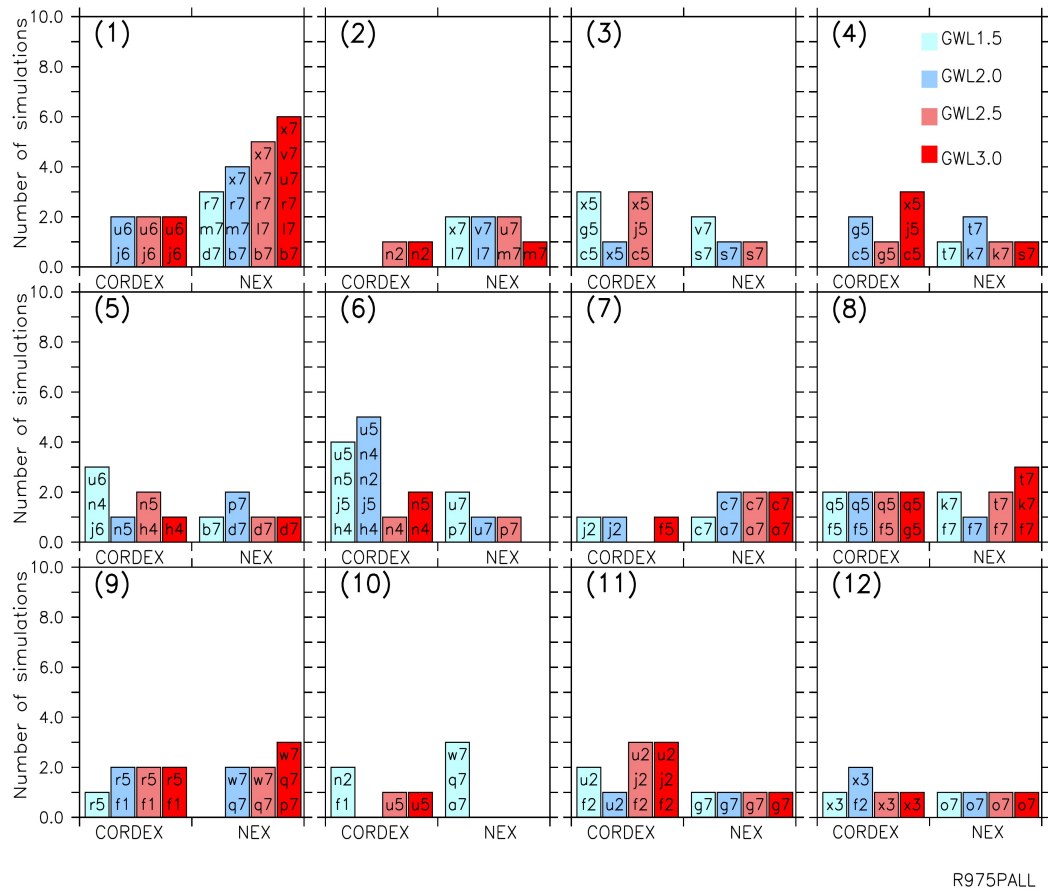
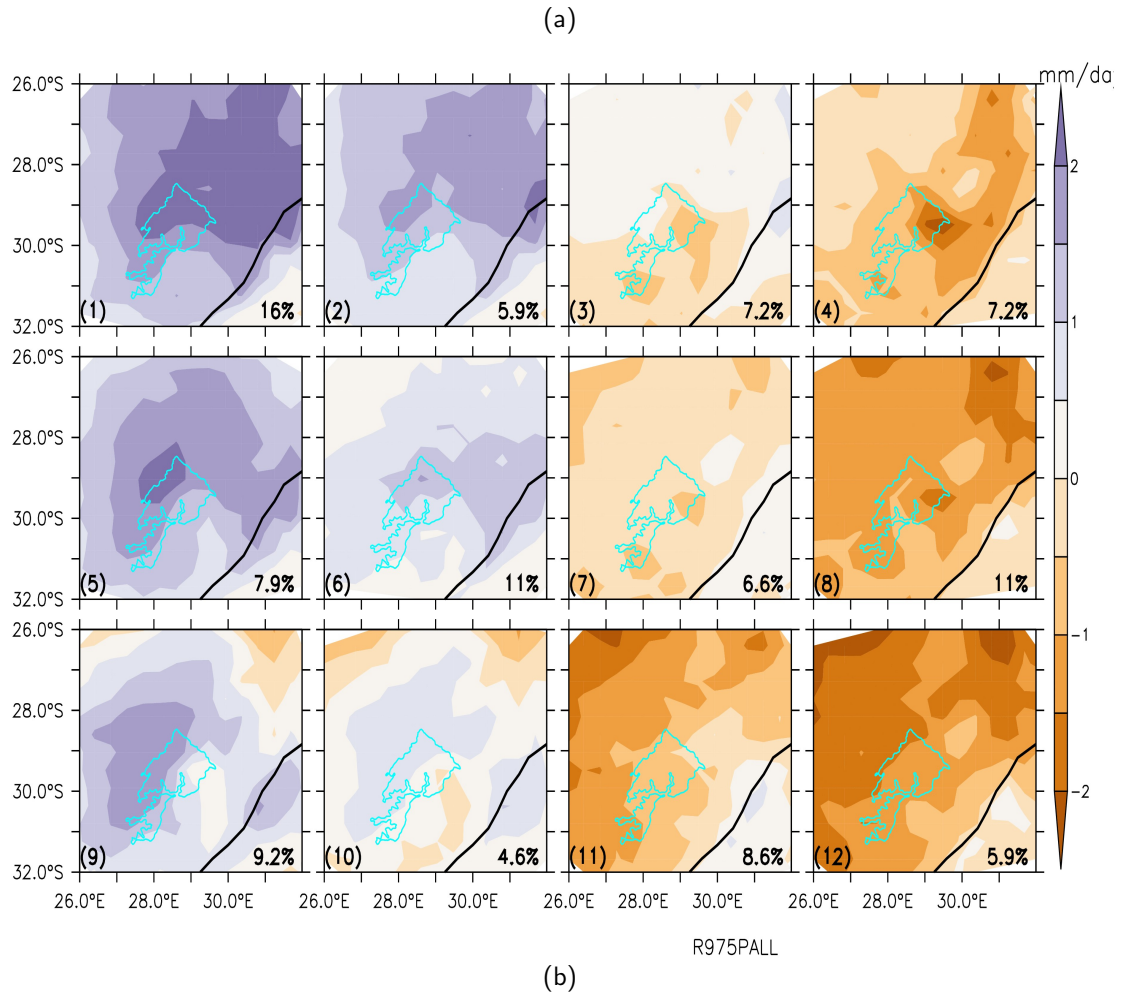


Figure 6.8: Same as for Figure 6.7 but for R97.5p.

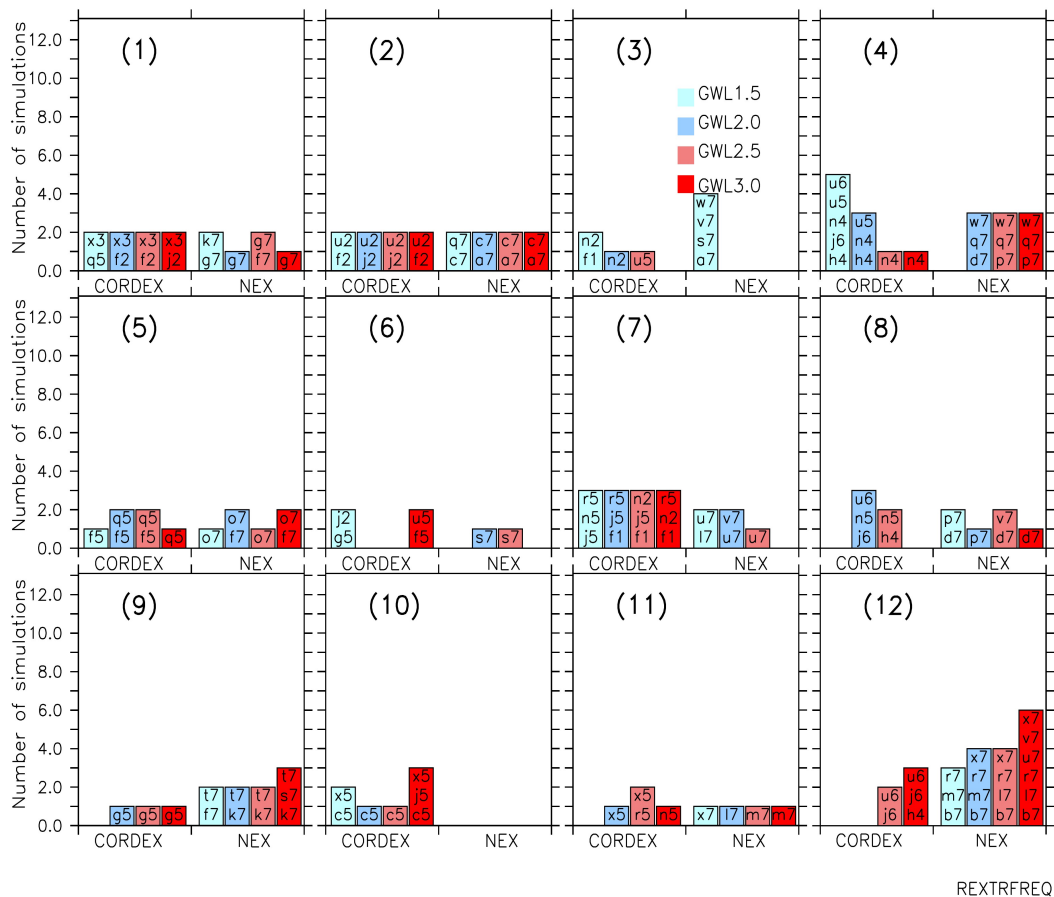
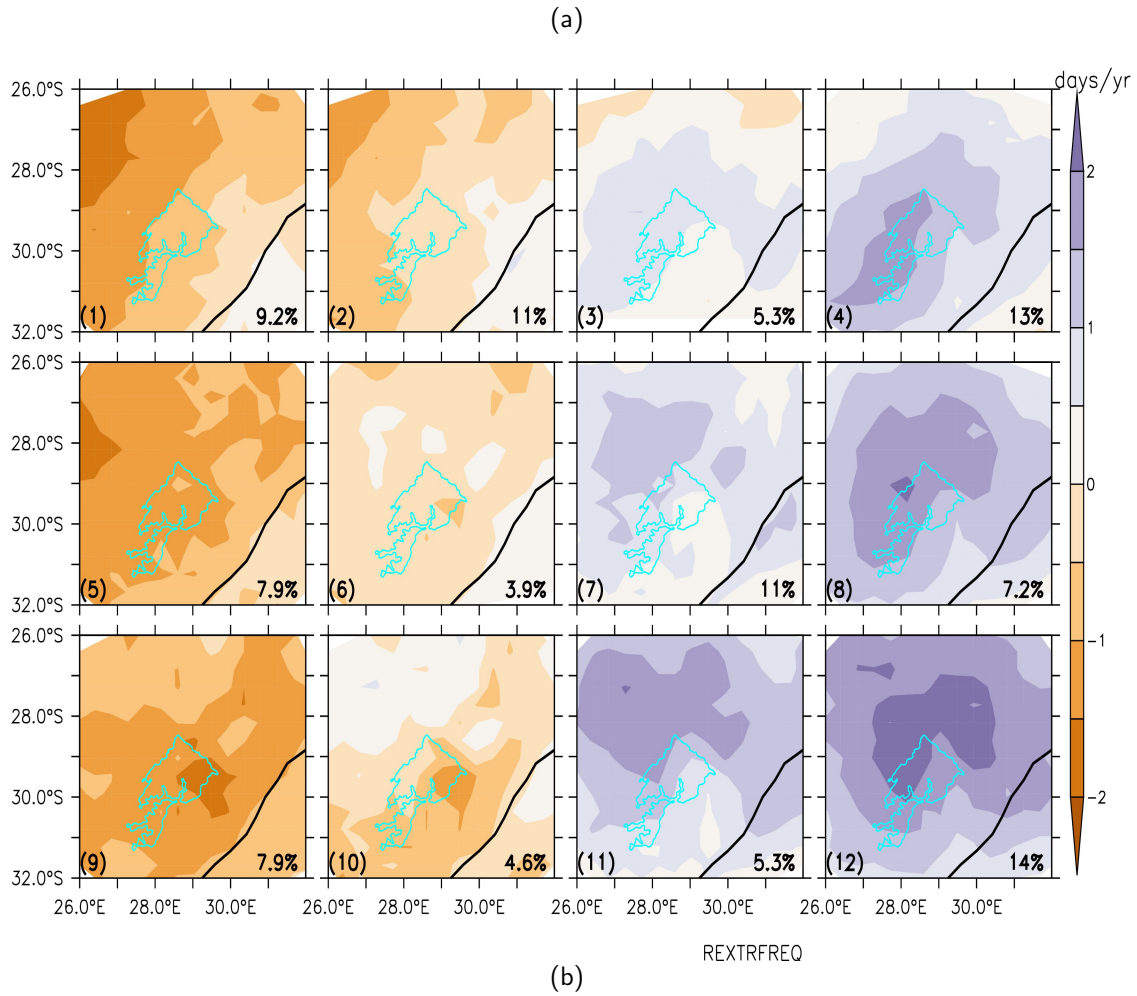


Figure 6.9: Same as for Figure 6.7 but for REXTRFREQ.

Table 6.3: Ranking of GCM simulations for downscaling over DMR based on their contribution to the SOMs classification of projected changes in RTOT and R97.5p patterns. The RTOT patterns used for the ranking are Dipole (Nodes 1, 2 and 5), Wetter (Nodes 9 and 10) and Drier (Nodes 3, 4 and 8) patterns in Figure 6.7 while that of R97.5p patterns are Stronger (Nodes 1, 2, and 5) and Weaker (Nodes 8, 11, 12) patterns in Figure 6.8. The pattern to which each simulation contributes is ticked (✓).

GCMs	RTOT patterns			R97.5p patterns		Rank
	Dipole	Wetter	Drier	Stronger	Weaker	
NorESM1-M ^(x)	✓	✓	✓	✓	✓	1
EC-EARTH-r12 ^(j)		✓	✓	✓	✓	2
MPI-ESM-LR ^(u)		✓	✓	✓	✓	2
CNRM-CM5 ^(f)	✓		✓		✓	3
EC-EARTH-r1 ^(h)	✓	✓		✓		3
MIROC5 ^(r)	✓	✓		✓		3
BNU-ESM ^(b)		✓		✓		4
CCSM4 ^(d)		✓		✓		4
CSIRO-Mk3-6 ^(g)			✓		✓	4
GFDL-CM3 ^(k)			✓		✓	4
GFDL-ESM2G ^(l)		✓		✓		4
GFDL-ESM2M ^(m)		✓		✓		4
HadGEM2-ES ⁽ⁿ⁾		✓		✓		4
INMCM4 ^(o)			✓		✓	4
IPSL-CM5A-LR ^(p)		✓		✓		4
IPSL-CM5A-MR ^(q)			✓		✓	4
MIROC-ESM5 ^(s)			✓		✓	4
MPI-ESM-MR ^(v)		✓		✓		4
CanESM2 ^(c)			✓			5
CESM1-BGC ^(e)						6
MIROC-ESM-CHEM ^(t)						6
MRI-CGCM3 ^(w)						6

Table 6.4: Projected changes in precipitation over the Drakensberg and its potential impacts and suggested adaptation strategies.

Projection	Potential impacts	Adaptation Strategies
Increase in both annual rainfall and extreme rainfall events.	<ul style="list-style-type: none"> • Increased risk of floods, landslides, geotechnical and hydrologic hazards. • Degradation of ecological services, which may involve risks to lives, livelihoods and lifestyles. 	<ul style="list-style-type: none"> • Financing the relocation of citizens at risk. • Diversification of livelihood. • Disaster relief fund. • Policy making. • Structural flood protection measures, such as dikes and levees. • Flood early warning systems. • Risk-informed land planning. • Financing the repair of and recovery from flood damages. • Development of flood map. • Development of emergency response plans.
Decrease in both annual rainfall and extreme rainfall events.	<ul style="list-style-type: none"> • Increase in droughts. • Reduction in food production and famine. • Reduction in dam levels and hence hydro-electric power generation. • Crop destruction. 	<ul style="list-style-type: none"> • Education of citizens. • Changes to crop types. • Provision of crop insurance. • Alternative means of power generation, such as solar and wind energy. • Design of an agriculture-based adaptation strategy in terms of policy. • Increased access of farmers to information, training, knowledge networks. • Social organizations to provide opportunities to enhance resilience and adaptive capacity. • Diversification of options for water supply and expansion of current sources, e.g., desalination. • Increased water storage capacity of dams by raising the dam levels.
Decrease in annual rainfall, but increase in extreme rainfall events.	<ul style="list-style-type: none"> • Increase in droughts, floods, landslides, geotechnical and hydrologic hazards. • Degradation of ecological services, which may involve risks to lives, livelihoods and lifestyles. 	<ul style="list-style-type: none"> • Modelling of climate change risk. • Development of models to understand potential water quality changes. • Monitoring of surface water conditions. • Development of emergency response plans.

6.4 Summary

In this study, we investigated the projected changes in the characteristics of rainfall indices over the Drakensberg Mountains at four different GWLs (1.5°C , 2.0°C , 2.5°C and 3.0°C) under the RCP8.5 scenario. We compared statistical (NEX) and dynamical (CORDEX) downscaled projections of the CMIP5 GCMs. To investigate the capability of the two downscaled products to capture the observed characteristics of the rainfall indices over the DMR, we compared their biases in historical simulation of the past climate with observation uncertainties based on eight observation datasets (ARC, CHIRPS, PERSIANN, TAMSAT, AgCFSR, AgMERRA, WFDEI-CRU and WFDEI-GPCC). The model ensemble spatial means were compared using box plots, whereas the projected change in the spatial distribution of rainfall indices was compared using SOMs. The results of the study can be summarized as follows:

- The eight observation datasets agree on the characteristics of precipitation (intensity-frequency curves and precipitation indices) over the DMR, albeit with some discrepancies.
- The CORDEX and NEX datasets give a realistic simulation of precipitation characteristics over the DMR and, in most cases, their biases lie within the observation uncertainty.
- NEX performs better than CORDEX in reproducing most of the precipitation characteristics (e.g. intensity-frequency curves, RTOT, WDAY, SDII), but CORDEX performs better than NEX in simulating the threshold of extreme rainfall (R97.5p).
- The ensemble means of both datasets agree on a future increase of SDII, RA97.5p, RA97.5pTOT, RA97.5pFREQ and WEREFreq, and on a decrease of WDAY and CWD, but they disagree on the projected changes of RTOT, for which CORDEX projects an increase over most parts of the domain, while NEX indicates a decrease.
- The SOM analysis, which reveals projected patterns that are visible in the ensemble mean results, shows the four most important projections with a combination of annual rainfall and extreme precipitation events (intensity and frequency): (i) increase in both annual precipitation and extreme precipitation events; (ii) decrease in both annual precipitation and extreme precipitation events; (iii) increase in annual precipitation but decrease in extreme precipitation events; and (iv) decrease in annual precipitation but increase in extreme precipitation events.

The adaptation strategies presented in Table 6.4 may either be applicable to the communities living directly on the Drakensberg mountains or to remote low land communities which depend on the mountain. For example, the Drakensberg is a major water tower for South Africa and Lesotho. This means that decrease in both annual rainfall and extreme rainfall events may potentially lead to reduction in dam levels and hence Hydro-electric power generation as listed in Table 6.4. This can potentially affect both the communities living on the Drakenberg and the low land communities. Therefore, for adaptation strategy, both communities will need to consider diversifying electric power generation or moving to alternative means of power generation such as solar and wind energy as listed in the adaptation strategy column in Table 6.4.

Some studies (Mukwada et al., 2016; Mutana and Mukwada, 2020) have noted that the Drakenberg communities are poor and exposed to poor living conditions characterized by undernourishment and a lack of adequate shelter and potable water. That is, they are generally disadvantaged and prone to challenges associated with food insecurity, material poverty, and other forms of deprivation. Therefore, citizen education as an adaptation strategy could help community members diversify their income sources or learn new means of earning income by getting involved in sectors like tourism (Mutana and Mukwada, 2020).

Studies such as [Adelabu et al. \(2020\)](#) and ([Mukwada et al., 2021](#)) have reported that agriculture is a common activity in the Drakensberg. Commercial farming involves the cultivation of coffee, tea, citrus, mangoes, papayas (pawpaw), avocados, bananas, litchis and forestry in high rainfall areas of the Drakensberg and Soutpansberg Mountains ([Mukwada et al., 2021](#)). This means that reduction in food production (food security) and famine as a result of decrease in both annual rainfall and extreme rainfall events may have severe consequences on the Drakensberg communities. Therefore, adaptation strategies like provision of crop insurance is very relevant for commercial farmers in the region. Other relevant adaptation strategies include increased access of farmers to information, training, knowledge networks, design of an agriculture-based adaptation strategy in terms of policy and social organizations to provide opportunities to enhance resilience and adaptive capacity as listed in Table 6.4. It is out of the scope of this study to elaborate on each adaptation strategy listed in Table 6.4 nor provide implementation details.

CHAPTER 7

Conclusions and Recommendations

7.1 Conclusions

This dissertation has examined the characteristics of rainfall distribution over the Drakensberg, with the main objectives of investigating the characteristics of rainfall distribution under weak synoptic conditions over the Drakensberg, the capability of two climate models in simulating the characteristic of rainfall over the Drakensberg, and the potential impacts of climate change on the characteristics of precipitation over the Drakensberg at various global warming levels. The thesis used a combination of observation, reanalysis, and climate simulation data to achieve the objectives. The observation data are from eight satellite precipitation products (Section 3.2.1), while the reanalysis data are from Climate Forecast System Reanalysis (CFSR, Section 3.2.2), and the model simulation is from two international multi-model downscaling experiments (i.e. CORDEX and NEX Section 3.2.3) and simulation experiments performed locally with two climate models (WRF and MPAS; Section 3.2.3).

Several definitions and methods have been used to analyse the datasets to achieve the objectives. A weak synoptic day (WSD) over the Drakensberg was defined as a day in which the average synoptic wind speed (at $850hPa$) is less or equal to $7ms^{-1}$ while a wet WSD was identified as WSD with at least $1mm$ rainfall. The characteristics of rainfall and extreme rainfall (including widespread extreme rainfall events, WERE) over the Drakensberg Mountains were quantified using various indices that have been well tested and documented in the literature. The performance of the reanalysis and climate model in simulating rainfall and rainfall extremes was quantified with standard statistical metrics. The major synoptic atmospheric features over Southern Africa, rainfall distribution during WSD over the Drakensberg, and major patterns of WERE over the mountain were obtained using the Self-Organizing Map technique. The future impacts of climate change on rainfall indices were projected at various global warming levels under the RCP8.5 (i.e., high-emission, business-as-usual) scenario. The results of the three studies conducted are reported in three chapters (Chapters 4–6).

In Chapter 4, the thesis found that WSD over the Drakensberg can occur in any season but it is most prevalent in MAM and JJA when it accounts for 20% and 16% of the days in the seasons (respectively). The WSDs are induced by a high-pressure system or the ridging of the South Atlantic High Pressure or South Indian Anticyclone over the mountain. The wet WSDs can feature heavy precipitation over the whole study domain, weak precipitation over the Domain, moderate precipitation over the southwest part, and moderate precipitation over the North-East part. The transport of moisture from the South West Indian Ocean into Southern Africa is the main source of moisture for the WSD rainfall, but the magnitude of the rainfall depends on the modulation of the moisture transport by the orientation of Indian Ocean Highs and the continental trough. The CFSR dataset underestimates the frequency of wet WSDs and the magnitude of the associated rainfall, but the downscaling of the dataset with WRF improves the quality of the simulated rainfall.

In Chapter 5, the thesis showed that WRF and MPAS simulations give a realistic simulation of the

precipitation characteristics over Southern Africa, especially over South Africa and the Drakensberg Mountains. MPAS performs better than the WRF aspect while WRF performs better than MPAS in others. The model results agree with observation and reanalysis datasets that WERE over the Drakensberg mostly occurs in three seasons (DJF, MAM, and SON) and does not occur every year. The hot spot of the events can be on the eastern side of the mountain (stretching from north-east to the south-west along the coastline), or over the north and northeast slope, or over the southern slope, or over the north-western slope of the mountain. However, the most widespread WERE is the one with the maximum rainfall at the eastern side of the mountain. This event is usually associated with tropical temperate troughs, cold fronts, and ridging highs.

In Chapter 6, the thesis found that the two international downscaling experiment datasets (CORDEX and NEX) give reliable simulation of rainfall and extreme precipitation over the Drakensberg. In most cases, the biases in the datasets lie within the uncertainty in the observation. Nevertheless, NEX performs better than CORDEX in reproducing some rainfall and extreme rainfall characteristics and the reverse is the case in other characteristics. Both datasets project an increase in simple rainfall and extreme rainfall intensity and a decrease in the number of wet days and number of continuous wet days over the Drakensberg in the future. The classification of the future projection from the datasets suggests four possible scenarios for future changes in rainfall and extreme rainfall events, namely: (i) increase in both annual precipitation and extreme precipitation events; (2) decrease in both annual precipitation and extreme precipitation events; (3) increase in annual precipitation but decrease in extreme precipitation events; and (4) decrease in annual precipitation but increase in extreme precipitation events.

The results of the thesis can have application in understanding and predicting the characteristics of precipitation over the Drakensberg. Previous studies (Nel and Sumner, 2005; Nel, 2008; Schulze, 1979) have discussed the distribution of the annual precipitation over the mountain but the present study has extended the discussion by focusing on rainfall distribution on WSDs and provided information that can improve rainfall prediction over the mountain. The identification of the atmospheric systems that induce weak synoptic conditions over Drakenberg and the classification of the associated rainfall patterns could guide operational weather forecasters in predicting rainfall distribution on WSDs. The study showed that the WSD rainfall over the Drakensberg could be more than 13mm day^{-1} , especially over the north-eastern part of the mountain. Most weather prediction centers in Africa rely on information from global forecast products like the Global Forecasting System (used in producing CSFS). The present study shows the extent to which the products can underestimate WSD rainfall and the extent to which the dynamical downscaling with regional climate models (like WRF) can improve the predicted rainfall. This has implications for the usage of weather and climate information for hydrological and agricultural studies or modelling over the Drakensberg.

These results have also improved knowledge of the characteristics of widespread extreme rainfall events over the Drakensberg and the dynamics of moisture transport that sustains the events. In agreement with previous studies (i.e., Omar and Abiodun, 2017; Mpungose et al., 2022; Ndarana et al., 2018) this study identified the Indian Ocean as the main source of widespread extreme events over the Drakensberg area and highlighted the important role played by ridging highs in transporting moisture to the mountain rain. More importantly, it has identified hotspots and the spatial coverage of widespread extreme rainfall events of the Drakensberg. This information is valuable for improving the prediction of extreme rainfall events over the Drakensberg, as well as for planning and mitigating the impacts. For instance, the identification of WERE hotspots around the Drakensberg could help in the development and implementation of structural and non-structural mitigation strategies to protect against extreme rainfall damage in the hotspot areas. Structural strategies consist in using engineered systems like floodwalls, dams, and levees to control the hazards whereas non-structural mitigation strategies include education and measures

like public policy planning programs, such as zoning, buyout, land-use regulation, and socioeconomic incentives (Hemmati et al., 2022).

The results can also provide a basis for developing climate change adaptation and mitigation strategies over the Drakensberg. For example, the projected increase in extreme precipitation events over the Drakensberg suggests an increased future risk of floods and geotechnical hazards. Hunter et al. (2016) reported that an extreme rainfall event over the Main Ranges of the Canadian Rocky Mountains and over the Bow River watershed (Canada) in June 2013 produced flooding that led to geotechnical and hydrologic hazards. The occurrence of such geotechnical hazards over the Drakensberg may be detrimental to the lives and socio-economic activities of the communities at the foot of the Drakensberg. The projected decrease in annual precipitation may furthermore lead to a future increase in droughts in the Drakensberg. Droughts in this area may encourage forest and bush fires and could have severe implications for water resources and disaster management. It may result in a drop in river flow level in rivers such as the Tugela and Vaal, which rise from the upper reaches of the Drakensberg. These rivers provide water for agriculture, hydroelectric power generation, and home use downstream. In addition, drought may negatively affect the Lesotho Highlands Water Project, which is a water supply project with a hydropower component, developed in partnership between the governments of Lesotho and South Africa. Putting an adequate plan or policy in place to mitigate these impacts would help to reduce the associated risks.

7.2 Recommendations

There is a need to improve the robustness of the results for practical purposes. It may be difficult to generalize the performance of CFSR on other reanalysis or global forecast products, which may have a different resolution or use different models than the CFSR. Future studies could extend the analysis to other global forecast products and compare the WSD precipitation biases across the products. In addition, due to time and resource constraints, the present study could only use one downscaling approach (dynamic downscaling) and one model (WRF) to downscale the reanalysis. Using multi-approach and multi-model to downscale the reanalysis or global forecast products would help quantify the uncertainty in the downscaling results and guide on the most efficient ways of improving the quality of the simulated precipitation over the mountain. Furthermore, extreme rainfall events are a threat to the Drakensberg. Future studies could investigate if extreme rainfall events could occur over mountains on WSDs because there is a possibility that the local-scale circulation systems can trigger deep convection which can induce extreme rainfall on WSDs. However, the present study has shown that weak-synoptic conditions over the Drakensberg can lead to heavy rainfall ($> 13\text{mm day}^{-1}$), which may not be captured in reanalysis or global forecasting products without downscaling.

In addition, while the study revealed the strength and weakness of two atmospheric models in simulating WERE over the mountain, only one realization of the models' simulation was considered, making it difficult to know how much error we can ascribe to the inadequacy of the models versus sampling uncertainty. Future work could perform a series of simulation ensembles with both models, using various parameterization schemes, initial conditions, boundary conditions (for WRF), and resolutions. Such information would go a long way in helping the model developers in improving the model performance over the Drakensberg. It will also guide the model users on how to optimise the model simulations for weather and climate studies or predictions. However, the present study has linked WERE over the Drakensberg with various synoptic patterns over Southern Africa and shows the capability of two climate models simulating the characteristics of the WERE.

Furthermore, the projected droughts over the Drakensberg from the SOM analysis are based on precipita-

tion alone; they do not however account for the role of potential evapotranspiration. Meanwhile, [Abiodun et al. \(2019\)](#) showed that accounting for atmospheric evaporative demand (potential evapotranspiration) in the drought projections (i.e., using the Standardised Precipitation Evapotranspiration Index [SPEI]) produced more severe droughts than using only precipitation (or the Standardized Precipitation Index [SPI]) for such projections. Hence, future studies could consider incorporating the influence of potential evapotranspiration on future drought projections over this mountain. In addition, the downscaled datasets do not have all the dynamic variables needed to investigate the dynamics behind the projected changes. Future studies could investigate the dynamics behind the projected changes using a series of sensitivity experiments with regional climate models (forced by GCM simulations) or a global model with a variable horizontal grid resolution. Furthermore, the present study has used regional climate simulations in which convection is activated through physical parameterizations of convective processes. Several studies have shown that explicit convection may produce sensibly different results and changes in rainfall properties (e.g., [Kendon et al., 2019](#)). Hence, analysing simulations with high resolution and explicit convection for the projections would provide more detailed information over a complex topography like the Drakensberg.

References

- Abiodun B.J., Abba Omar S., Lennard C., and Jack C.: 2016, *Using regional climate models to simulate extreme rainfall events in the Western Cape, South Africa*, *International Journal of Climatology*, 36, 2:pages 689–705.
- Abiodun B.J., Adegoke J., Abatan A.A., Ibe C.A., Egbebiyi T.S., Engelbrecht F., and Pinto I.: 2017, *Potential impacts of climate change on extreme precipitation over four African coastal cities*, *Climatic Change*, pages 1–15.
- Abiodun B.J., Makhanya N., Petja B., Abatan A.A., and Oguntunde P.G.: 2019, *Future projection of droughts over major river basins in Southern Africa at specific global warming levels*, *Theoretical and Applied Climatology*, 137, 3:pages 1785–1799.
- Abiodun B.J., Mogebeisa T.O., Petja B., Abatan A.A., and Roland T.R.: 2020, *Potential impacts of specific global warming levels on extreme rainfall events over southern Africa in CORDEX and NEX-GDDP ensembles*, *International Journal of Climatology*, 40, 6:pages 3118–3141.
- Adelabu D.B., Clark V.R., and Bredenhand E.: 2020, *Potential for sustainable mountain farming: challenges and prospects for sustainable smallholder farming in the Maloti–Drakensberg mountains*, *Mountain Research and Development*, 40, 1:page A1.
- Akinsanola A., Ogunjobi K., Gbode I., and Ajayi V.: 2015, *Assessing the capabilities of three regional climate models over CORDEX Africa in simulating West African summer monsoon precipitation*, *Advances in Meteorology*, 2015.
- Alexander L.V., Uotila P., Nicholls N., and Lynch A.: 2010, *A new daily pressure dataset for Australia and its application to the assessment of changes in synoptic patterns during the last century*, *Journal of Climate*, 23, 5:pages 1111–1126.
- Alexander W.J. and Emeritus W.J.: 2005, *Linkages between solar activity and climatic responses*, *Energy & Environment*, 16, 2:pages 239–253.
- Allen M.R. and Ingram W.J.: 2002, *Constraints on future changes in climate and the hydrologic cycle*, *Nature*, 419, 6903:pages 228–232.
- Araujo J.A., Abiodun B.J., and Crespo O.: 2016, *Impacts of drought on grape yields in Western Cape, South Africa*, *Theoretical and applied climatology*, 123, 1:pages 117–130.
- Arnell N., Hudson D., and Jones R.: 2003, *Climate change scenarios from a regional climate model: Estimating change in runoff in southern Africa*, *Journal of Geophysical Research: Atmospheres*, 108, D16.
- Baldwin M., Gray L., Dunkerton T., Hamilton K., Haynes P., Randel W., Holton J., Alexander M., Hirota I., Horinouchi T., et al.: 2001, *The quasi-biennial oscillation*, *Reviews of Geophysics*, 39, 2:pages 179–229.

- Bao Y. and Wen X.: 2017, *Projection of China's near-and long-term climate in a new high-resolution daily downscaled dataset NEX-GDDP*, *Journal of Meteorological Research*, 31, 1:pages 236–249.
- Barros A.P. and Lettenmaier D.P.: 1994, *Dynamic modeling of orographically induced precipitation*, *Reviews of geophysics*, 32, 3:pages 265–284.
- Barry R.G.: 1992, *Mountain weather and climate*, Psychology Press.
- Berg P. and Haerter J.: 2011, *Unexpected increase in precipitation intensity with temperature—A result of mixing of precipitation types?*, *Atmospheric Research*, 119:pages 56–61.
- Berg P., Moseley C., and Haerter J.O.: 2013, *Strong increase in convective precipitation in response to higher temperatures*, *Nature Geoscience*, 6, 3:pages 181–185.
- Blamey R., Middleton C., Lennard C., and Reason C.: 2017, *A climatology of potential severe convective environments across South Africa*, *Climate Dynamics*, 49, 5-6:pages 2161–2178.
- Blamey R. and Reason C.: 2013, *The role of mesoscale convective complexes in southern Africa summer rainfall*, *Journal of climate*, 26, 5:pages 1654–1668.
- Carbone R., Tuttle J., Cooper W., Grubišić V., and Lee W.: 1998, *Trade wind rainfall near the windward coast of Hawaii*, *Monthly weather review*, 126, 11:pages 2847–2863.
- Chen H.P., Sun J.Q., and Li H.X.: 2017, *Future changes in precipitation extremes over China using the NEX-GDDP high-resolution daily downscaled data-set*, *Atmospheric and Oceanic Science Letters*, 10, 6:pages 403–410.
- Christensen J.H., Carter T.R., Rummukainen M., and Amanatidis G.: 2007, *Evaluating the performance and utility of regional climate models: the PRUDENCE project*.
- Cook C., Reason C.J., and Hewitson B.C.: 2004, *Wet and dry spells within particularly wet and dry summers in the South African summer rainfall region*, *Climate Research*, 26, 1:pages 17–31.
- Crétat J., Pohl B., Richard Y., and Drobinski P.: 2012, *Uncertainties in simulating regional climate of Southern Africa: sensitivity to physical parameterizations using WRF*, *Climate dynamics*, 38, 3:pages 613–634.
- Crimp S. and Mason S.: 1999, *The extreme precipitation event of 11 to 16 February 1996 over South Africa*, *Meteorology and atmospheric physics*, 70, 1-2:pages 29–42.
- Crimp S.J., Lutjeharms J.R., and Mason S.J.: 1998, *Sensitivity of a tropical-temperate trough to sea-surface temperature anomalies in the Agulhas retroflexion region*, *WATER SA-PRETORIA*, 24:pages 93–100.
- De Coning E.: 2013, *Optimizing satellite-based precipitation estimation for nowcasting of rainfall and flash flood events over the South African domain*, *Remote Sensing*, 5, 11:pages 5702–5724.
- de Quervain A.: 1903, *Die Hebung der atmosphärischen Isothermen in den Schweizer Alpen und ihre Beziehung zu den Höhengrenzen*, W. Engelmann.
- de Sousa Pinto I.S.: 2015, *Future changes in extreme rainfall events and circulation patterns over southern Africa*, Ph.D. thesis, Department of Environmental & Geographical Science, University of Cape Town.

- Dedekind Z., Engelbrecht F.A., and Van der Merwe J.: 2016, *Model simulations of rainfall over southern Africa and its eastern escarpment*, *Water SA*, 42, 1:pages 129–143.
- Déqué M., Calmanti S., Christensen O.B., Aquila A.D., Maule C.F., Haensler A., Nikulin G., and Teichmann C.: 2017, *A multi-model climate response over tropical Africa at $\pm 2^\circ\text{C}$* , *Climate Services*, 7:pages 87–95.
- Diab R., Preston-Whyte R., and Washington R.: 1991, *Distribution of rainfall by synoptic type over Natal, South Africa*, *International journal of climatology*, 11, 8:pages 877–888.
- Diasso U. and Abiodun B.J.: 2017, *Drought modes in West Africa and how well CORDEX RCMs simulate them*, *Theoretical and Applied Climatology*, 128, 1:pages 223–240.
- Dieppois B., Pohl B., Rouault M., New M., Lawler D., and Keenlyside N.: 2016, *Interannual to inter-decadal variability of winter and summer southern African rainfall, and their teleconnections*, *Journal of Geophysical Research: Atmospheres*, 121, 11:pages 6215–6239.
- Dosio A. and Fischer E.M.: 2018, *Will half a degree make a difference? Robust projections of indices of mean and extreme climate in Europe under 1.5 C, 2 C, and 3 C global warming*, *Geophysical Research Letters*, 45, 2:pages 935–944.
- Dosio A. and Panitz H.J.: 2016, *Climate change projections for CORDEX-Africa with COSMO-CLM regional climate model and differences with the driving global climate models*, *Climate Dynamics*, 46, 5:pages 1599–1625.
- Driver P. and Reason C.: 2017, *Variability in the Botswana High and its relationships with rainfall and temperature characteristics over southern Africa*, *International Journal of Climatology*, 37:pages 570–581.
- Drobinski P., Silva N.D., Panthou G., Bastin S., Muller C., Ahrens B., Borga M., Conte D., Fosser G., Giorgi F., et al.: 2018, *Scaling precipitation extremes with temperature in the Mediterranean: past climate assessment and projection in anthropogenic scenarios*, *Climate dynamics*, 51, 3:pages 1237–1257.
- Dube L.: 2002, *Climate of southern Africa*, *South African Geographical Journal*, 84, 1:pages 125–138.
- Dyer T.: 1975, *Solar activity and rainfall variation over southern Africa*, *South African Journal of Science*, 71, 12:page 369.
- Engelbrecht F., Adegoke J., Bopape M.J., Naidoo M., Garland R., Thatcher M., McGregor J., Katzfey J., Werner M., Ichoku C., et al.: 2015, *Projections of rapidly rising surface temperatures over Africa under low mitigation*, *Environmental Research Letters*, 10, 8:page 085004.
- Engelbrecht F., McGregor J., and Engelbrecht C.: 2009, *Dynamics of the Conformal-Cubic Atmospheric Model projected climate-change signal over southern Africa*, *International Journal of Climatology: A Journal of the Royal Meteorological Society*, 29, 7:pages 1013–1033.
- Engelbrecht F., Rautenbach D.W., McGregor J., and Katzfey J.: 2002, *January and July climate simulations over the SADC region using the limited-area model DARLAM, WATER SA-PRETORIA*, 28, 4:pages 361–374.
- ETCCDI: 2022, *ETCCDI Climate Change Indices*, http://etccdi.pacificclimate.org/list_27_indices.shtml, [Online; accessed 20-November-2022].

- Everson C.: 2001, *The water balance of a first order catchment in the montane grasslands of South Africa*, *Journal of Hydrology*, 241, 1-2:pages 110–123.
- Fatti C.E. and Patel Z.: 2013, *Perceptions and responses to urban flood risk: Implications for climate governance in the South*, *Applied Geography*, 36:pages 13–22.
- Favre A., Hewitson B., Lennard C., Cerezo-Mota R., and Tadross M.: 2013, *Cut-off lows in the South Africa region and their contribution to precipitation*, *Climate dynamics*, 41, 9:pages 2331–2351.
- Favre A., Philippon N., Pohl B., Kalognomou E.A., Lennard C., Hewitson B., Nikulin G., Dosio A., Panitz H.J., and Cerezo-Mota R.: 2016, *Spatial distribution of precipitation annual cycles over South Africa in 10 CORDEX regional climate model present-day simulations*, *Climate Dynamics*, 46, 5:pages 1799–1818.
- Fosser G., Khodayar S., and Berg P.: 2015, *Benefit of convection permitting climate model simulations in the representation of convective precipitation*, *Climate Dynamics*, 44, 1:pages 45–60.
- Funk C.C., Peterson P.J., Landsfeld M.F., Pedreros D.H., Verdin J.P., Rowland J.D., Romero B.E., Husak G.J., Michaelsen J.C., and Verdin A.P.: 2014, *A quasi-global precipitation time series for drought monitoring*, Technical report, US Geological Survey.
- Gaffin D.M., Parker S.S., and Kirkwood P.D.: 2003, *An unexpectedly heavy and complex snowfall event across the southern Appalachian region*, *Weather and Forecasting*, 18, 2:pages 224–235.
- Giorgi F.: 1990, *Simulation of regional climate using a limited area model nested in a general circulation model*, *Journal of Climate*, 3, 9:pages 941–963.
- Giorgi F., Jones C., Asrar G.R., et al.: 2009, *Addressing climate information needs at the regional level: the CORDEX framework*, *World Meteorological Organization (WMO) Bulletin*, 58, 3:page 175.
- Giorgi F. and Mearns L.O.: 1991, *Approaches to the simulation of regional climate change: a review*, *Reviews of Geophysics*, 29, 2:pages 191–216.
- Giorgi F. and Mearns L.O.: 1999, *Introduction to special section: Regional climate modeling revisited*, *Journal of Geophysical Research: Atmospheres*, 104, D6:pages 6335–6352.
- Grab S. and Simpson A.: 2000, *Climatic and environmental impacts of cold fronts over KwaZulu-Natal and the adjacent interior of southern Africa*, *South African Journal of Science*, 96, 11-12:pages 602–608.
- Ha S., Snyder C., Skamarock W.C., Anderson J., and Collins N.: 2017, *Ensemble Kalman filter data assimilation for the Model for Prediction Across Scales (MPAS)*, *Monthly Weather Review*, 145, 11:pages 4673–4692.
- Haeberli W. and Beniston M.: 1998, *Climate change and its impacts on glaciers and permafrost in the Alps*, *Ambio*, pages 258–265.
- Haensler A., Hagemann S., and Jacob D.: 2011, *The role of the simulation setup in a long-term high-resolution climate change projection for the southern African region*, *Theoretical and applied climatology*, 106, 1-2:pages 153–169.
- Haerter J.O. and Berg P.: 2009, *Unexpected rise in extreme precipitation caused by a shift in rain type?*, *Nature Geoscience*, 2, 6:pages 372–373.

- Harangozo S. and Harrison M.: 1983, *ON THE USE OF SYNOPTIC DATA IN INDICATING THE PRESENCE OF CLOUD BANDS OVER SOUTHERN-AFRICA*, *South African Journal of Science*, 79, 10:pages 413–414.
- Harrison M.: 1984, *A generalized classification of South African summer rain-bearing synoptic systems*, *Journal of Climatology*, 4, 5:pages 547–560.
- Hart N., Reason C., and Fauchereau N.: 2010, *Tropical–extratropical interactions over southern Africa: Three cases of heavy summer season rainfall*, *Monthly weather review*, 138, 7:pages 2608–2623.
- Hart N.C., Reason C.J., and Fauchereau N.: 2013, *Cloud bands over southern Africa: Seasonality, contribution to rainfall variability and modulation by the MJO*, *Climate dynamics*, 41, 5:pages 1199–1212.
- Heinzeller D., Duda M.G., and Kunstmann H.: 2016, *Towards convection-resolving, global atmospheric simulations with the Model for Prediction Across Scales (MPAS) v3. 1: An extreme scaling experiment*, *Geoscientific Model Development*, 9, 1:pages 77–110.
- Held I.M., Soden B.J., et al.: 2000, *Water vapor feedback and global warming*, *Annual review of energy and the environment*, 25, 1:pages 441–475.
- Hemmati M., Kornhuber K., and Kruczkiewicz A.: 2022, *Enhanced urban adaptation efforts needed to counter rising extreme rainfall risks*, *npj Urban Sustainability*, 2, 1:pages 1–5.
- Hernández-Díaz L., Laprise R., Sushama L., Martynov A., Winger K., and Dugas B.: 2013, *Climate simulation over CORDEX Africa domain using the fifth-generation Canadian Regional Climate Model (CRCM5)*, *Climate Dynamics*, 40, 5:pages 1415–1433.
- Hertig E., Seubert S., Jacobeit J., Paxian A., Vogt G., and Paeth H.: 2012, *Statistical and dynamical downscaling assessments of precipitation extremes in the Mediterranean area*, *Meteorologische Zeitschrift (Berlin)*, 21.
- Hewitson B. and Crane R.: 2006, *Consensus between GCM climate change projections with empirical downscaling: precipitation downscaling over South Africa*, *International Journal of Climatology: A Journal of the Royal Meteorological Society*, 26, 10:pages 1315–1337.
- Hewitson B.C. and Crane R.G.: 2002, *Self-organizing maps: applications to synoptic climatology*, *Climate Research*, 22, 1:pages 13–26.
- Hohenegger C., Brockhaus P., and Schar C.: 2008, *Towards climate simulations at cloud-resolving scales*, *Meteorologische Zeitschrift*, 17, 4:pages 383–394.
- Hope P.K.: 2006, *Projected future changes in synoptic systems influencing southwest Western Australia*, *Climate Dynamics*, 26, 7-8:pages 765–780.
- Houze Jr R.A.: 2012, *Orographic effects on precipitating clouds*, *Reviews of Geophysics*, 50, 1.
- Hughes W.S. and Balling Jr R.C.: 1996, *Urban influences on South African temperature trends*, *International Journal of Climatology: A Journal of the Royal Meteorological Society*, 16, 8:pages 935–940.
- Hulme M.: 1992, *Rainfall changes in Africa: 1931–1960 to 1961–1990*, *International Journal of Climatology*, 12, 7:pages 685–699.

- Hulme M., Doherty R., Ngara T., New M., and Lister D.: 2001, *African climate change: 1900-2100. ClimateResearch17: 145–168.*
- Hunter E.C., Hendry M.T., and Cruden D.M.: 2016, *Effects of extreme rainfall on geotechnical hazards in the Canadian Rocky Mountains, in 'Proceedings of the 17th Nordic Geotechnical Meeting', NGM 2016 Reykjavik. Proceedings of the 17th Nordic Geotechnical Meeting.*
- Hyden L., Sekoli T., et al.: 2000, *Possibilities to forecast early summer rainfall in the Lesotho Lowlands from the El-Nino/Southern Oscillation, WATER SA-PRETORIA-, 26, 1:pages 83–90.*
- IPCC W.: 2007, *Climate change 2007: the physical science basis.*
- Ivancic T.J. and Shaw S.B.: 2016, *A US-based analysis of the ability of the Clausius-Clapeyron relationship to explain changes in extreme rainfall with changing temperature, Journal of Geophysical Research: Atmospheres, 121, 7:pages 3066–3078.*
- Jones P.D.: 1994, *Hemispheric surface air temperature variations: a reanalysis and an update to 1993, Journal of Climate, 7, 11:pages 1794–1802.*
- Joubert A.: 1994, *Simulations of southern African climatic change by early-generation general circulation models, WATER SA-PRETORIA-, 20:pages 315–315.*
- Joubert A. and Hewitson B.: 1997, *Simulating present and future climates of southern Africa using general circulation models, Progress in Physical Geography, 21, 1:pages 51–78.*
- Joubert A., Katzfey J., McGregor J., and Nguyen K.: 1999, *Simulating midsummer climate over southern Africa using a nested regional climate model, Journal of Geophysical Research: Atmospheres, 104, D16:pages 19015–19025.*
- Jury M.R.: 2012, *An inter-comparison of model-simulated east–west climate gradients over South Africa, Water SA, 38, 4:pages 467–478.*
- Jury M.R., White W.B., and Reason C.J.: 2004, *Modelling the dominant climate signals around southern Africa, Climate dynamics, 23, 7-8:pages 717–726.*
- Kalognomou E.A., Lennard C., Shongwe M., Pinto I., Favre A., Kent M., Hewitson B., Dosio A., Nikulin G., Panitz H.J., et al.: 2013, *A diagnostic evaluation of precipitation in CORDEX models over southern Africa, Journal of climate, 26, 23:pages 9477–9506.*
- Kane R.: 2009, *Periodicities, ENSO effects and trends of some South African rainfall series: an update, South African Journal of Science, 105, 5:pages 199–207.*
- Karl T.R., Jones P.D., Knight R.W., Kukla G., Plummer N., Razuvayev V., Gallo K.P., Lindsey J., Charlson R.J., and Peterson T.C.: 1993, *Asymmetric trends of daily maximum and minimum temperature, Papers in Natural Resources, page 185.*
- Karl T.R. and Trenberth K.E.: 2003, *Modern global climate change, science, 302, 5651:pages 1719–1723.*
- Kendon E.J., Stratton R.A., Tucker S., Marsham J.H., Berthou S., Rowell D.P., and Senior C.A.: 2019, *Enhanced future changes in wet and dry extremes over Africa at convection-permitting scale, Nature communications, 10, 1:pages 1–14.*

- Klein Tank AMG Zwiers FW Z.X.: 2009, *Guidelines on analysis of extremes in a changing climate in support of informed decisions for adaptation. Climate data and monitoring WCDMP-No. 72, WMOTD No. 1500.*, World Meteorological Organization.
- Klutse N.A.B., Sylla M.B., Diallo I., Sarr A., Dosio A., Diedhiou A., Kamga A., Lamptey B., Ali A., Gbobaniyi E.O., et al.: 2016, *Daily characteristics of West African summer monsoon precipitation in CORDEX simulations, Theoretical and Applied Climatology*, 123, 1:pages 369–386.
- Knight J. and Grab S.: 2015, *The Drakensberg escarpment: mountain processes at the edge*, in *Landscapes and Landforms of South Africa*, pages 47–55, Springer.
- Kohonen T.: 1990, *The self-organizing map, Proceedings of the IEEE*, 78, 9:pages 1464–1480.
- Kruger A.: 2006, *Observed trends in daily precipitation indices in South Africa: 1910–2004, International Journal of Climatology*, 26, 15:pages 2275–2285.
- Kruger A.C. and Shongwe S.: 2004, *Temperature trends in South Africa: 1960–2003, International Journal of Climatology: A Journal of the Royal Meteorological Society*, 24, 15:pages 1929–1945.
- Kusangaya S., Warburton M.L., Van Garderen E.A., and Jewitt G.P.: 2014, *Impacts of climate change on water resources in southern Africa: A review, Physics and Chemistry of the Earth, Parts A/B/C*, 67:pages 47–54.
- LaCorte J.: 1999, *Improving Convective Forecasts in Weakly Forced Environments*, URL https://repository.library.noaa.gov/view/noaa/6674/noaa_6674_DS1.pdf.
- Laprise R., Hernández-Díaz L., Tete K., Sushama L., Šeparović L., Martynov A., Winger K., and Valin M.: 2013, *Climate projections over CORDEX Africa domain using the fifth-generation Canadian Regional Climate Model (CRCM5), Climate Dynamics*, 41, 11:pages 3219–3246.
- Legates D.R.: 2014, *Climate models and their simulation of precipitation, Energy & environment*, 25, 6-7:pages 1163–1175.
- Lenderink G., Barbero R., Loriaux J., and Fowler H.: 2017, *Super Clausius-Clapeyron scaling of extreme hourly precipitation and its relation to large-scale atmospheric conditions*, in *EGU General Assembly Conference Abstracts*, page 13162.
- Lenderink G. and Van Meijgaard E.: 2008, *Increase in hourly precipitation extremes beyond expectations from temperature changes, Nature Geoscience*, 1, 8:pages 511–514.
- Lenderink G. and Van Meijgaard E.: 2010, *Linking increases in hourly precipitation extremes to atmospheric temperature and moisture changes, Environmental Research Letters*, 5, 2:page 025208.
- Lennard C. and Hegerl G.: 2015, *Relating changes in synoptic circulation to the surface rainfall response using self-organising maps, Climate Dynamics*, 44, 3:pages 861–879.
- Levey K.M.: 1996, *Interannual temperature variability and associated synoptic climatology at Cape Town, International journal of climatology*, 16, 3:pages 293–306.
- Li H., Gao J., Zhang H., Zhang Y., and Zhang Y.: 2017, *Response of extreme precipitation to solar activity and El Nino events in typical regions of the Loess Plateau, Advances in Meteorology*, 2017.

- Loriaux J.M., Lenderink G., De Roode S.R., and Siebesma A.P.: 2013, *Understanding convective extreme precipitation scaling using observations and an entraining plume model*, *Journal of the Atmospheric Sciences*, 70, 11:pages 3641–3655.
- Macron C., Pohl B., Richard Y., and Bessafi M.: 2014, *How do tropical temperate troughs form and develop over southern Africa?*, *Journal of Climate*, 27, 4:pages 1633–1647.
- Manabe S. and Wetherald R.T.: 1967, *Thermal equilibrium of the atmosphere with a given distribution of relative humidity*.
- Maoyi M.L. and Abiodun B.J.: 2022, *Investigating the response of the Botswana High to El Niño Southern Oscillation using a variable resolution global climate model*, *Theoretical and Applied Climatology*, pages 1–15.
- Maoyi M.L., Abiodun B.J., Prusa J.M., and Veitch J.J.: 2018, *Simulating the characteristics of tropical cyclones over the South West Indian Ocean using a Stretched-Grid Global Climate Model*, *Climate dynamics*, 50, 5-6:pages 1581–1596.
- Marbaix P., Gallée H., Brasseur O., and van Ypersele J.P.: 2003, *Lateral boundary conditions in regional climate models: a detailed study of the relaxation procedure*, *Monthly weather review*, 131, 3:pages 461–479.
- Markowski P. and Richardson Y.: 2011, *Mesoscale meteorology in midlatitudes*, volume 2, John Wiley & Sons.
- Mason S. and Tyson P.: 1992, *The modulation of sea surface temperature and rainfall associations over southern Africa with solar activity and the quasi-biennial oscillation*, *Journal of Geophysical Research: Atmospheres*, 97, D5:pages 5847–5856.
- Mason S.J.: 2001, *El Niño, climate change, and Southern African climate*, *Environmetrics: The official journal of the International Environmetrics Society*, 12, 4:pages 327–345.
- Mason S.J. and Jury M.: 1997, *Climatic variability and change over southern Africa: a reflection on underlying processes*, *Progress in physical geography*, 21, 1:pages 23–50.
- Mason S.J., Waylen P.R., Mimmack G.M., Rajaratnam B., and Harrison J.M.: 1999, *Changes in extreme rainfall events in South Africa*, *Climatic Change*, 41, 2:pages 249–257.
- Maúre G., Pinto I., Ndebele-Murisa M., Muthige M., Lennard C., Nikulin G., Dosio A., and Meque A.: 2018, *The southern African climate under 1.5 C and 2 C of global warming as simulated by CORDEX regional climate models*, *Environmental Research Letters*, 13, 6:page 065002.
- Mazvimavi D.: 2010, *Climate change, water availability and supply*, *SARUA Leadership Dialogue Series*, 2, 4:pages 81–97.
- Mba W.P., Longandjo G.N.T., Moufouma-Okia W., Bell J.P., James R., Vondou D.A., Haensler A., Fotso-Nguemo T.C., Guenang G.M., Tchotchou A.L.D., et al.: 2018, *Consequences of 1.5 C and 2 C global warming levels for temperature and precipitation changes over Central Africa*, *Environmental Research Letters*, 13, 5:page 055011.
- McCauley M. and Sturman A.: 1999, *A study of orographic blocking and barrier wind development upstream of the Southern Alps, New Zealand*, *Meteorology and Atmospheric Physics*, 70, 3-4:pages 121–131.

- Meinshausen M., Smith S.J., Calvin K., Daniel J.S., Kainuma M.L., Lamarque J.F., Matsumoto K., Montzka S.A., Raper S.C., Riahi K., et al.: 2011, *The RCP greenhouse gas concentrations and their extensions from 1765 to 2300*, *Climatic change*, 109, 1:pages 213–241.
- Miller S., Keim B., Talbot R., and Mao H.: 2003, *Sea breeze: Structure, forecasting, and impacts*, *Reviews of geophysics*, 41, 3.
- Mizuta R., Arakawa O., Ose T., Kusunoki S., Endo H., and Kitoh A.: 2014, *Classification of CMIP5 future climate responses by the tropical sea surface temperature changes*, *Sola*, 10:pages 167–171.
- Molekwa S., Engelbrecht C.J., and Rautenbach C.: 2014, *Attributes of cut-off low induced rainfall over the Eastern Cape Province of South Africa*, *Theoretical and applied climatology*, 118, 1:pages 307–318.
- Molnar P., Fatichi S., Gaál L., Szolgay J., and Burlando P.: 2015, *Storm type effects on super Clausius–Clapeyron scaling of intense rainstorm properties with air temperature*, *Hydrology and Earth System Sciences*, 19, 4:pages 1753–1766.
- Monerie P.A., Sanchez-Gomez E., and Boé J.: 2017, *On the range of future Sahel precipitation projections and the selection of a sub-sample of CMIP5 models for impact studies*, *Climate Dynamics*, 48, 7:pages 2751–2770.
- Morris C.D., Everson C.S., Everson T.M., and Gordijn P.J.: 2021, *Frequent burning maintained a stable grassland over four decades in the Drakensberg, South Africa*, *African Journal of Range & Forage Science*, 38, 1:pages 39–52.
- Mpungose N., Thoithi W., Blamey R., and Reason C.: 2022, *Extreme rainfall events in southeastern Africa during the summer*, *Theoretical and Applied Climatology*, pages 1–17.
- Mukwada G., Le Roux A., Hlalele D., and Lombard C.: 2016, *The afromontane research unit (ARU) in South Africa*, *Mountain Research and Development*, 36, 3:pages 384–386.
- Mukwada G., Mazibuko S.M., Moeletsi M., and Robinson G.M.: 2021, *Can Famine Be Averted? A Spatiotemporal Assessment of The Impact of Climate Change on Food Security in The Luvuvhu River Catchment of South Africa*, *Land*, 10, 5:page 527.
- Mulder N. and Grab S.W.: 2009, *Contemporary spatio-temporal patterns of snow cover over the Drakensberg, South African Journal of Science*, 105, 5:pages 228–233.
- Munday C. and Washington R.: 2017, *Circulation controls on southern African precipitation in coupled models: The role of the Angola low*, *Journal of Geophysical Research: Atmospheres*, 122, 2:pages 861–877.
- Mutana S. and Mukwada G.: 2020, *Are policies and guidelines shaping tourism sustainability in South Africa? Critical success factors for tourism sustainability governance in the Drakensberg region*, *Tourism and Hospitality Research*, 20, 2:pages 198–209.
- Nayak S. and Takemi T.: 2020, *Clausius-Clapeyron scaling of extremely heavy precipitations: Case studies of the July 2017 and July 2018 heavy rainfall events over Japan*, *Journal of the Meteorological Society of Japan. Ser. II*.
- Ndarana T., Bopape M.J., Waugh D., and Dyson L.: 2018, *The influence of the lower stratosphere on ridging Atlantic ocean anticyclones over South Africa*, *Journal of Climate*, 31, 15:pages 6175–6187.

- Ndarana T., Mpati S., Bopape M.J., Engelbrecht F., and Chikooore H.: 2021, *The flow and moisture fluxes associated with ridging South Atlantic Ocean anticyclones during the subtropical southern African summer*, *International Journal of Climatology*, 41:pages E1000–E1017.
- Ndarana T., Rammopo T.S., Reason C.J., Bopape M.J., Engelbrecht F., and Chikooore H.: 2022, *Two types of ridging South Atlantic Ocean anticyclones over South Africa and the associated dynamical processes*, *Atmospheric Research*, 265:page 105897.
- Nel W.: 2007, *Intra-storm attributes of extreme storm events in the Drakensberg, South Africa*, *Physical Geography*, 28, 2:pages 158–169.
- Nel W.: 2008, *Observations on daily rainfall events in the KwaZulu-Natal Drakensberg*, *Water SA*, 34, 2:pages 271–274.
- Nel W.: 2009, *Rainfall trends in the KwaZulu-Natal Drakensberg region of South Africa during the twentieth century*, *International Journal of Climatology*, 29, 11:pages 1634–1641.
- Nel W. and Sumner P.: 2005, *Short communication First rainfall data from the KZN Drakensberg escarpment edge (2002 and 2003)*, *Water SA*, 31, 3:pages 399–402.
- Nel W. and Sumner P.: 2006, *Trends in rainfall total and variability (1970–2000) along the KwaZulu-Natal Drakensberg foothills*, *South African Geographical Journal*, 88, 2:pages 130–137.
- Nel W. and Sumner P.: 2008, *Rainfall and temperature attributes on the Lesotho–Drakensberg escarpment edge, southern Africa*, *Geografiska Annaler: Series A, Physical Geography*, 90, 1:pages 97–108.
- New M., Hewitson B., Stephenson D.B., Tsiga A., Kruger A., Manhique A., Gomez B., Coelho C.A., Masisi D.N., Kululanga E., et al.: 2006, *Evidence of trends in daily climate extremes over southern and west Africa*, *Journal of Geophysical Research: Atmospheres*, 111, D14.
- Nicholson S.E.: 2018, *The ITCZ and the seasonal cycle over equatorial Africa*, *Bulletin of the American Meteorological Society*, 99, 2:pages 337–348.
- Nikulin G., Jones C., Giorgi F., Asrar G., Büchner M., Cerezo-Mota R., Christensen O.B., Déqué M., Fernandez J., Hänsler A., et al.: 2012, *Precipitation climatology in an ensemble of CORDEX-Africa regional climate simulations*, *Journal of Climate*, 25, 18:pages 6057–6078.
- Nikulin G., Lennard C., Dosio A., Kjellström E., Chen Y., Hänsler A., Kupiainen M., Laprise R., Mariotti L., Maule C.F., et al.: 2018, *The effects of 1.5 and 2 degrees of global warming on Africa in the CORDEX ensemble*, *Environmental Research Letters*, 13, 6:page 065003.
- Novella N.S. and Thiaw W.M.: 2013, *African rainfall climatology version 2 for famine early warning systems*, *Journal of Applied Meteorology and Climatology*, 52, 3:pages 588–606.
- Odoulami R.C., Wolski P., and New M.: 2021, *A SOM-based analysis of the drivers of the 2015–2017 Western Cape drought in South Africa*, *International Journal of Climatology*, 41:pages E1518–E1530.
- Omar S.A. and Abiodun B.J.: 2017, *How well do CORDEX models simulate extreme rainfall events over the East Coast of South Africa?*, *Theoretical and Applied Climatology*, 128, 1–2:pages 453–464.
- Omar S.A. and Abiodun B.J.: 2020, *Characteristics of cut-off lows during the 2015–2017 drought in the Western Cape, South Africa*, *Atmospheric Research*, 235:page 104772.

- O'Gorman P.A.: 2015, *Precipitation extremes under climate change*, *Current climate change reports*, 1, 2:pages 49–59.
- Paegle J., Pielke R.A., Dalu G., Miller W., Garratt J., Vukicevic T., Berri G., and Nicolini M.: 1990, *Predictability of flows over complex terrain*, in *Atmospheric Processes over Complex Terrain*, pages 285–299, Springer.
- Pan Z., Zhu J., Liu J., Gu J., Liu Z., Qin F., and Pan Y.: 2021, *Estimation of air temperature and the mountain-mass effect in the Yellow River Basin using multi-source data*, *Plos one*, 16, 10:page e0258549.
- Panthou G., Mailhot A., Laurence E., and Talbot G.: 2014, *Relationship between surface temperature and extreme rainfalls: A multi-time-scale and event-based analysis*, *Journal of hydrometeorology*, 15, 5:pages 1999–2011.
- Park S.H., Klemp J.B., and Skamarock W.C.: 2014, *A comparison of mesh refinement in the global MPAS-A and WRF models using an idealized normal-mode baroclinic wave simulation*, *Monthly Weather Review*, 142, 10:pages 3614–3634.
- Pathak R., Sahany S., Mishra S.K., and Dash S.: 2019, *Precipitation biases in CMIP5 models over the south Asian region*, *Scientific reports*, 9, 1:pages 1–13.
- Phillips T.J., Potter G.L., Williamson D.L., Cederwall R.T., Boyle J.S., Fiorino M., Hnilo J.J., Olson J.G., Xie S., and Yio J.J.: 2004, *Evaluating parameterizations in general circulation models: Climate simulation meets weather prediction*, *Bulletin of the American Meteorological Society*, 85, 12:pages 1903–1916.
- Pielke R.: 1984, *Mesoscale Meteorological Modeling* Academic Press, New York, NY, USA, pages 1–612.
- Pinto I., Zachariah M., Wolski P., Landman S., Phakula V., Maluleke W., Bopape M.J., Engelbrecht C., Jack C., McClure A., Bonnet R., Vautard R., Sjoukje P., Kew S., Heinrich D., Vahlberg M., Singh R., Arrighi J., Thalheimer L., van Aalst M., Li S., Sun J., Vecchi G., Yang W., Tradowsky J., Otto F.E., and Dipura R.: 2022, *Climate change exacerbated rainfall causing devastating flooding in Eastern South Africa*, URL <https://www.worldweatherattribution.org/wp-content/uploads/WWA-KZN-floods-scientific-report.pdf>.
- Pohl B., Macron C., and Monerie P.A.: 2017, *Fewer rainy days and more extreme rainfall by the end of the century in Southern Africa*, *Scientific Reports*, 7.
- Powers J.G., Klemp J.B., Skamarock W.C., Davis C.A., Dudhia J., Gill D.O., Coen J.L., Gochis D.J., Ahmadov R., Peckham S.E., et al.: 2017, *The weather research and forecasting model: Overview, system efforts, and future directions*, *Bulletin of the American Meteorological Society*, 98, 8:pages 1717–1737.
- Preston-Whyte R., Diab R., and Washington R.: 1991, *Diurnal variation of rainfall events by synoptic type in Natal*, *South African geographical journal*, 73, 1:pages 22–28.
- Preston-Whyte R.A. and Tyson P.D.: 1988, *Atmosphere and weather of southern Africa*, Oxford University Press.
- Ratna S.B., Behera S., Ratnam J.V., Takahashi K., and Yamagata T.: 2013, *An index for tropical temperate troughs over southern Africa*, *Climate dynamics*, 41, 2:pages 421–441.

- Ratna S.B., Ratnam J., Behera S., Rautenbach C.d., Ndarana T., Takahashi K., and Yamagata T.: 2014, *Performance assessment of three convective parameterization schemes in WRF for downscaling summer rainfall over South Africa*, *Climate dynamics*, 42, 11:pages 2931–2953.
- Ratnam J., Behera S., Masumoto Y., Takahashi K., and Yamagata T.: 2012, *A simple regional coupled model experiment for summer-time climate simulation over southern Africa*, *Climate dynamics*, 39, 9:pages 2207–2217.
- Reason C.: 2019, *Low-frequency variability in the Botswana High and southern African regional climate*, *Theoretical and Applied Climatology*, 137, 1:pages 1321–1334.
- Reason C. and Jagadheesha D.: 2005, *A model investigation of recent ENSO impacts over southern Africa*, *Meteorology and Atmospheric Physics*, 89, 1:pages 181–205.
- Rouault M., Florenchie P., Fauchereau N., and Reason C.J.: 2003, *South East tropical Atlantic warm events and southern African rainfall*, *Geophysical Research Letters*, 30, 5.
- Ruane A.C., Goldberg R., and Chryssanthacopoulos J.: 2015, *Climate forcing datasets for agricultural modeling: Merged products for gap-filling and historical climate series estimation*, *Agricultural and Forest Meteorology*, 200:pages 233–248.
- Saha S., Moorthi S., Pan H.L., Wu X., Wang J., Nadiga S., Tripp P., Kistler R., Woollen J., Behringer D., Liu H., Stokes D., Grumbine R., Gayno G., Wang J., Hou Y.T., Chuang H.Y., Juang H.M.H., Sela J., Iredell M., Treadon R., Kleist D., Van Delst P., Keyser D., Derber J., Ek M., Meng J., Wei H., Yang R., Lord S., van den Dool H., Kumar A., Wang W., Long C., Chelliah M., Xue Y., Huang B., Schemm J.K., Ebisuzaki W., Lin R., Xie P., Chen M., Zhou S., Higgins W., Zou C.Z., Liu Q., Chen Y., Han Y., Cucurull L., Reynolds R.W., Rutledge G., and Goldberg M.: 2010, *NCEP Climate Forecast System Reanalysis (CFSR) 6-hourly Products, January 1979 to December 2010*, URL <https://doi.org/10.5065/D69K487J>.
- Saha S., Moorthi S., Wu X., Wang J., Nadiga S., Tripp P., Behringer D., Hou Y.T., ya Chuang H., Iredell M., Ek M., Meng J., Yang R., Mendez M.P., van den Dool H., Zhang Q., Wang W., Chen M., and Becker E.: 2011, *NCEP Climate Forecast System Version 2 (CFSv2) 6-hourly Products*, URL <https://doi.org/10.5065/D61C1TXF>.
- Sahana A., Pathak A., Roxy M., and Ghosh S.: 2019, *Understanding the role of moisture transport on the dry bias in Indian monsoon simulations by CFSv2*, *Climate Dynamics*, 52, 1:pages 637–651.
- Sakalli A., Cescatti A., Dosio A., and Gücel M.U.: 2017, *Impacts of 2 C global warming on primary production and soil carbon storage capacity at pan-European level*, *Climate Services*, 7:pages 64–77.
- Schär C., Ban N., Fischer E.M., Rajczak J., Schmidli J., Frei C., Giorgi F., Karl T.R., Kendon E.J., Tank A.M., et al.: 2016, *Percentile indices for assessing changes in heavy precipitation events*, *Climatic Change*, 137, 1:pages 201–216.
- Schleussner C.F., Lissner T.K., Fischer E.M., Wohland J., Perrette M., Golly A., Rogelj J., Childers K., Schewe J., Frieler K., et al.: 2016, *Differential climate impacts for policy-relevant limits to global warming: the case of 1.5 C and 2 C*, *Earth system dynamics*, 7, 2:pages 327–351.
- Schröer K. and Kirchengast G.: 2018, *Sensitivity of extreme precipitation to temperature: the variability of scaling factors from a regional to local perspective*, *Climate Dynamics*, 50, 11:pages 3981–3994.
- Schulze R.: 1979, *Hydrology and water resources of the Drakensberg*, Report, , 6.

- Schulze R., Kunz R., and Knoesen D.: 2010, *Atlas of Climate Change and Water Resources in South Africa*, Water Research Commission, Pretoria, RSA, WRC Report 1843/1/10.
- Schulze R.E.: 2011, *Approaches towards practical adaptive management options for selected water-related sectors in South Africa in a context of climate change*, *Water SA*, 37, 5:pages 621–646.
- Sene K., Jones D., Meigh J., and Farquharson F.: 1998, *Rainfall and flow variations in the Lesotho Highlands*, *International Journal of Climatology*, 18, 3:pages 329–345.
- Sheridan S.C. and Lee C.C.: 2011, *The self-organizing map in synoptic climatological research*, *Progress in Physical Geography*, 35, 1:pages 109–119.
- Simmons A., Willett K., Jones P., Thorne P., and Dee D.: 2010, *Low-frequency variations in surface atmospheric humidity, temperature, and precipitation: Inferences from reanalyses and monthly gridded observational data sets*, *Journal of Geophysical Research: Atmospheres*, 115, D1.
- Singleton A. and Reason C.: 2006, *Numerical simulations of a severe rainfall event over the Eastern Cape coast of South Africa: sensitivity to sea surface temperature and topography*, *Tellus A*, 58, 3:pages 355–367.
- Singleton A. and Toumi R.: 2013, *Super-Clausius–Clapeyron scaling of rainfall in a model squall line*, *Quarterly Journal of the Royal Meteorological Society*, 139, 671:pages 334–339.
- Skamarock W.C. and Klemp J.B.: 2008, *A time-split nonhydrostatic atmospheric model for weather research and forecasting applications*, *Journal of Computational Physics*, 227, 7:pages 3465–3485.
- Skamarock W.C., Klemp J.B., Duda M.G., Fowler L.D., Park S.H., and Ringler T.D.: 2012, *A multi-scale nonhydrostatic atmospheric model using centroidal Voronoi tessellations and C-grid staggering*, *Monthly Weather Review*, 140, 9:pages 3090–3105.
- Skamarock W.C., Klemp J.B., Dudhia J., Gill D.O., Barker D.M., Wang W., and Powers J.G.: 2005, *A description of the advanced research WRF version 2*, Technical report, National Center For Atmospheric Research Boulder Co Mesoscale and Microscale
- Sorooshian S., Hsu K.L., Gao X., Gupta H.V., Imam B., and Braithwaite D.: 2000, *Evaluation of PER-SIANN system satellite-based estimates of tropical rainfall*, *Bulletin of the American Meteorological Society*, 81, 9:pages 2035–2046.
- Stander J.H., Dyson L., and Engelbrecht C.J.: 2016, *A snow forecasting decision tree for significant snowfall over the interior of South Africa*, *South African Journal of Science*, 112, 9-10:pages 1–10.
- Steiner M., Bousquet O., Houze Jr R.A., Smull B.F., and Mancini M.: 2003, *Airflow within major Alpine river valleys under heavy rainfall*, *Quarterly Journal of the Royal Meteorological Society: A journal of the atmospheric sciences, applied meteorology and physical oceanography*, 129, 588:pages 411–431.
- Stensrud D.J. and Fritsch J.M.: 1993, *Mesoscale convective systems in weakly forced large-scale environments. Part I: Observations*, *Monthly weather review*, 121, 12:pages 3326–3344.
- Steynor A., Hewitson B., and Tadross M.: 2009, *Projected future runoff of the Breede River under climate change*, *Water sa*, 35, 4.
- Stull R.: 2015, *Practical meteorology, An algebra-based survey of atmospheric science*. University of British Columbia, Columbia.

- Sylla M., Giorgi F., Coppola E., and Mariotti L.: 2013, *Uncertainties in daily rainfall over Africa: assessment of gridded observation products and evaluation of a regional climate model simulation*, *International Journal of Climatology*, 33, 7:pages 1805–1817.
- Tadross M., Davis C., Engelbrecht F., Joubert A., and Archer E.R.: 2011, *Regional scenarios of future climate change over southern Africa*, CSIR.
- Tadross M., Jack C., and Hewitson B.: 2005, *On RCM-based projections of change in southern African summer climate*, *Geophysical Research Letters*, 32, 23.
- Taljaard J.: 1986, *Change of rainfall distribution and circulation patterns over southern Africa in summer*, *Journal of Climatology*, 6, 6:pages 579–592.
- Tang J., Niu X., Wang S., Gao H., Wang X., and Wu J.: 2016, *Statistical downscaling and dynamical downscaling of regional climate in China: Present climate evaluations and future climate projections*, *Journal of Geophysical Research: Atmospheres*, 121, 5:pages 2110–2129.
- Taylor K.E.: 2001, *Summarizing multiple aspects of model performance in a single diagram*, *Journal of Geophysical Research: Atmospheres*, 106, D7:pages 7183–7192.
- Taylor K.E., Stouffer R.J., and Meehl G.A.: 2012, *An overview of CMIP5 and the experiment design*, *Bulletin of the American meteorological Society*, 93, 4:pages 485–498.
- Taylor S., Ferguson J., Engelbrecht F.A., Clark V., Van Rensburg S., and Barker N.: 2016, *The Drakensberg Escarpment as the great supplier of water to South Africa*, Elsevier.
- Tennant W. and van Heerden J.: 1994, *The influence of orography and local sea-surface temperature anomalies on the development of the 1987 Natal floods: a general circulation model study*, *South African Journal of Science*, 90, 1:pages 45–49.
- Thoithi W., Blamey R.C., and Reason C.J.: 2021, *Dry spells, wet days, and their trends across Southern Africa during the summer rainy season*, *Geophysical Research Letters*, 48, 5:page e2020GL091041.
- Thrasher B., Maurer E.P., McKellar C., and Duffy P.B.: 2012, *Bias correcting climate model simulated daily temperature extremes with quantile mapping*, *Hydrology and Earth System Sciences*, 16, 9:pages 3309–3314.
- Thrasher B., Xiong J., Wang W., Melton F., Michaelis A., and Nemani R.: 2013, *Downscaled climate projections suitable for resource management*, *Eos, Transactions American Geophysical Union*, 94, 37:pages 321–323.
- Todd M. and Washington R.: 1999, *Circulation anomalies associated with tropical-temperate troughs in southern Africa and the south west Indian Ocean*, *Climate dynamics*, 15, 12:pages 937–951.
- Tozuka T., Abiodun B.J., and Engelbrecht F.A.: 2014, *Impacts of convection schemes on simulating tropical-temperate troughs over southern Africa*, *Climate dynamics*, 42, 1:pages 433–451.
- Tran Anh Q. and Taniguchi K.: 2018, *Coupling dynamical and statistical downscaling for high-resolution rainfall forecasting: Case study of the Red River Delta, Vietnam*, *Progress in Earth and Planetary Science*, 5, 1:pages 1–18.
- Trenberth K.E.: 2011, *Changes in precipitation with climate change*, *Climate Research*, 47, 1-2:pages 123–138.

- Trenberth K.E., Dai A., Rasmussen R.M., and Parsons D.B.: 2003, *The changing character of precipitation*, *Bulletin of the American Meteorological Society*, 84, 9:pages 1205–1217.
- Tshiala M.F., Olwoch J.M., and Engelbrecht F.A.: 2011, *Analysis of temperature trends over Limpopo province, South Africa*, *Journal of Geography and Geology*, 3, 1:page 13.
- Tyson P.D. and Preston-Whyte R.: 1972, *Observations of regional topographically-induced wind systems in Natal*, *Journal of Applied Meteorology*, 11, 4:pages 643–650.
- Tyson P.D., Preston-Whyte R., and Schulze R.: 1976, *The climate of the Drakensberg*, volume 31, Town and Regional Planning Commission.
- Tyson P.D. and Preston-Whyte R.A.: 2000, *Weather and climate of southern Africa*, Oxford University Press.
- Tyson P.D. et al.: 1990, *Modelling climatic change in southern Africa: a review of available methods*, *South African Journal of Science*, 86, 7-10:pages 318–329.
- UNESCO: 2000, *CONVENTION CONCERNING THE PROTECTION OF THE WORLD CULTURAL AND NATURAL HERITAGE*, Technical report, UNITED NATIONS EDUCATIONAL, SCIENTIFIC AND CULTURAL ORGANIZATION, wORLD HERITAGE COMMITTEE, Twenty-fourth session, Cairns, Australia 27 November – 2 December 2000.
- Unganai L.S.: 1996, *Historic and future climatic change in Zimbabwe*, *Climate research*, 6, 2:pages 137–145.
- Usoskin I.G.: 2017, *A history of solar activity over millennia*, *Living Reviews in Solar Physics*, 14, 1:pages 1–97.
- Vaittinada Ayar P., Vrac M., Bastin S., Carreau J., Déqué M., and Gallardo C.: 2016, *Intercomparison of statistical and dynamical downscaling models under the EURO-and MED-CORDEX initiative framework: present climate evaluations*, *Climate dynamics*, 46, 3:pages 1301–1329.
- van Heerden J. and Taljaard J.: 1998, *Africa and surrounding waters*, in *Meteorology of the southern hemisphere*, pages 141–174, Springer.
- Vautard R., Gobiet A., Sobolowski S., Kjellström E., Stegehuis A., Watkiss P., Mendlik T., Landgren O., Nikulin G., Teichmann C., et al.: 2014, *The European climate under a 2° C global warming*, *Environmental Research Letters*, 9, 3:page 034006.
- Vigaud N., Pohl B., and Créta J.: 2012, *Tropical-temperate interactions over southern Africa simulated by a regional climate model*, *Climate dynamics*, 39, 12:pages 2895–2916.
- Wallace J.M. and Hobbs P.V.: 2006, *Atmospheric science: an introductory survey*, volume 92, Elsevier.
- Warburton M., Schulze R., and Maharaj M.: 2005, *Is South Africa's temperature changing? An analysis of trends from daily records, 1950–2000*, *Climate change and water resources in southern Africa: studies on scenarios, impacts, vulnerabilities and adaptation*, pages 275–295.
- Weedon G.P., Balsamo G., Bellouin N., Gomes S., Best M.J., and Viterbo P.: 2014, *The WFDEI meteorological forcing data set: WATCH Forcing Data methodology applied to ERA-Interim reanalysis data*, *Water Resources Research*, 50, 9:pages 7505–7514.

- Wilby R.L. and Wigley T.M.: 1997, *Downscaling general circulation model output: a review of methods and limitations*, *Progress in physical geography*, 21, 4:pages 530–548.
- Williams C.J., Kniveton D.R., and Layberry R.: 2010, *Assessment of a climate model to reproduce rainfall variability and extremes over Southern Africa*, *Theoretical and applied climatology*, 99, 1:pages 9–27.
- Wood A.W., Leung L.R., Sridhar V., and Lettenmaier D.: 2004, *Hydrologic implications of dynamical and statistical approaches to downscaling climate model outputs*, *Climatic change*, 62, 1:pages 189–216.
- Wood A.W., Maurer E.P., Kumar A., and Lettenmaier D.P.: 2002, *Long-range experimental hydrologic forecasting for the eastern United States*, *Journal of Geophysical Research: Atmospheres*, 107, D20:pages ACL–6.
- Woodborne S., Hall G., Robertson I., Patrut A., Rouault M., Loader N.J., and Hofmeyr M.: 2015, *A 1000-year carbon isotope rainfall proxy record from South African baobab trees (*Adansonia digitata* L.)*, *PLoS One*, 10, 5:page e0124202.
- Yhang Y.B., Sohn S.J., and Jung I.W.: 2017, *Application of dynamical and statistical downscaling to East Asian summer precipitation for finely resolved datasets*, *Advances in Meteorology*, 2017.
- Yu R., Zhai P., and Lu Y.: 2018, *Implications of differential effects between 1.5 and 2° C global warming on temperature and precipitation extremes in China's urban agglomerations*, *International Journal of Climatology*, 38, 5:pages 2374–2385.